INCORPORATION OF TIME-DEPENDENT FRACTURE BEHAVIOUR IN THE STRUCTURAL DESIGN OF FIBRE REINFORCED CONCRETE ELEMENTS

A THESIS
submitted by
STEFIE J. STEPHEN
for the award of the degree
of
DOCTOR OF PHILOSOPHY

BUILDING TECHNOLOGY AND CONTRUCTION MANAGEMENT DIVISION
DEPARTMENT OF CIVIL ENGINEERING
INDIAN INSTITUTE OF TECHNOLOGY MADRAS
CHENNAI 600036

August 2019

DEDICATED TO THE LOVING MEMORY OF MY MOTHER

THESIS CERTIFICATE

This is to certify that the thesis entitled **INCORPORATION OF TIME-DEPENDENT FRACTURE BEHAVIOUR IN THE STRUCTURAL DESIGN OF FIBRE REINFORCED CONCRETE ELEMENTS**, submitted by **Stefie J. Stephen** to the Indian Institute of Technology Madras, for the award of the degree of **Doctor of Philosophy** is a bonafide record of research work carried out by her under my supervision. The contents of this thesis, in full or in parts, have not been submitted to any other Institute or University for the award of any degree or diploma.

Prof. Ravindra Gettu
Research Guide
Professor
Dept. of Civil Engineering
Indian Institute of Technology Madras

Chennai 600036
Date: 08.08.2019

ACKNOWLEDGEMENTS

I express my sincere gratitude to my guide Prof. Ravindra Gettu for making the journey of my doctoral thesis research a thoroughly enjoyable one in addition to being productive. I am indebted to him for the long hours of patient listening he gave me; however trivial my queries were. His persistence for perfection led me to understand that excellence is a habit and not a virtue. Integrating analytical skills with practical and experimental knowledge is one of his pre-eminent qualities that one can emulate. His profound ability to give easily adoptable solutions to problems, be it analytical or practical, reflecting his deep fundamental knowledge has inspired me immensely. In the various trying situations, I have faced, both in academic and personal fronts, during my tenure as a research scholar, he has been my pillar of strength. I thank him for having mentored me and let me learn from mistakes and for kindling my interest and curiosity in my field of study, as a young learner.

I am indebted to Prof. Benny Raphael for his valuable suggestions and for helping me with the optimisation algorithm. I am thankful to Prof. Manu Santhanam for his encouragement and the various valuable inputs given adding insight on many aspects of my research, in the capacity of my teacher as well as doctoral committee member. I am very grateful to Dr. Radhakrishna Pillai for his relentless support and suggestions that have helped me improve my technical writing skills and presentation skills in addition to the technical inputs given by him. I am very grateful to Dr. Sivakumar Palaniappan for having given me right directions for the progress of my work as a doctoral committee member. I take this opportunity to profoundly thank all the other faculty members of the Building Technology and Construction Management Division, Dr. Piyush Chaunsali, Prof. K Ananthanarayanan, Prof. K N Satyanarayana, Prof. Koshy Varghese and Dr. Ashwin Mahalingam for their continuous support and encouragement.

I am extremely grateful to Dr. T. Chellappa for his valuable inputs and words of wisdom given to me during my thesis preparation. I am thankful to Dr. Arul Jayachandran, Dr. Arun Menon, Dr. Dali Naidu Arnepalli and Prof. J Muralikrishnan for their constant support and encouragement.

With a deep sense of gratitude I profoundly thank Prof. Surendra P. Shah, Distinguished Professor, IIT Madras, and Prof. V. S. Gopalaratnam, Professor, University of Missouri, Columbia, for their timely suggestions, during their visits to IIT Madras, which resulted in throwing open many arenas in my research work. I owe a great deal of gratitude to Prof. José Luiz Antunes de Oliveira e Sousa, Professor, University of Campinas, for his valuable advice that helped me gain confidence in my area of research.

I record my gratitude to the Head of the Civil Engineering Department, Prof. K. Ramamurthy and former heads, Prof. Meher Prasad and Prof. S. R. Gandhi, for all the administrative support extended to me for carrying out this work. I am indebted to my doctoral committee member Dr. Srinivasa Chandrasekaran for his suggestions during different stages of my work.

I express my feelings of gratitude to Dr. Shyam Keralavarma, Assistant Professor, Department of Aerospace Engineering, Dr. Vidya Bhushan Maji and Dr. Atul Narayanan for their valuable suggestions, which helped me in the research progress.

The support extended to me by the staff of concrete lab has been a key point to the success of my thesis work. I profoundly thank Mrs. Malarrvizhi for her help and support. I thank Mr. Muthusamy, Mr. Soundarapandian, Mr. Subramaniam, Mr. Krishnan, Mr. Gasper, Mr. Siva and Mr. Arun for their immense help in carrying out the experimental work. I thank all the support staff of the lab. I wish to acknowledge the help rendered to me in carrying out the experiments by all the project associates and intern students who have worked with me. I express my thanks to Mr. Murali and all the staff of the Department Workshop for their help in all fabrication work. I am thankful to the staff of the Civil Engineering Department office, BTCM office and Department Computer facility for their cooperation.

I acknowledge the support of Messrs Bekaert Industries India, Nina and W.R. Grace for having provided the fibres used in this study. I am thankful to the Ministry of Human Resource Development (MHRD), Government of India, for providing scholarship during my research period at IIT Madras. I gratefully acknowledge the facilities established through the FIST Grant SR/FST/ETII-054/2012 in the Laboratory for Mechanical Performance of Civil Engineering Materials, IIT Madras, which were used in this research work.

All my fellow research scholars, Swathi, Dr. Srilatha, Ram, Shriram, Sujatha, Dr. Prabha, Santhosh, Marimuthu, Dr. Sripriya, Dr. Sunitha, Dr. Sakthivel, Dr. Komathi, Sachin, Sanoop, Sooraj, Aswathy, Reesha, Jayasree, Nithya, Dr. Pinky, Dr. Jayachandran, Dr. Bahrudeen, Dr. Murugan, Dr. Priyadharsini and many others, who have been a constant source of encouragement, have helped in making my tenure here a remarkable experience. I thank all of them for having taught me the importance of collaborative work.

I would not have been able to conduct this research work with such ardour if not for the whole-hearted support I have received from my family. I thank my deceased mother, Mrs. M. S. Komala and my father, Mr. K. S. James Stephenson for having been my constant support and for taking care of my son and home, which enabled me to work with free mind. Their unconditional love and enthusiastic encouragement have helped me reach my dreams. I immensely thank my sister, Dr. Jermie J. Stephen and her husband, Mr. Geo Lumin, for their every effort in taking care of my kid during my thesis preparation. I wish to specially thank my son, Allen Yeswin, for having put up with my busy schedule. I believe that it is the optimism of my husband, Mr. Anish Engles, that has made it possible for me to achieve this degree of success and I thank him immensely for it. I thank all the other members of my family who have made me what I am today.

Above all I would like to thank the Almighty and my mother, the guardian angel for showering blessings, which guided me throughout the course of this work.

Stefie J. Stephen

ABSTRACT

Use of fibre reinforced concrete (FRC) in applications such as tunnel lining segments, pavements, slabs-on-grade, bridge deck slabs and elevated slabs could help in lower thickness and maintenance cost. The design of these structures, which is based on the inelastic analysis techniques, utilises the residual strength of the material, since fibre bridging plays a major role after the formation of the cracks. However, the time-dependence of these parameters, which could govern the response under long-term and fatigue loading, is still unknown. The present study aims at providing a design methodology for FRC elements by incorporating appropriate time-dependent fracture models derived from extensive experimental data.

The fracture response of plain and fibre reinforced concrete can be characterized using modified linear elastic fracture mechanics models, such as the rising resistance curve (R-curve). The size-dependent geometric functions required for the nonlinear analysis have been calculated using linear elastic fracture mechanics (LEFM). The experimental response from the notched beam test is used to generate the R-curve, which can be used as a measure of the toughness of FRC. A comparison between the predicted flexural response of specimens of different geometry and the experimental data shows that the obtained R-curve can be used to understand the fracture response of FRC.

A cracked hinge model has been utilized to determine the bridging stresses developed along the cracked faces of FRC. An analytical formulation for the three-point bending specimen, considering a multilinear tensile constitutive model (σ-w curve), is used to develop closed-form solutions for the response. The parameters of σ-w curve that provide the best fit of the experimentally-obtained load versus crack mouth opening displacement (load-CMOD) curve are obtained using a global optimization algorithm. Tensile fracture properties of steel and polymer fibre reinforced concrete beams, with both softening and hardening-type behaviour, have been determined using the inverse analysis procedure. The applicability of method has been assessed by using the obtained σ-w curve to predict the response of specimens of different geometry, with varying fit parameters.

The effect of loading rate on the fracture response and on the tensile constitutive relation of FRC has been studied experimentally and trends are identified. The post-peak flexural response of FRC over loading rates covering 5 orders of magnitude, and the corresponding tetralinear stress-crack opening (σ-w) relations are obtained from inverse analyses. The results show that the tensile strength is lower and the initial drop in cohesive stresses is less steep at slower loading rates, more predominantly in concretes with lower toughness (i.e., concrete with polypropylene fibres and low dosages of steel fibres). Such behaviour is manifested by a longer fracture process zone during crack initiation. The variation in the σ-w relation with crack rate has been modelled empirically based on the rate-dependence of the concrete matrix and the tensile strength of the FRC. The general trend of decreasing flexural toughness with a decrease in loading rate has also been identified, with a moderating influence with higher dosages of steel fibres.

An experimental study of the post-peak fatigue behaviour of plain and fibre reinforced concrete (FRC) under bending has also been performed. Pre-cracked notched beams are tested for fatigue and the performance is evaluated. The S-N curves or Wöhler diagrams are plotted, using which fatigue models are proposed for different concretes. The level of fatigue damage is described in terms of the evolution of crack opening and stiffness degradation. The critical crack opening at which the fatigue crack growth becomes unstable has been identified and a S-N model for the critical crack opening is developed.

FRC structural elements that are most likely to be subjected to prolonged and fatigue loading during their design life have been considered to develop a comprehensive methodology for incorporating time-dependent models. Tunnel segments under service have to withstand slow soil settlement and groundwater movement and likewise, elevated slabs used for industrial purpose must bear heavy static loads for longer duration. Even though these structural elements are designed for high magnitude of loads, the duration of loading is not considered generally in conventional analysis and design. The developed rate effect models can be utilized to improve the reliability of the structure. Higher dosage of steel fibres in concrete has been found to be beneficial in restraining such rate effects.

In addition to prolonged loading, some FRC structures such as pavements, elevated slabs and tunnel segments, are subjected to fatigue loading, in the form of traffic movement, temperature variation and wind action. Even though these structures are designed based on toughness parameters, the fatigue design is often based on the pre-crack S-N model. The design procedure including reduction factors derived from both pre-peak and post-peak fatigue responses is appropriately illustrated for different structural elements and the implication of the dosage of fibres in concrete is discussed. It is found that higher dosages of steel fibres improve the moment carrying capacity of FRC structures especially at high fatigue loading.

Keywords: Fibre reinforced concrete, linear elastic fracture mechanics, R-curve, inverse analysis, tensile constitutive relation, stress versus crack width curve, load rate effects, post-peak fatigue, tunnel segments, elevated slabs, pavements.

TABLE OF CONTENTS

ACKNOWLEDGEMENTS....................i
ABSTRACT....................iv
LIST OF TABLES....................xi
LIST OF FIGURES....................xii
NOTATIONS....................xvi
ABBREVIATIONS....................xix
1 INTRODUCTION....................1
  1.1 Background....................1
  1.2 Objectives and Scope....................2
  1.3 Outline of the thesis....................2
2 R-CURVE ANALYSIS....................4
  2.1 Introduction....................4
  2.2 Use of R-curves in the analysis of FRC....................5
  2.3 Fracture analysis....................6
    2.3.1 Equations based on linear elastic fracture mechanics....................6
    2.3.2 The R-curve....................7
  2.4 Application of R-curve to FRC....................8
  2.5 Prediction of load-CMOD curves using the R-curve....................13
  2.6 Conclusions....................16
3 INVERSE ANALYSIS FOR THE σ-w CURVES....................17
  3.1 Introduction....................17
  3.2 Determination of the σ-w curve from test data....................17
  3.3 Inverse analysis using the three-point bending test....................19
    3.3.1 Background....................19
    3.3.2 Analytical formulation....................22
    3.3.3 Optimization algorithm....................29

3.3.4 Comparison of different models for the σ-w curve 30

3.3.5 Range of fitting variables..34

3.3.6 Parametric study..35

3.4 Application of inverse analysis procedure to FRC......................................40

3.5 Validation of analytical model 42

3.5.1 Unnotched beam 42

3.5.2 Notched beam with different geometry...43

3.6 Conclusions 45

4 RATE-DEPENDENCE OF THE FRACTURE PROPERTIES IN THE QUASI-STATIC REGIME 46

4.1 Introduction 46

4.2 Rate effects of plain and fibre reinforced concrete 46

4.3 Experimental program 48

4.3.1 Specimen preparation 48

4.3.2 Three-point bending test (3PBT)..49

4.4 Test results...49

4.4.1 Flexural tests...49

4.4.2 σ-w curves at different rates 52

4.5 Discussion of the trends..61

4.6 Effect of loading on the toughness parameters...64

4.7 Conclusions 68

5 POST-PEAK FATIGUE BEHAVIOUR OF CRACKED FRC IN FLEXURE 70

5.1 Introduction 70

5.2 Fatigue fracture of FRC in flexure...71

5.3 Experimental programme 77

5.3.1 Specimen details 77

5.3.2 Test procedure 78
5.4 Results and discussion 79
5.4.1 Flexural fatigue behaviour 79
5.4.2 *S-N* models for representing fatigue failure 90
5.4.3 *S-N* model based on critical CMOD 95
5.5 Conclusions 96
6 INCORPORATION OF TIME-DEPENDENT FRACTURE PROPERTIES IN STRUCTURAL DESIGN 98
6.1 General 98
6.2 Design modifications using time-dependent models 98
6.3 Design of tunnel lining segments 100
6.3.1 Load Case 1: Demoulding 101
6.3.2 Load Case 2: Stacking 102
6.3.3 Flexural load carrying capacity of the segment 103
6.3.4 Load Case 3: Construction stage 108
6.3.5 Load Case 4: Service stage 109
6.3.6 P-M interaction diagram for the segment 110
6.4 Design of pavements and slabs-on-grade 116
6.5 Design of elevated slabs 118
6.6 Conclusions 119
7 CONCLUSIONS 121
7.1 General conclusions 121
7.2 Specific conclusions 122
7.2.1 R-curve analysis 122
7.2.2 Inverse analysis for the σ-w curves 122
7.2.3 Rate-dependence of the fracture properties 123

7.2.4 Post-peak fatigue behaviour of cracked FRC 124
7.2.5 Incorporation of time-dependent fracture properties in the structural design 124
7.3 Recommendations for future work 125
REFERENCES 127
PUBLICATIONS BASED ON THE THESIS 138

LIST OF TABLES

Table 2.1. Characteristics of the fibres used (as given by the manufacturer) 9
Table 2.2. Fibre volume fraction and specimen notation 9
Table 3.1. Characteristics of constitutive model 21
Table 3.2. Fitting ranges and the optimization values obtained 34
Table 4.1. Details of the fibres 48
Table 4.2. Parameters of σ-w curves obtained from inverse analyses (mean ± standard deviation) 57
Table 4.3. Toughness parameters at different loading rates (mean ± standard deviation) 65
Table 5.1 Review of literature related to the flexural fatigue response of FRC 73
Table 5.2 Fatigue test parameters 79
Table 5.3 Critical CMOD at different fatigue loading levels 87
Table 6.1 The values of the fatigue reduction factors for desired fatigue life for FRC with different dosages of steel fibres 99
Table 6.2 Equations to compute member forces and moments under service load (ITA Report, 2016) 110
Table 6.3 Moment carrying capacity after incorporating the fatigue model 117
Table 6.4 Moment carrying capacity of slab subjected to different loading rates 119

LIST OF FIGURES

Figure 2.1. Fracture process zone in FRC......5
Figure 2.2. a) Test arrangement of three-point notched beam specimen b) finite element mesh used in the analysis 7
Figure 2.3. An illustration of evaluation of secant modulus (Xu and Reinhardt, 1998).....8
Figure 2.4. a) Effective crack growth obtained from the experimental load-CMOD data, and b) the R-curve for M40SF20......10
Figure 2.5. Comparison of crack resistance curves of concrete with different dosages of a) steel fibres, and b) polymer fibres (insets show the experimental load-CMOD curves) 12
Figure 2.6. Similar R-curves for two different concretes with similar flexural response .12
Figure 2.7. Variations in R-curves for concrete within the same set; a) M40SF30, and b) M40PF3.75 (the insets show the corresponding load-CMOD curves)......13
Figure 2.8. Flexural response of beam with notch length of 30 mm......14
Figure 2.9. Flexural response of beam with span length of 600 mm 15
Figure 3.1. Fracture response of fibre reinforced concrete loaded in uniaxial tension.....18
Figure 3.2. Two major approaches of inverse analysis: a) piece wise and b) holistic optimization 20
Figure 3.3. Model for a) precracked concrete, and b) cracked state with direct parameters, and c) with indirect or derived parameters 23
Figure 3.4. Test configuration 24
Figure 3.5. Deformation of the cracked hinge 24
Figure 3.6. Different phases of stress distribution in the ligament......26
Figure 3.7. Stress distribution for a multi-linear model......27
Figure 3.8. Flowchart describing the analytical process......28
Figure 3.9. Weighting considered in the robustness analysis: W1: uniform weight; W2: higher weight at the peak 31
Figure 3.10. Fitting of strain softening type response with a) bilinear, b) trilinear and c) tetralinear models, without (W1) and with (W2) weighting function 32
Figure 3.11. Fitting of strain hardening type response with a) bilinear, b) trilinear and c) tetralinear models, without (W1) and with (W2) weighting function 34

Figure 3.12. Optimization using different ranges of fitting variables 35
Figure 3.13. Diagrammatic illustration of different regions in the load-CMOD curve 36
Figure 3.14. Variation of the Load-CMOD curve with the Young's modulus 36
Figure 3.15. Variation of the Load-CMOD curve with the tensile strength 37
Figure 3.16. Variation of the Load-CMOD curve with σ_1 and w_1.................................38
Figure 3.17. Variation of the Load-CMOD curve with σ_2 and w_2.................................39
Figure 3.18. Variation of the Load-CMOD curve with σ_3 and w_3.................................39
Figure 3.19. Variation of the Load-CMOD curve with the critical crack length 40
Figure 3.20. Average load-CMOD curve for concrete reinforced with a) steel and b) polymer fibres 41
Figure 3.21. Tetralinear σ-w curves for concrete with a) steel and b) polymer fibres......42
Figure 3.22. Comparison of the predicted load-deflection curve for an unnotched beam with experimental data 43
Figure 3.23. Comparison of numerically obtained load-CMOD curve for beam with span=600 mm with experimental data...44
Figure 3.24. Comparison of numerically obtained load-CMOD curve for beam with notch length=30 mm with experimental data 44
Figure 4.1. Testing configuration...49
Figure 4.2. Typical flexural response of concrete with a) 3.75 kg/m^3 PF, b) 10 kg/m^3 SF, c) 30 kg/m^3 SF, and d) 45 kg/m^3 SF at different loading rates 52
Figure 4.3. a) Tetralinear tensile constitutive relation considered for FRC, and b) the corresponding stress distribution in the FPZ...53
Figure 4.4. Stress-crack opening curve concrete with a) 3.75 kg/m^3 PF, b) 10 kg/m^3 SF, c) 30 kg/m^3 SF, and d) 45 kg/m^3 SF at different loading rates..56
Figure 4.5. Finite element mesh used...58
Figure 4.6. Bridging stress variation in the FPZ of concrete with a) 3.75 kg/m^3 PF, b) 10 kg/m^3 SF, c) 30 kg/m^3 SF, and d) 45 kg/m^3 SF at different loading rates 60
Figure 4.7.Variation of fracture process zone length at a) peak load and b) CMOD = 0.5 mm, with respect to time...61
Figure 4.8. Variation of tensile strength with the loading rate 62
Figure 4.9. Variation of a) σ_1, b) σ_2 and c) σ_3 with CTOD rate for different concretes....63

Figure 4.10. Effect of loading rate on LOP for different types of concrete 66

Figure 4.11. Effect of loading rate on flexural toughness parameter for concrete with a) 3.75 kg/m^3 PF, b) 10 kg/m^3 SF, c) 30 kg/m^3 SF, and d) 45 kg/m^3 SF............................68

Figure 5.1 Comparison of *S-N* models based on pre-peak fatigue performance for FRC under flexure (40 kg/m^3 of steel fibres) with the model for plain concrete suggested in IRC:58-2010..75

Figure 5.2 Comparison of *S-N* models available for cracked FRC in literature..............76

Figure 5.3 Illustration of fatigue test procedure 79

Figure 5.4 Typical load versus CMOD curves for M40SF45 concrete beams under different fatigue loading levels 81

Figure 5.5 Typical CMOD vs. N response of a) M40SF10 b) M40SF30 and c) M40SF45 concrete (inset CMOD vs. $\log_{10}$N)...84

Figure 5.6 Typical CMOD rate under fatigue loading for M40SF10.............................85

Figure 5.7 Typical CMOD rate under fatigue loading for M40SF30.............................86

Figure 5.8 Typical CMOD rate under fatigue loading for M40SF45.............................86

Figure 5.9 Typical degradation of stiffness with fatigue cycles for different concretes...89

Figure 5.10 Fatigue response: a) increase in CMOD during fatigue loading, b) rate of increase in CMOD during fatigue loading and c) decrease in stiffness with fatigue loading...90

Figure 5.11 *S-N* curves for FRC reinforced with a) 0 kg/m^3 b) 10 kg/m^3, c) 30 kg/m^3, and d) 45 kg/m^3 of steel fibres 93

Figure 5.12 Comparison of *S-N* model for concretes with different dosage of steel fibres. 94

Figure 5.13 *S-N* model based on critical CMOD for FRC reinforced with different dosages of steel fibres...96

Figure 6.1 Fatigue reduction factors derived from S-N curves 99

Figure 6.2 Evolution of FRC in the tunnel segment industry (ITA Report, 2016).........100

Figure 6.3 Loading condition during demoulding phase 101

Figure 6.4 Loading condition during the stacking phase (ACI 544.7R, 2016).............102

Figure 6.5 Finite element model of tunnel lining segment used for numerical analysis.104

Figure 6.6 a) FRC tensile model obtained from inverse analysis and b) flexural load carrying capacity of Barcelona tunnel segment..105
Figure 6.7 Effect of loading rate on the load-carrying capacity of the tunnel segment with different dosages of steel fibre..107
Figure 6.8 Loading conditions during construction stage (ACI 544.7R, 2016).............108
Figure 6.9 Loading conditions for tunnel segment under service (ITA, 2000).............109
Figure 6.10 Material models for a) SFRC in tension, b) SFRC in compression and c) steel bars in tension (Yao et al., 2018)..111
Figure 6.11 Moment interaction diagram for the reinforced concrete tunnel segment...112
Figure 6.12 Load rate effects on moment-force interaction diagram for tunnel segment under service load condition..114
Figure 6.13 Variation of moment-force interaction diagram of tunnel segment with fatigue cycles..116

NOTATIONS

a	total crack length
a_0	initial notch depth
a_i	slope of each linear segment of σ-w curve
b	breadth of the beam
b_i	y-intercept of the linear segments of σ-w curve
C	compressive force
d_{clip}	thickness of the knife-edge
E	Young's modulus of concrete
$f_I(x)$ & $V_I(x)$	dimensionless geometry dependent LEFM functions
f_L	Peak flexural strength
$f_{R,1}$	Residual flexural strength at a CMOD of 0.5 mm
$f_{R,2}$	Residual flexural strength at a CMOD of 1.5 mm
$f_{R,3}$	Residual flexural strength at a CMOD of 2.5 mm
$f_{R,4}$	Residual flexural strength at a CMOD of 3.5 mm
f_t	tensile strength
H	depth of the beam
K_{IR}	critical stress intensity factor
L	length of the beam

l	span of the beam
l_c	chain length
M	Moment
n	number of linear segments of σ-w curve
P	applied load
P_i^{exp}	experimentally-obtained loads at the i^{th} point of the load-CMOD curve
P_i^{th}	analytically-predicted loads at the i^{th} point of the load-CMOD curve
R_i	initial radius of specimen
s	length of nonlinear hinge
T_i	tensile forces
$u(y)$	deformation of a strip
w	crack opening
w_c	critical crack opening
w_i	crack opening at i^{th} kink
x	relative crack length
y^*	the length of the linear tension region in uncracked zone
y_0	neutral axis depth
y_i	depth of different nonlinear stress kink locations
$\Delta \mathrm{a}$	crack extension
ΔC	change in circumference of specimen
Δl	output recorded from circumference extensometer

ε	Strain
θ_i	angle, in radians, subtended by initial chord length
σ	tensile stress
σ_i	tensile stress at i^{th} kink
ϕ	angular deformation
ψ_i	weighting function at the i^{th} point of the load-CMOD curve

ABBREVIATIONS

3PB	Three-Point Bending
CMOD	Crack Mouth Opening Displacement
COD	Crack Opening Displacement
FPZ	Fracture Process Zone
FRC	Fibre Reinforced Concrete
LEFM	Linear Elastic Fracture Mechanics
LOP	Limit of Proportionality
LVDT	Linear Variable Differential Transformers
MC 2010	CEB-FIB Model Code 2010
PDF	Probability Density Function
PF	Polymer Fibre
PGSL	Probabilistic Global Search Laussane
R-curve	Rising Resistance Curve
RILEM	The International Union of Testing and Research Laboratories for Materials and Structures
SF	Steel Fibre
SLS	Serviceability Limit State
ULS	Ultimate Limit State

1 INTRODUCTION

1.1 BACKGROUND

Fibres are added to improve the toughness and energy absorption capacity of concrete resulting from their crack bridging ability, which facilitates the applications of fibre reinforced concrete (FRC) in pavements, elevated slabs, tunnel lining segments, bridge decks, etc. With more extensive usage of FRC in structural applications and the potential for it to be employed in a wider range of structures, more sophisticated concepts are required for the design to exploit the higher load-carrying capacity under tension. Hence, fracture mechanics models, extending beyond Linear Elastic Fracture Mechanics (LEFM), need to be incorporated in the analysis and design for a rational approach toward the use of FRC in structures. Further, there is a necessity to obtain the parameters for the models from simple tests and robust analytical methods, such as inverse analysis.

The design of most FRC structures is based on inelastic analysis techniques that utilize residual strength or similar as the design parameter. The influence of low loading rates or long-term loads on the toughness parameters is significant in structures that could experience crack growth. For instance, in tunnel segments under service, the settlement of soil and groundwater influx can apply load gradually at a very slow rate. In industrial slabs accommodating rack storage, during the stacking of products, the slabs are subjected to sudden to gradual application of load and loading cycles. Hence, the design of such structural elements should include the effect of loading rate on the design parameters. However, the influence of long-term loading on post-peak strength is not well established, and hence, research is warranted for a better understanding of the rate-dependence so that its implications for FRC in such applications can be assessed.

In addition to prolonged static loading, some FRC structures, such as pavements, industrial slabs, bridge deck slabs and tunnel lining segments, are subjected to cyclic loads, in the form of traffic movement, thermal variation and machine vibration. These structures typically experience millions of stress cycles during the service life, which could have detrimental effects on material properties such as strength, stiffness, toughness and durability. Though there have been many studies on the fatigue of plain and fibre reinforced concrete in the uncracked (pre-peak) state, the post-peak fatigue response of cracked concrete has not been extensively explored. The use of appropriate design tools to account for the influence of toughness parameters under long-term and fatigue loading is expected to aid in improving the safety of the structure.

1.2 OBJECTIVES AND SCOPE

With the goal to develop guidelines to incorporate the time-dependent fracture properties in the design of FRC elements, the following objectives are formulated.

i. To determine a material tensile constitutive model through a robust inverse analysis method for use in the nonlinear finite element modelling of FRC structures.
ii. To characterize the rate-dependent fracture response of cracked FRC and obtain the relevant rate-dependence on the material parameters obtained through inverse analysis.
iii. To determine the post-peak fatigue characteristics of cracked FRC and model them appropriately.
iv. To provide guidelines for the incorporation of fatigue and load rate effects in the design of FRC structural elements.

The scope is limited to the following:

i. Tests are conducted on a M40 grade concrete with hooked-ended steel and polypropylene fibres. The volume fraction of fibres varies from 0.1% to 0.6%.
ii. Rates of loading considered vary such that the standard notched beam lasts for FRC toughness characterization between 30 seconds and 5 days.
iii. Tunnel lining segments, pavements and elevated slabs are the elements considered for illustrating the design guideline.

1.3 OUTLINE OF THE THESIS

The research strategy that was followed in order to achieve the objectives specified and the results obtained are described in the following chapters of the thesis. Since the scope is broad, corresponding literature can be found in individual chapters.

Chapter 2 has a review of nonlinear models available in literature and a simple R-curve model is used to describe the toughening mechanism of fibres in concrete. In this process, the procedure to derive size-dependent functions, which is used in R-curve analysis and cracked hinge model, based on linear fracture mechanics is explained. The linear elastic fracture mechanics equations that account for the specimen geometry have been derived and presented here.

Chapter 3 describes the nonlinear model used for analytical formulation and the detailed methodology to obtain tensile constitutive relations from the three-point bending test using inverse analysis. Also, this chapter details the application of fracture properties obtained using inverse analysis to predict the response of beam of other geometries to check their applicability.

In Chapter 4, the effects of loading rate on the flexural response of the FRC is presented along with the results of an extensive study of FRCs subjected to 5 different loading rates. A rate-dependent fracture model is developed based on the inverse analysis result obtained for FRCs subjected to different loading rates. The role of fibres in mitigating the rate-dependence is also discussed.

The experimental programme to characterise the post-peak fatigue response is presented in Chapter 5. The results for concrete with different dosage of steel fibres are discussed. The level of damage with an increase in fatigue cycles is discussed in terms of the increase in crack opening and reduction in stiffness. The discussion brings out the advantage of using higher dosages of steel fibres in FRC for the fatigue performance enhancement.

In Chapter 6, the design methodology to incorporate the rate-dependence and post-peak fatigue models is presented. The design philosophy is described for different structural elements subjected to different forms of long-term and fatigue loading, along with illustrative examples.

The conclusions drawn from the research work are summarized and presented in Chapter 7, including the scope for future research.

In the final section of the thesis, three appendices are given. Appendix A has the finite element mesh sensitivity analysis of the notched beam. Appendix B has the description and results of tests conducted to determine the uniaxial compressive stress-strain curve of FRC. The experimental results of flexural tests performed at different loading rate for different types of concrete have been summarised in Appendix C. Appendix D consists of the experimental data for all types of concrete for which the post-peak fatigue performance has been studied.

2 R-CURVE ANALYSIS

2.1 INTRODUCTION

Fracture analysis is essential for the accurate prediction of failure and crack initiation, which is critical in most structures. Linear elastic fracture mechanics (LEFM) is the basic theory available for the analysis of any structural problems dealing with fracture process. For concrete and other quasi-brittle materials, however the nonlinear zone ahead of the crack tip is relatively large compared to the element dimension and hence, its effect cannot be neglected as in LEFM. For such materials, the LEFM is modified to accommodate the nonlinear effect. The R-curve model utilizes the concept of the equivalent elastic crack and nonlinearity, and it helps in analysing the complete crack growth process. For the R-curve method, LEFM is modified by introducing a varying fracture toughness or energy that accounts for the nonlinearity of the fracture process, essentially by considering a stress-free crack along with a varying critical stress intensity factor.

In this chapter, the crack-extension resistance curve or R-curve derived from the response of notched beam specimen is expounded. This type of analysis provides additional information from simple test results, which can be used to estimate the failure pattern of any specimen or structural element. Further, this chapter examines the extent to which the R-curve can represent fracture in fibre reinforced concrete (FRC), which is more nonlinear than plain concrete. R-curves for concrete reinforced with the most commonly used fibres in construction industry, namely steel and polymer fibres are obtained using the experimental data obtained from three-point bending tests on notched FRC beams, following EN 14651 (EN 14651, 2005). The size dependent geometric functions calculated using LEFM are used in the R-curve approach to model the fracture in concrete (Gettu et al., 1990; Bažant et al., 1991; Karihaloo, 1995) and for determining the modulus of elasticity in the initial stage. The R-curve is used to explain the variation of toughness of concrete at different stages of crack propagation. The obtained R-curve is used to predict the flexural response of specimens of different geometry and the unambiguity of the R-curve is assessed by comparing the predicted response with experimental data. The variation in the R-curves with increase in dosage of steel and polymer fibres in concrete is also presented.

2.2 USE OF R-CURVES IN THE ANALYSIS OF FRC

Toughness parameters, such as equivalent and residual strength, are obtained based on simple elastic bending theory at the crack plane from commonly used four- and three-point bending testing configurations (JSCE Part III-2 (SF1–SF4), 1984; RILEM TC 162-TDF, 2002; EN 14651, 2005; ASTM C1609/C1609M, 2010; ICI-TC/01.1, 2014). For instance, the residual strength of FRC at a specific deflection, say serviceability limit (0.5 mm), is calculated considering the entire depth of the beam, ignoring any crack growth. However, in FRC, a nonlinear zone, termed fracture process zone (FPZ), is formed where fibre pull out, aggregate bridging and micro cracking occurs (See Figure 2.1). The size of this zone, large enough to be considered in calculations, is in contrast with the LEFM solutions. Hence, approaches based on nonlinear theories have been used to represent the evolution of the FPZ and the improved toughness due to the incorporation of fibres in concrete (Ouyang et al., 1990; Eissa and Batson, 1996; Mobasher and Li, 1996; Dey et al., 2015). Basic approximate nonlinear models such as the two-parameter model (Jenq and Shah, 1986), the effective crack model (Karihaloo and Nallathambi, 1989) and the R-curve models do not need any sophisticated finite element code for the analysis.

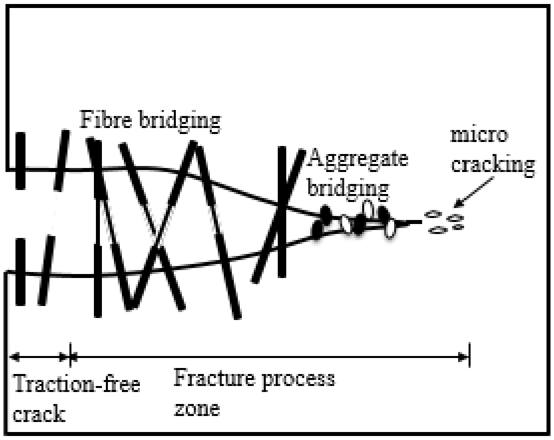

Figure 2.1. Fracture process zone in FRC

Among these nonlinear models, the R-curve is advantageous because it represents both pre- and post-peak response of the concrete reasonably well. For a given material under external load, there is a unique relationship between the crack extension (Δa) and the stress intensity factor (K_I), which is termed as the R-curve. In a body of infinite size, where the full FPZ can be developed in an unhindered manner (Gettu et al., 1990; Bažant et al., 1991; Karihaloo, 1995), the R-curve reaches a plateau. However, in a smaller specimen, the R-curve keeps rising, thus making it dependent on specimen size and geometry (Foote et al., 1986; Cotterell and Mai, 1987; Banthia and Sheng, 1996; Mai, 2001), especially during the unstable fracture (Wecharatana and Shah, 1983; Bažant et al., 1986; Kumar and Barai, 2010; Brake, 2012; Zhao et al., 2015). The significance of the R-curve is that, in spite of being geometry and material dependent, there are correlations with the constitutive relation of the material (Morel et al., 2010). For a given σ-w curve, the $K_I(\Delta a)$ can be found using an appropriate Green's function as proposed by Foote et al. (1986), and vice versa. Also, the R-curve has been used to determine the bridging stress behaviour of ceramic and concrete materials (Fett et al., 2000; Mobasher et al., 2015) for use in the analysis of structural behaviour.

2.3 FRACTURE ANALYSIS

2.3.1 Equations based on linear elastic fracture mechanics

The flexural toughness testing of a notched beam conforming the EN 14651 standard (EN 14651, 2005) uses a centre-point loaded (P) beam with length (L) = 700mm, width (b) = 150mm, depth (d) = 150mm, notch length (a_0)= 25 mm and span of the support (l) = 500mm (Figure 2.2). The stress intensity factor for mode I fracture (K_I) in such a specimen with a relative crack length of 'x' can be expressed as,

$$K_I = \frac{3Pl\sqrt{\pi a}}{2bd^2} f_I(x) \tag{2.1}$$

Similarly, the crack mouth opening displacement ($CMOD$) is given by,

$$CMOD = \frac{6Pla}{Ebd^2} V_1(x);\ x = \frac{a}{d} \tag{2.2}$$

where, $f_I(x)$ and $V_1(x)$ are dimensionless geometry dependent LEFM functions, which can be determined by linear elastic analysis.

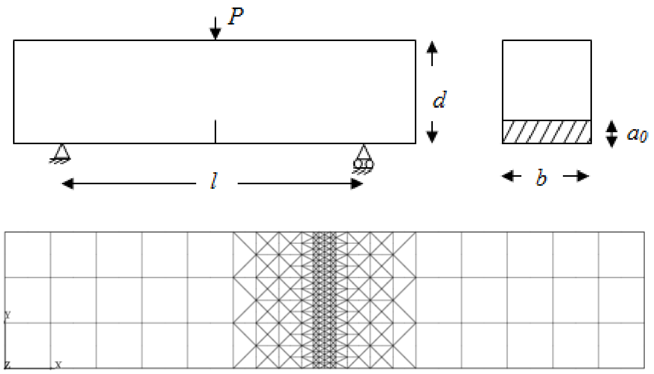

Figure 2.2. a) Test arrangement of three-point notched beam specimen b) finite element mesh used in the analysis

The Young's modulus, E = 1 GPa and the stiffness modulus = 10^8 N/mm^3 are assumed during the linear-static analysis performed using the finite element programme TNO DIANA v9. The numerical computation is performed for the relative crack length range of $0.02 \leq x \leq 0.85$ (corresponding total crack length $3.125\text{mm} \leq a \leq 128.125\text{mm}$). A unit load is applied at the mid-span of the beam, and the crack mouth opening displacement and load-point deflection, are obtained for different crack lengths. The geometry-dependent functions are derived following the procedures given by Ferreira et al. (2002) and García-Álvarez et al. (2017). The equations obtained are expressed as follows:

$$f_I(x) = 0.4 + 7.3x - 41.6x^2 + 118.5x^3 - 156.3x^4 + 85.2x^5 \text{ for } 0.17 \leq x \leq 0.65 \quad (2.3)$$

$$f_I(x) = \frac{0.604 - 0.547x}{1 - 2.026x + 1.027x^2} \quad \text{for } x > 0.65 \quad (2.4)$$

$$V_1(x) = 0.197 + 17.816x - 107.63x^2 + 338.21x^3 - 494.26x^4 + 298.86x^5 \quad \text{for } 0.175 \leq x \leq 0.65 \quad (2.5)$$

$$V_1(x) = \frac{0.817 - 0.218x}{1 - 2.011x + 1.012x^2} \quad \text{for } x > 0.65 \quad (2.6)$$

2.3.2 The R-curve

The R-curve is considered here as the relation between the critical stress intensity factor (K_{IR}) and the crack extension $\Delta a = a - a_0$, where a = total crack length and a_0 =

initial notch length, and denoted as $K_{IR}(\Delta a)$. The Young's modulus of concrete, E, can be obtained by using the initial linear part of experimentally obtained load-CMOD curve using the following equation derived from Eq. (2.2).

$$E = \frac{6Pla_0}{CMOD\, bd^2} V_1(x_0);\ x_0 = \frac{a_0}{d} \qquad (2.7)$$

The relative crack length is obtained by iterating for x in the following equation (Banthia and Sheng, 1996; Xu and Reinhardt, 1998; Wu et al., 2006; Wallin, 2013):

$$\beta(x) = \frac{CMOD\, bdE}{6Pl} = xV_1(x) \qquad (2.8)$$

Conceptually, the crack length x represents the traction free crack plus an equivalent fracture process zone length corresponding to the secant compliance (C_s), as shown in Figure 2.3 (Xu and Reinhardt, 1998). For different effective crack lengths, K_{IR} is calculated using Eq. (2.1) and Eq. (2.3) or (2.4), considering that the load-CMOD curve is governed by the propagating crack.

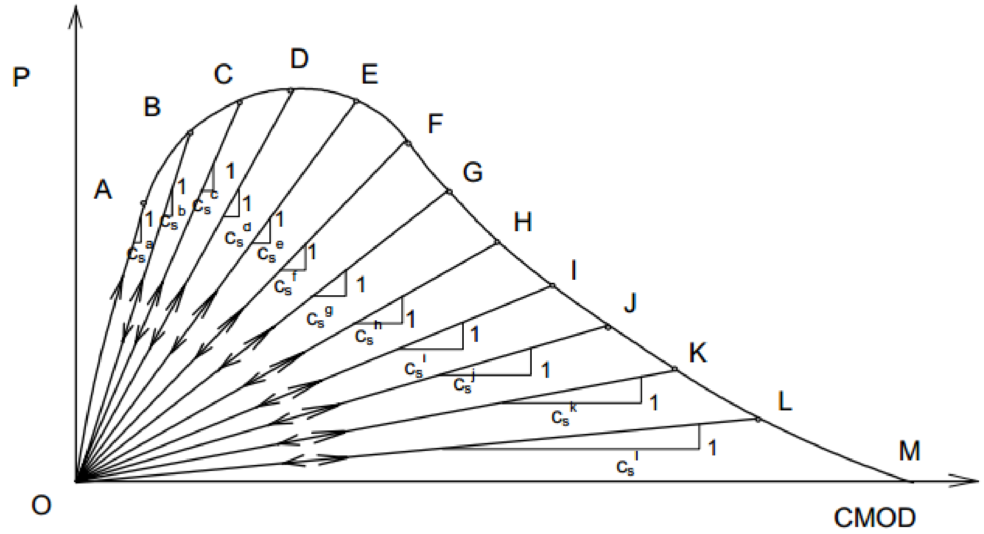

Figure 2.3. An illustration of evaluation of secant modulus (Xu and Reinhardt, 1998)

2.4 APPLICATION OF R-CURVE TO FRC

The toughness of steel (SFRC) and polymer fibre reinforced concrete (PFRC) made of M40 grade concrete (with a maximum aggregate size of 20 mm) is assessed for 6 specimens in each case. Table 2.1 presents the characteristics of fibres used in the FRC. Polypropylene (PF) and hooked-ended cold drawn steel fibres (SF) have been used at different dosages (Table 2.2). The details of specimen preparation, curing and testing can be found in Jose et al. (2018).

Table 2.1. Characteristics of the fibres used (as given by the manufacturer)

Properties	**Steel fibres**	**Polymer fibres**
Specific gravity	7.8	0.92
Length (mm)	60	40
Aspect ratio (length/diameter)	80	90
Characteristic tensile strength (MPa)	1225	620

Table 2.2. Fibre volume fraction and specimen notation

SF dosage (kg/m^3); Volume fraction	**Specimen notation**
0; 0%	M40SF0
10; 0.1%	M40SF10
15; 0.2%	M40SF15
20; 0.3%	M40SF20
30; 0.4%	M40SF30
45; 0.6%	M40SF45

PF dosage (kg/m^3); Volume fraction	**Specimen notation**
0; 0%	M40PF0
2.5; 0.3%	M40PF2.5
3.75; 0.4%	M40PF3.75
5; 0.54%	M40PF5

The methodology used for deriving the R-curve is illustrated using an FRC beam specimen reinforced with 20 kg/m^3 (M40SF20) and a notch length of 25 mm. The variation in the effective crack growth (Δa), obtained as a function of the CMOD, determined using the Eqn. (2.8), is shown in Figure 2.4a, along with the experimentally-obtained load-CMOD curve used in the derivation. The crack grows faster until a CMOD value of about 0.5 mm, and when the CMOD reaches 1.5 mm, the effective crack length is about 110 mm, beyond which there is no significant crack growth. The experimental load and the corresponding effective crack length are substituted in Eq. (2.1) to obtain the K_{IR}-value, the evolution of which is shown in Figure 2.4b, along with the parent P-Δa curve. It is evident that the stress intensity factor increases with an increase in crack length, as expected. When the crack reaches the boundary of the specimen, the increase in stress intensity factor becomes even more rapid.

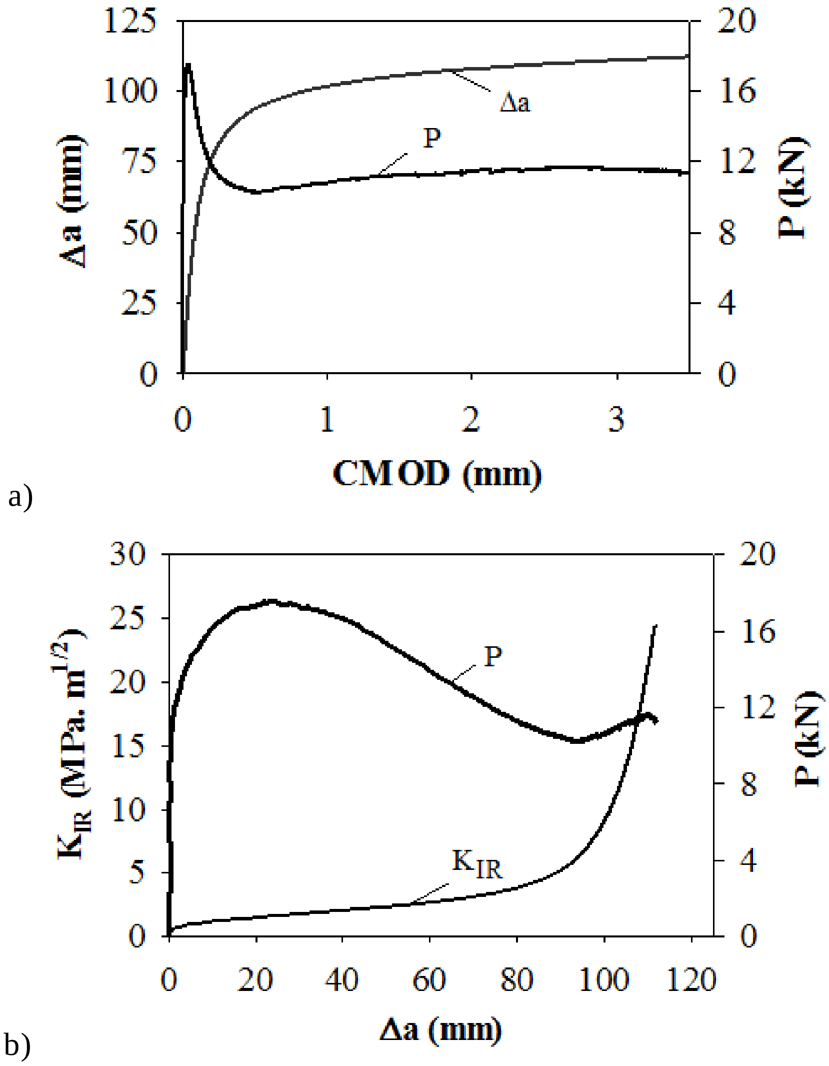

Figure 2.4. a) Effective crack growth obtained from the experimental load-CMOD data, and b) the R-curve for M40SF20

Typical R-curves for different dosages of steel fibres are shown in Figure 2.5a, corresponding to the experimental load-CMOD curves shown in the insets. With an increase in the fibre dosage, the toughness of the concrete increases, which is reflected by a gradual change from softening to plastic-type response. This leads to R-curves that are higher, especially beyond the peak load (× in each plot indicates the peak load, which does not change significantly with increase in fibre dosage) that occurs around the

CMOD of 0.5 mm. The effective crack lengths at different CMOD levels for concrete with different dosage of fibres are indicated by the dashed lines in the graphs. The mitigation of crack growth by fibres, in concrete with higher dosage of fibres, is reflected by the lower crack extension at a particular CMOD. Similar behaviour is observed in the PFRC (Figure 2.5b), except that for the same volume fraction, the stress intensity factor values are lower than those of SFRC. This describes the fact that even though the fibre volume fractions are the same, PFRC exhibits lower toughening than in SFRC. However, if the load-CMOD curves are similar, say in the case of M40SF10 and M40PF3.75, the R-curves obtained are comparable, as expected; see Figure 2.6.

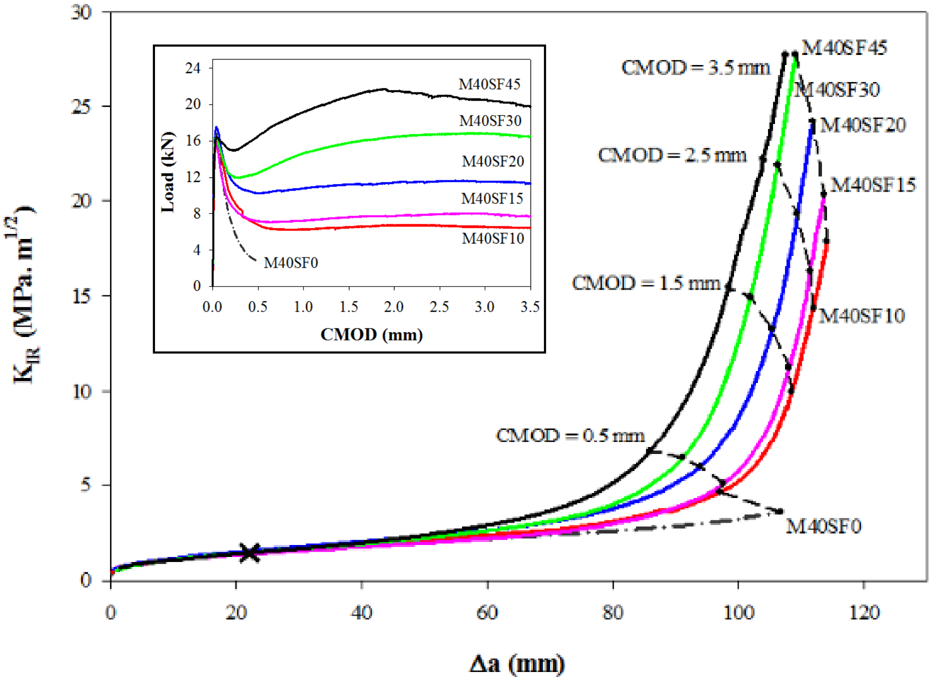

a)

The variation among R-curves is found to be low within a certain set of FRC specimens, with the same fibre type and volume fraction. However, the concrete reinforced with PF exhibits slightly lower scatter than SF (as can be seen in Figure 2.7). This is in accordance with previous studies that have attributed the lower scatter in polymer fibre reinforced concrete response to the larger number of fibres present in a unit volume of concrete or across a crack face than in steel fibre concrete, for the same volume fraction (Nayar et al., 2014)

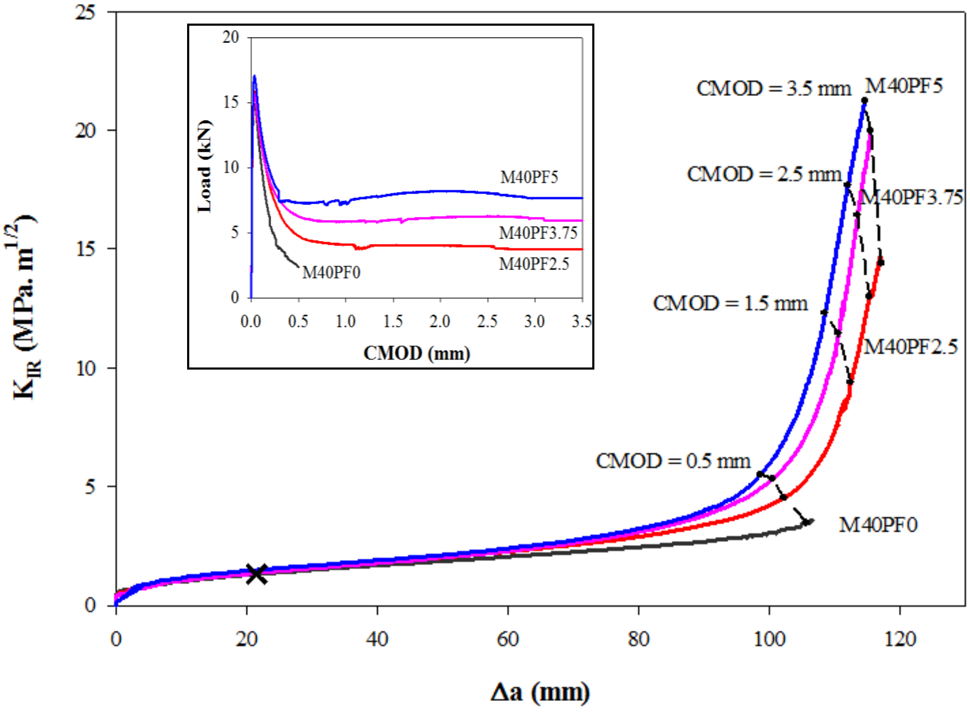

b)

Figure 2.5. Comparison of crack resistance curves of concrete with different dosages of a) steel fibres, and b) polymer fibres (insets show the experimental load-CMOD curves)

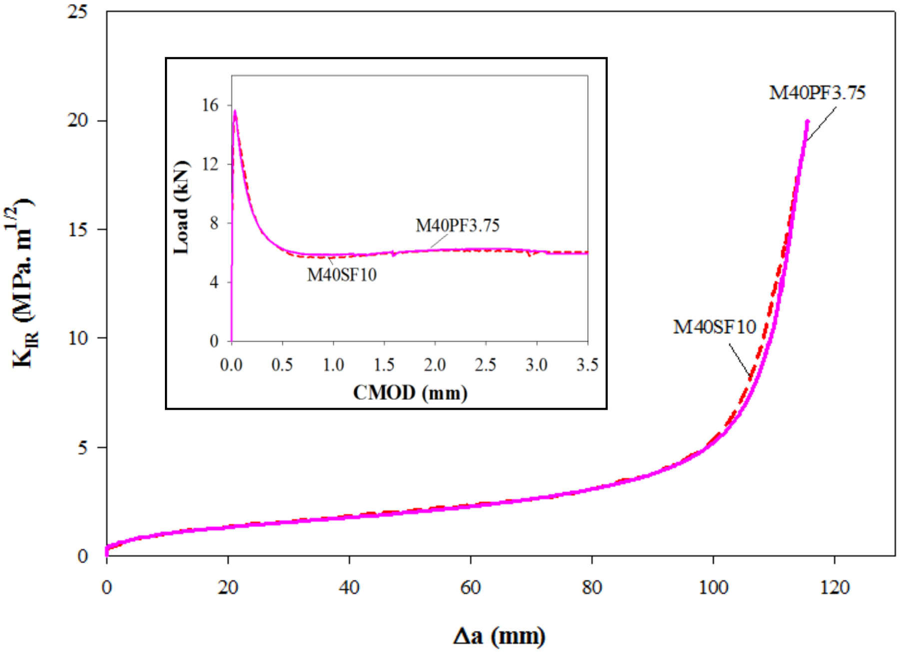

Figure 2.6. Similar R-curves for two different concretes with similar flexural response

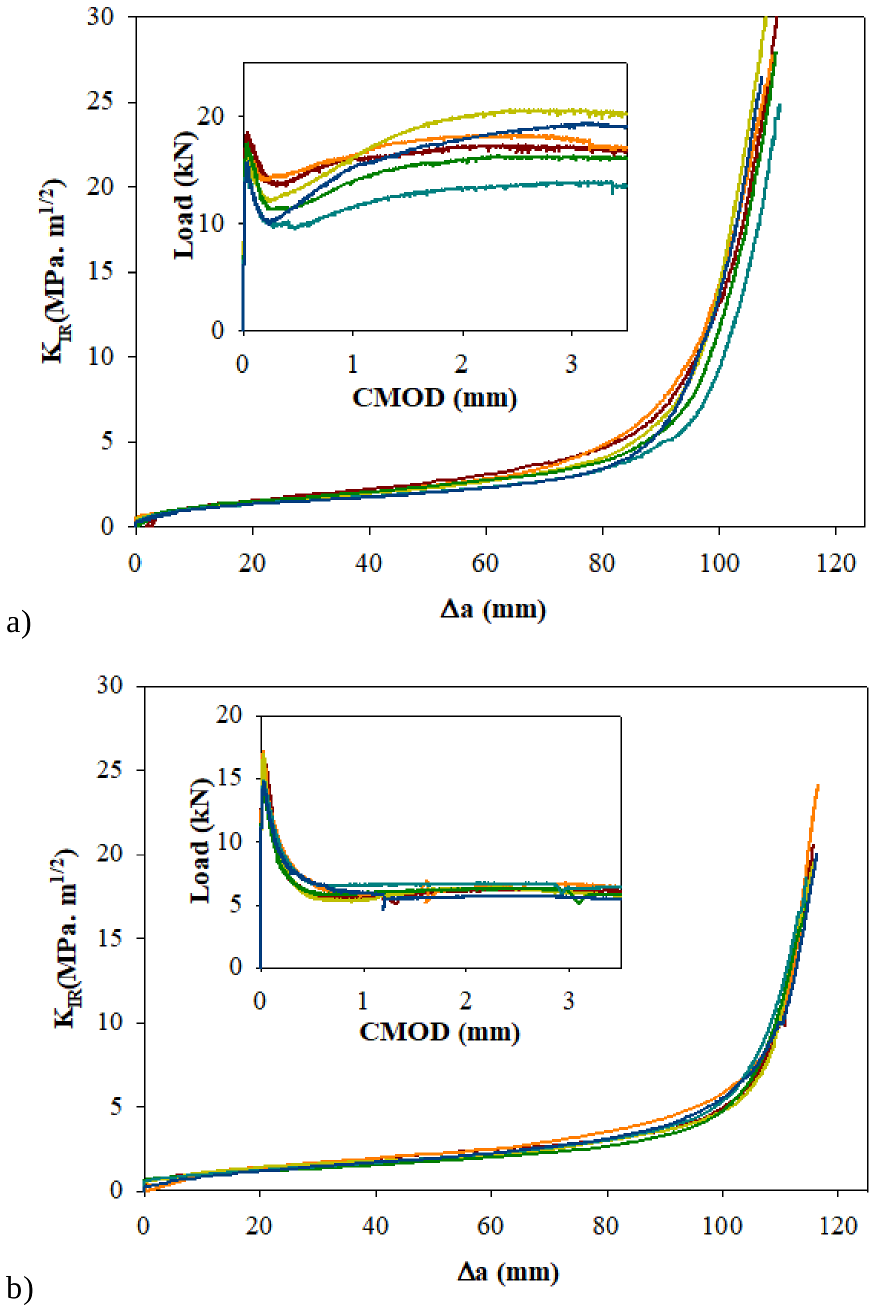

Figure 2.7. Variations in R-curves for concrete within the same set; a) M40SF30, and b) M40PF3.75 (the insets show the corresponding load-CMOD curves)

2.5 PREDICTION OF LOAD-CMOD CURVES USING THE R-CURVE

In order to assess whether the R-curve described earlier could be used to simulate the flexural response of specimens/elements of different geometry, tests were performed on M40SF30 concrete specimens that are similar to those referred to earlier but with a different notch length or span. The average R-curve obtained, from six M40SF30 beams with notch length of 25 mm, was used to predict the response of a beam with a notch length of 30 mm, using the LEFM functions already given in Eqns. (2.3) to (2.6). The predicted load-CMOD curve is compared with experimental data for this specimen geometry in Figure 2.8, and is found to fall within the band of results though closer to the lower bound. This may be because of the slightly shorter crack growth, in this case compared to the shorter notch length, due to the boundary effect. It can be inferred that due the longer notch length, the crack reaches the specimen boundary with a CMOD smaller than in the standard beam.

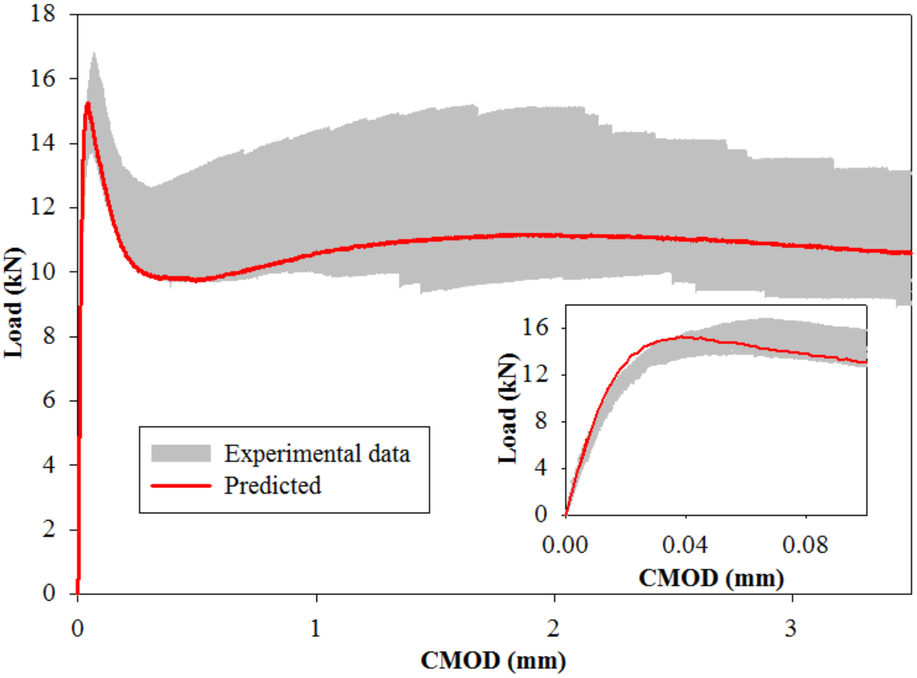

Figure 2.8. Flexural response of beam with notch length of 30 mm

Similarly, the prediction was made for beams with a span length of 600 mm and notch length of 25 mm, using the following LEFM equations derived for this purpose:

$$f_I(x) = 1.03 - 0.57x - 1.38x^2 + 20.87x^3 - 43.31x^4 + 34.96x^5 \quad \text{for } 0.17 \le x \le 0.65 \tag{2.9}$$

$$f_I(x) = \frac{0.59 - 0.50x}{1 - 1.98x + 0.98x^2} \quad \text{for } x > 0.65 \tag{2.10}$$

$$V_1(x) = 1.28 + 2.14x - 21.07x^2 + 113.32x^3 - 216.76x^4 + 168.06x^5 \quad \text{for } 0.17 \le x \le 0.65 \tag{2.11}$$

$$V_1(x) = \frac{0.84 - 0.25x}{1 - 2.013x + 1.014x^2} \quad \text{for } x > 0.65 \tag{2.12}$$

$$V_1(x) = \frac{0.84 - 0.25x}{1 - 2.013x + 1.014x^2} \quad \text{for } x > 0.65 \tag{2.13}$$

It can be seen in Figure 2.9 that the prediction is within the experimental band of results, though the tail of the post-peak region approaches the upper bound. Beyond a crack opening of about 1.5 mm, crack progression is limited due to the effect of the boundary. Since the fracture does not propagate significantly beyond 1.5 mm, the flexural response until this crack opening could give a more representative flexural characterization of a material, instead of using the response until the CMOD of 3 or 4 mm.

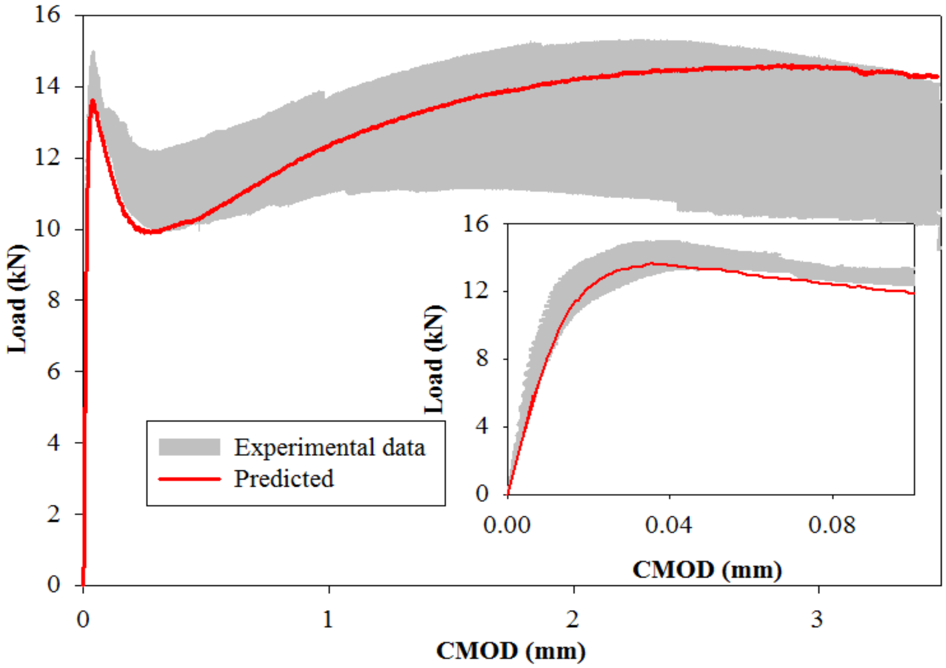

Figure 2.9. Flexural response of beam with span length of 600 mm

2.6 CONCLUSIONS

The rising resistance curve (R-curve) obtained using the response of the FRC beam specimen tested in accordance with RILEM 162 TDF and EN14651 recommendations has been presented in this chapter. The size-dependent geometric functions required for the nonlinear R-curve analysis have been derived using linear elastic fracture mechanics (LEFM). The effect of fibres in improving the toughness is well reflected by the R-curves obtained for concrete with different dosages of steel and polymer fibres. It has been found that the fracture resistance values are consistently higher for concrete reinforced with steel fibres than with polymer fibres, for the same volume fractions. The R-curves obtained using the EN 14651 specimen have been used satisfactorily to predict the flexural response for other geometries as well. Since the crack progression beyond a crack opening of about 1.5 mm in the EN 14651 specimen is limited by the specimen boundary, it is proposed that toughness characterization be limited to the crack opening of 1.5 mm, instead of 3.5 mm. This is more likely to provide a more representative material characterization without much effect of the specimen dimensions.

3 INVERSE ANALYSIS FOR THE *σ-w* CURVES

3.1 INTRODUCTION

A majority of cracks formed in concrete structures can be ascribed to some form of tensile stresses, thus necessitating the determination of tensile characteristics. The fracture characteristics of FRC can be found by the direct uniaxial tensile test (RILEM TC 162-TDF, 2002; Barragán et al., 2003) or indirectly from flexural, wedge splitting or round panel tests, or finite element analysis by using analytical models (Hillerborg et al., 1976; Olesen, 2001) combined with inverse analysis. Even though the use of the tensile characteristics of concrete is not common in design calculations, finite element predictions of different structural elements require the tensile constitutive relation as the input parameter.

This chapter deals with the development of the inverse analysis procedure for the determination of tensile stress-crack opening (*σ*-*w*) curve from the flexural response of fibre reinforced concrete, considering nonlinearity and inelasticity after cracking. A closed-formed solution is developed using an analytical formulation for the three-point bending test considering a multilinear stress-crack opening (*σ*-*w*) curve. A global optimization algorithm has been used to determine the tensile constitutive relation represented by the *σ*-*w* curve by identifying the parameters that provide the best fit with the load versus crack mouth opening displacement (load-CMOD) curve obtained. The multilinear model derivation is based on the cracked hinge model developed by Olesen (Olesen, 2001), and the optimization of the parameters has been done using the Probabilistic Global Search Lausanne (PGSL) algorithm (Raphael and Smith, 2003). The procedure has been applied for determining the tensile constitutive parameters of steel and polymer fibre reinforced concrete, with both softening and hardening-type behaviour. The parameters thus obtained have been used to predict the response of different geometries of beams to assess the applicability of the methodology.

3.2 DETERMINATION OF THE *σ-w* CURVE FROM TEST DATA

The toughness of fibre reinforced concrete (FRC) is usually characterized using a three-point bending test (JSCE Part III-2 (SF1–SF4), 1984; RILEM TC 162-TDF, 2002;

EN 14651, 2005; ASTM C1609/C1609M, 2010; ICI-TC/01.1, 2014), and the parameters obtained have been used in the design of structural components, such as slabs-on-grade and industrial flooring (CNR DT 204, 2006; fib Model, 2010; TR34, 2013). However, such parameters are not direct representation of the material tensile response and, therefore, more appropriate fracture properties of the material need to be deduced for generic structural analysis. In this context, the stress-crack opening relation (σ-w) can be a useful constitutive model for characterizing the nonlinear fracture of concrete. The tensile curve of FRC has an initial linear elastic region until the crack is formed. As the stress rises the tensile strength of the concrete is reached. Then, there is a gradual drop in stress until failure, in the case of plain concrete. In the case of FRC, the fibre bridges the crack and the tensile curve flattens or rises depending upon the dosage and type of fibre. (Figure 3.1).

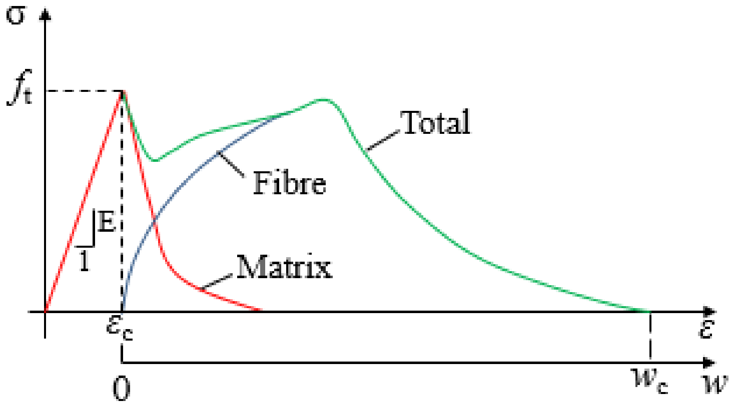

Figure 3.1. Fracture response of fibre reinforced concrete loaded in uniaxial tension

The standard methods generally used for fracture characterization are three-point bending tests (JSCE Part III-2 (SF1–SF4), 1984; RILEM TC 162-TDF, 2002; EN 14651, 2005; ASTM C1609/C1609M, 2010; ICI-TC/01.1, 2014), round determinate panel tests (Bernard,2000; ASTM C-1550, 2003), splitting tensile tests and uniaxial tensile tests (RILEM TC 162-TDF, 2001). The most direct test method to determine the fracture response of concrete is the uniaxial tensile test (Barragán et al., 2003). A number of technical problems must be solved before a reliable and reproducible uniaxial tensile test is obtained. The indirect methods could either be based on empirical equations (di Prisco, 2004) or closed-formed solutions obtained for bending (Jepsen et al., 2016), wedge splitting (Østergaard, 2003; Østergaard and Olesen, 2003; Löfgren, 2005; Skoček and

Stang, 2008) or round panel test configurations for the inverse analysis (Ciancio et al., 2014; Nour et al., 2015). The Round Determinate Panel (RDP) test has proven to be a reliable method for designing the fibre dosage of shotcrete used in tunnelling application; the round panels have been notched to obtain the load-CMOD curve and with the use of analytical formulation, the moment-curvature diagram is derived, which could later be used for the determination of fracture response (Ciancio et al., 2014). However, the test results of the panels show large scatter, which might lead to erroneous characterisation of fracture response.

3.3 INVERSE ANALYSIS USING THE THREE-POINT BENDING TEST

3.3.1 Background

The inverse analysis procedure generally consists of iterative modus operandi, which fit experimental data to obtain the parameters that define the σ-w curves. Roelfstra and Wittmann (1986) were the pioneers to propose inverse analysis for the determination of σ-w curve for concrete. However, the limitation of their type of analysis is that the algorithm can only find local minima rather than global minima. Later, Stang and Olesen (1998) developed the cracked hinge model, based on the work done by Ulfkjær et al. (1995) and this model was extended by Østergaard (2003) by incorporating in a Matlab program.

One of the common approaches for inverse analysis involves a step-by-step extension of softening curve otherwise called piecewise analysis (Nanakorn and Horii, 1996a; Kitsutaka, 1997). This analysis is performed at each experimental data point, thereby yielding a polylinear curve, and each new trial depends on the value obtained on the previous step making it more sensitive to experimental errors (Slowik et al., 2006; Skoček and Stang, 2010). In this holistic approach (illustrated in Figure 3.2b) the shape of the σ-w curve is predefined and it is almost the same as the polylinear curve obtained by piecewise analysis (Sousa et al., 2007) and also the computational procedure is easy.

For plain concrete, the shape of the σ-w curve is taken as bilinear (Roelfstra and Wittmann, 1986; Østergaard, 2003) or exponential (Planas et al., 1999; Slowik et al., 2006), and for fibre reinforced concrete (FRC), a bilinear (Kooiman, 2000; Olesen, 2001; Østergaard, 2003; Buratti et al., 2011) or trilinear model (Barros et al., 2005; Löfgren, 2005; Sousa and Gettu, 2006) is required for representing the fracture properties. Recent studies of FRC have shown that the bilinear model is not adequate for a material exhibiting pseudo-hardening behaviour, necessitating multilinear models (Kang et al., 2010; Jepsen et al., 2016; Reddy and Subramaniam, 2017), which could, however, increase the complexity of the inverse analysis and the ambiguity of the results obtained.

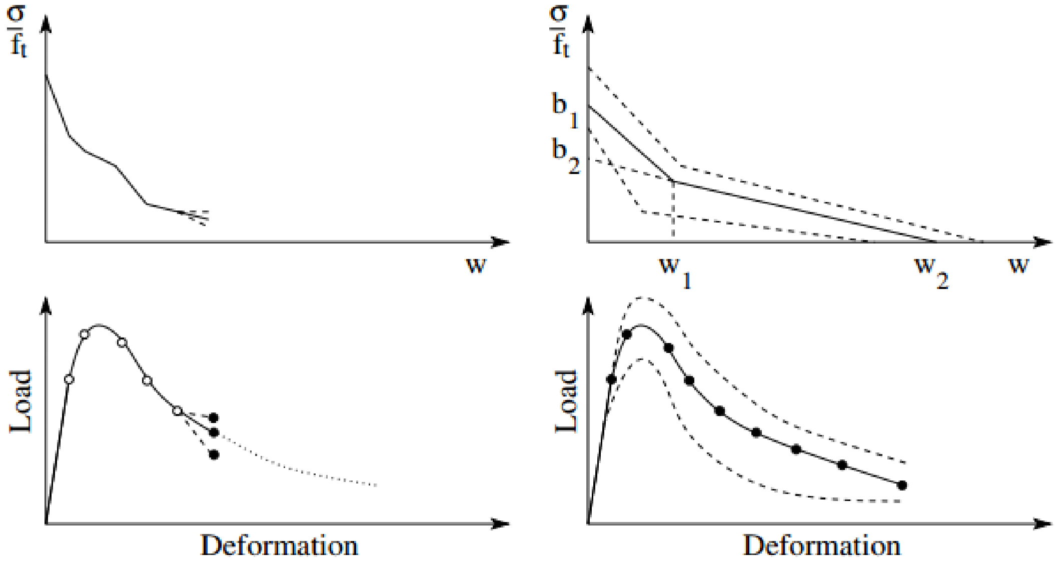

a) b)

Figure 3.2. Two major approaches of inverse analysis: a) piece wise and b) holistic optimization

In Table 3.1, the criteria considered in each of the constitutive models are presented. Based on the literature review of recent studies, a multilinear model with holistic approach is used for the determination of *σ*-*w* curve.

Table 3.1. Characteristics of constitutive model

Reference	**Material**		**Type of test**			**Analysis**		**Type of model for σ-w curve**		
	Plain Concrete	**FRC**	**3PB**	**WST**	**RDP**	**Piecewise**	**Holistic**	**Bilinear**	**Trilinear**	**Multi-linear**
Kitsutaka, 1997	●		●			●				●
Kooiman, 2000		●	●					●		
Meda et al., 2001	●	●		●				●		
Olesen, 2001		●	●					●		
Østergaard, 2003	●		●	●				●		
Barros et al., 2005		●	●				●		●	
Löfgren, 2005		●	●	●			●	●		●
Sousa and Gettu, 2006	●	●	●				●	●	●	
Sousa et al., 2007	●	●	●				●	●	●	
Skoček and Stang, 2008	●			●			●	●	●	●
Kang et al., 2010		●	●				●			●
Buratti et al., 2011		●	●				●	●		
Yoo et al., 2014		●	●				●	●	●	
Ciancio et al., 2014		●			●	●		●		
Nour et al., 2015		●	●		●	●				●
Jepsen et al., 2016			●				●			●
Reddy and Subramaniam, 2017			●				●			●

3.3.2 Analytical formulation

An analytical model based on the concept of a non-linear hinge is used here for simulating the three-point bending test of FRC (Olesen, 2001). This approach has previously been employed by various researchers (Löfgren et al., 2005; Sousa and Gettu, 2006; Buratti et al., 2011; Jepsen et al., 2016; Reddy and Subramaniam, 2017) as it yields closed-form analytical solutions for the entire load-crack mouth opening displacement (load-CMOD) curve. The maximum bending moment in the centrally-loaded notched beam occurs at mid-span and the fracture occurs along the notch plane. Consequently, the nonlinear hinge of length ‘s’ is placed at mid-span and is taken as half the beam depth, as recommended on the basis of extensive numerical simulations by Ulfkjær et al. (1995). The remaining portion of the beam, other than the hinge, is considered to be elastic. The hinge exhibits linear elastic behaviour until the stress reaches the tensile strength of the material, at which cracking is initiated. After the initiation of crack, the response becomes nonlinear. The tensile constitutive relation of the concrete (Figure 3.3) governs the later behaviour of hinge, which is modelled as layers of spring elements. The shape of the stress-crack opening curve (*σ*-*w*) is the effect of the fibre yielding and pull-out (pseudo-hardening), and the crack opening profile is assumed to be linear within each branch of the curve.

Following the work of Olesen (2001), the expression for the constitutive relation in the nonlinear hinge model is given as:

$$\sigma = \begin{cases} \varepsilon . E & \text{precrack state} \\ \sigma_w(w) = g(w) . f_t & \text{cracked state} \end{cases} \tag{3.1}$$

$$g(w) = b_i - a_i w, \quad \text{where } w_{i-1} < w < w_i \text{ and } i = 1 \dots n, w_0 = 0 \text{ and } b_1 = 1 \tag{3.2}$$

$$w_i = \frac{b_{i+1} - b_i}{a_{i+1} - a_i}, \text{where } i < n; \quad w_n = \frac{b_n}{a_n} \tag{3.3}$$

and *E*, Young’s modulus, ε, elastic strain, $\sigma_w(w)$, stress crack opening relationship with ‘*w*’ crack opening, f_t, uniaxial tensile strength, b_i, y-intercept of the linear segments, a_i, slope of each linear segment, w_i, limits of the linear branches and n, number of linear segments of the stress-crack opening relationship. Eqn. (11) can be rewritten to obtain the basic parameters required for the construction of σ-w curve as (Jepsen et al., 2016),

$$a_i = \frac{\sigma_i - \sigma_{i-1}}{w_i - w_{i-1}} \tag{3.4}$$

$$b_i = (a_i - a_{i+1})w_i + b_{i+1} \tag{3.5}$$

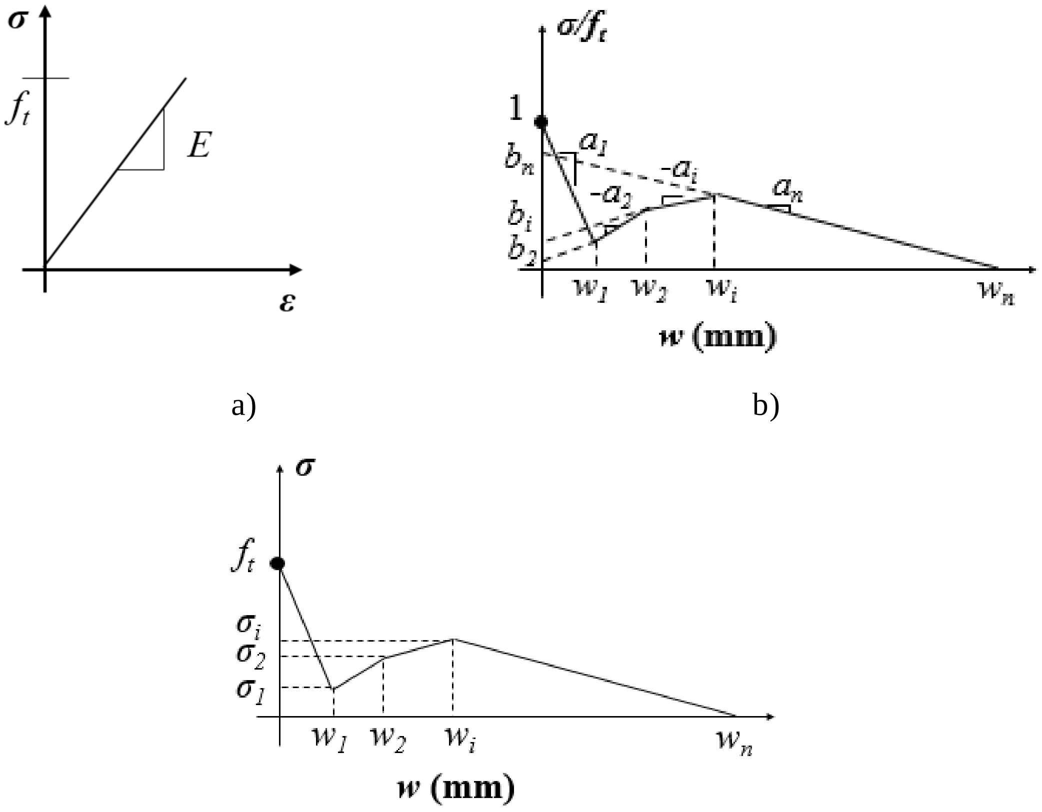

a) b)

c)

Figure 3.3. Model for a) precracked concrete, and b) cracked state with direct parameters, and c) with indirect or derived parameters

When a beam of depth 'H', breadth 'b' and span 'l' is subjected to a load of 'P' at the centre (see Figure 3.4), the hinge undergoes an angular deformation of ϕ. The tensile strain across the crack plane, $\varepsilon^*(y)$, is given by,

$$\varepsilon^*(y) = \frac{(y - y_0)2\phi}{s} \tag{3.6}$$

where y_0 is the neutral axis depth. After cracking, the deformation of a strip, $u(y)$, in the hinge is the sum of the elastic deformation of the strip and the crack opening (shown as the shaded portion of the hinge in Figure 3.5). Also, the deformation can be written as the product of the strain and length of the element and, therefore,

$$u(y) = s\varepsilon^*(y) = s\frac{\sigma_w(w(y))}{E} + w(y) \tag{3.7}$$

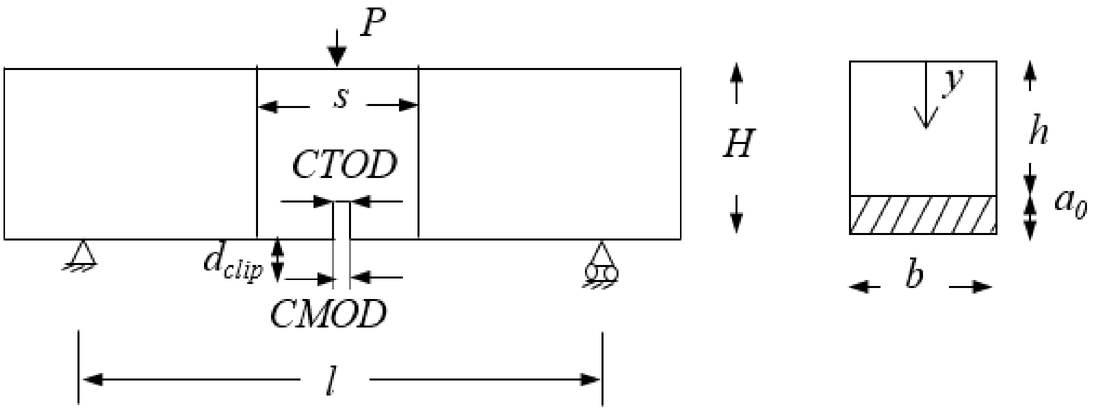

Figure 3.4. Test configuration

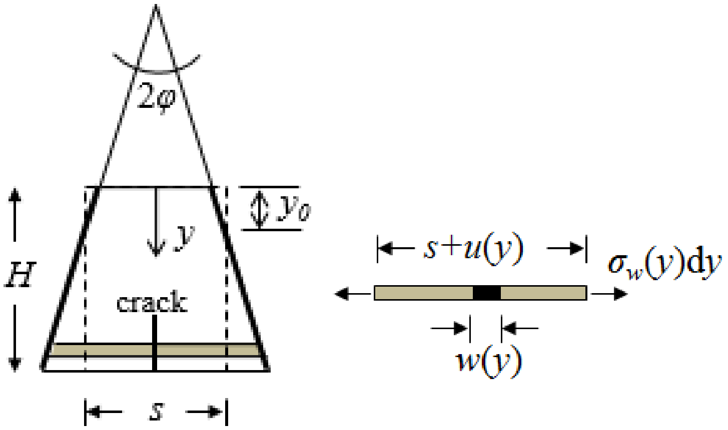

Figure 3.5. Deformation of the cracked hinge

Combining Eqns. (16) and (17), the stress in the horizontal layer of the hinge is found to be

$$\sigma_w(w(y)) = (2(y - y_0)\phi - w(y))(E/s) \tag{3.8}$$

From Eqns. (11) and (12), the following expression can be obtained:

$$\sigma_w(w(y)) = f_t(b_i - a_i w(y)); i \in [1..n] \tag{3.9}$$

Solving Eqns. (18) and (19) for $w(y)$ and $\sigma_w(w(y))$, the following solutions are obtained:

$$w(y) = \frac{2(y - y_0)\phi - \zeta_i}{1 - \beta_i} \tag{3.10}$$

$$\sigma_w(w(y)) = \frac{\zeta_i - 2(y - y_0)\phi\beta_i}{1 - \beta_i}\frac{E}{s} \tag{3.11}$$

where the dimensionless parameters β_i and ζ_i are given by:

$$\beta_i = \frac{f_t a_i s}{E}; \quad \zeta_i = \frac{f_t b_i s}{E} \tag{3.12}$$

The above expressions relate $\sigma_w(w(y))$ with the hinge displacement parameters ϕ and y_0, which define the shape of the stress-crack opening curve and these parameters are essential to obtain the closed-form solution that relates the constitutive tensile relation to the nonlinear flexural behaviour.

As the beam is loaded, the distribution of stresses along the cross-section of the beam prior to cracking will be linear – depicted as ‘Phase 0’ in Figure 3.6. As the load is increased in this stage, the stress developed reaches the tensile strength of the material (f_t) and a crack is formed. As the crack propagates, the stress profile in the cracked region will be nonlinear and is termed as ‘Phase I’. In the first stage of cracking, the stress distribution in the cracked region will be governed by the softening response of the concrete matrix. On further crack propagation, the fibres bridging action predominates and there is continued stress transfer across the crack (Phase II). Similarly, further phases (Phase III and so on) can be defined to reflect other features of the σ-w curve. When the fibres rupture or completely pull out, there is no further stress transfer across the crack, as seen in the distribution corresponding to Phase V.

If a tetralinear model is considered for the σ-w curve, the different crack propagation phases of a beam are as shown in Figure 3.6. Throughout crack propagation, the position of the neutral axis denoted as y_0, changes and can be determined by considering the static equilibrium across the section. The compressive force denoted as C and tensile forces denoted as T_i are obtained after determining the depth of various stress kink points in the sectional stress distribution. The depth of the uncracked region in tension, y* (see Figure 3.6), can be obtained from Eqn. 16 as:

$$y^* = \frac{sf_t}{2\phi E} \tag{3.13}$$

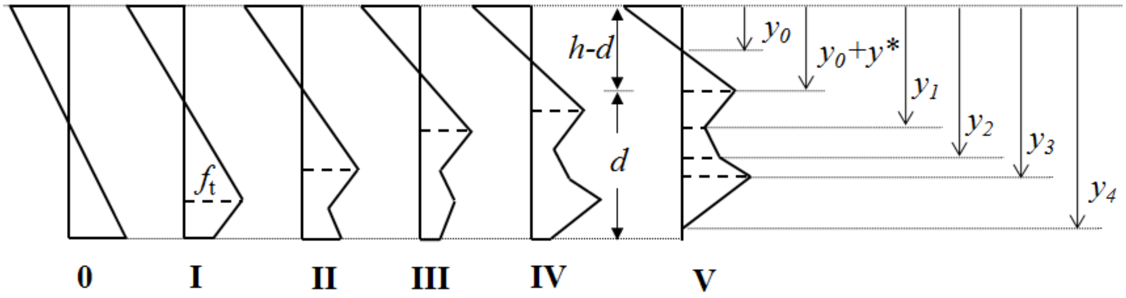

Figure 3.6. Different phases of stress distribution in the ligament

Eqn (20) can be rewritten to obtain the depth of different nonlinear stress kink locations y_i as,

$$y_i = y_0 + \frac{1}{2\phi}(\zeta_i - (\beta_i - 1)w_i) \quad i \in [1..n] \tag{3.14}$$

The stress block of the uncracked region in compression is linear as the compressive stresses are very low at crack initiation. The expressions for the compressive and tensile forces in the uncracked region are given as:

$$C = \frac{f_t b \theta y_0^2}{h} \tag{3.15}$$

$$T_0 = \frac{1}{4\theta} f_t h b \tag{3.16}$$

The forces acting in the cracked region can be obtained from the following Eqns. (27) and (28),

$$\sum_{i=1}^{n} T_i(i) = T_1 + T_2 ... + T_n \tag{3.17}$$

$$T_i(i) = \frac{(\sigma_{i-1} + \sigma_i)}{2} b y_b(i); \text{ where } \sigma_i = f_t(b_i - a_i w_i) \text{ and } y_b(i) = y_{i+1} - y_i \tag{3.18}$$

Now that the depth of neutral axis and forces acting on the stress block are known, the moment (M) due to the sectional stresses can be calculated for a particular σ-w curve. Consequently, the applied load (P) can be achieved (as illustrated in Figure 3.8), and the crack mouth opening displacement (CMOD) can be calculated by taking into account both the elastic (Tada et al., 1973) and inelastic deformations, as (see Figure 3.4):

$$CMOD = CTOD + \frac{24a_0 M v_1(x)}{bh^2 E} + a_0(\phi - \phi_{crack}) \tag{3.19}$$

$$\phi = \frac{2sf_t}{hE}\theta; \quad \phi_{crack} = \frac{2sf_t}{hE}; \quad CTOD = w(h) = \frac{sf_t}{E}\frac{1-b_i+2\alpha'\theta}{1-\beta_i}; \quad \alpha' = \frac{d}{h} \tag{3.20}$$

where the crack tip opening displacement (CTOD) is the value of w at the tip of the notch (see Figure 3.4). Normally, the CMOD is measured using knife edges that hold a clip gauge or an extensometer centred across the notch, in which case a_0 should be substituted with ($a_0 + d_{clip}$), where d_{clip} is the thickness of the knife-edge.

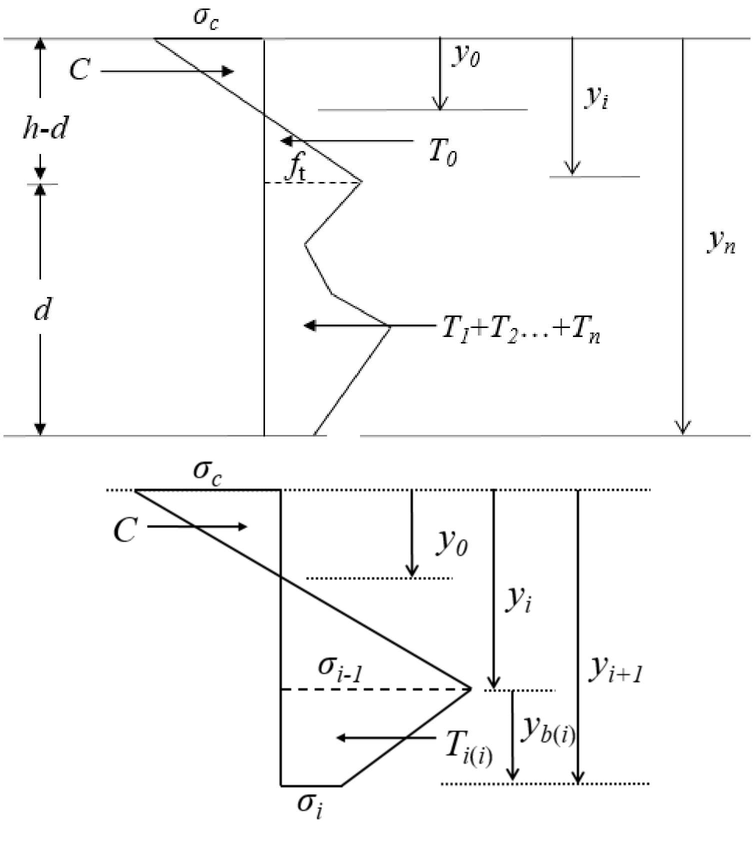

Figure 3.7. Stress distribution for a multi-linear model

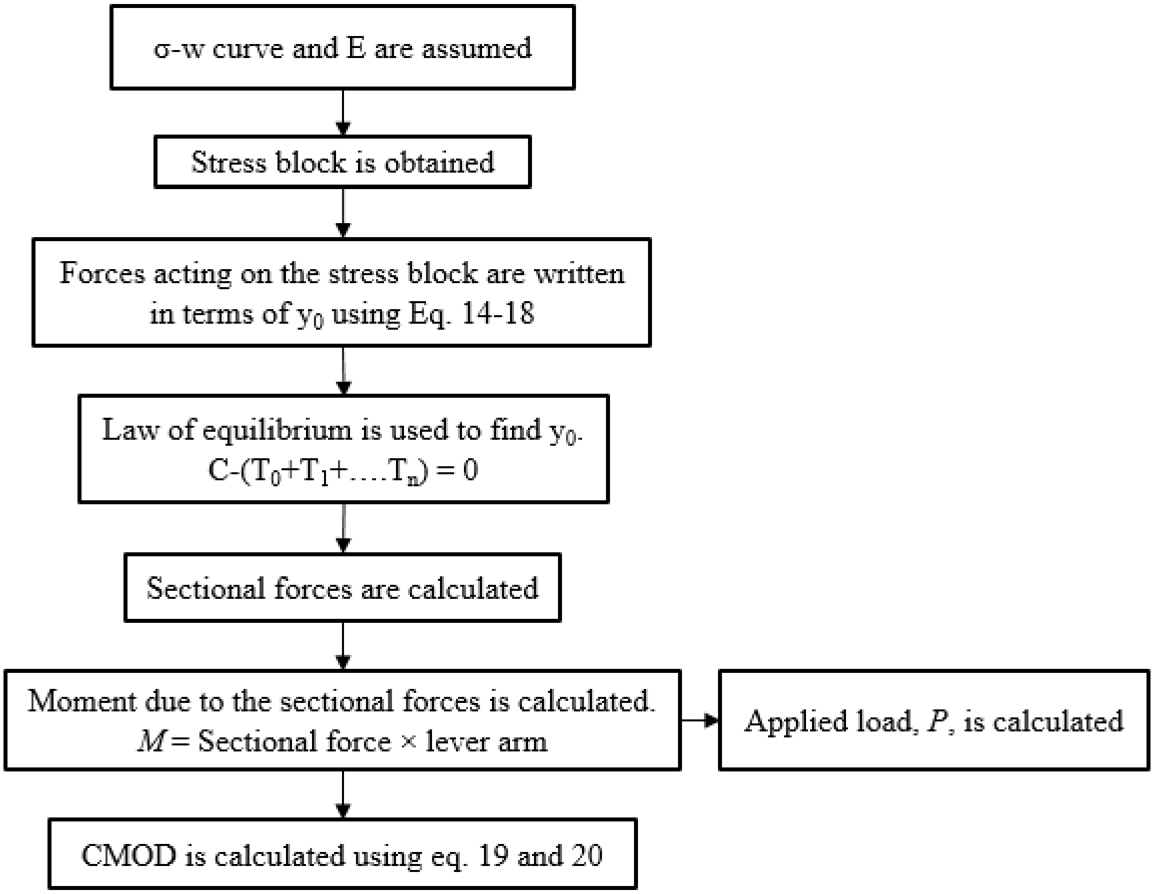

Figure 3.8. Flowchart describing the analytical process

Thus, from the above equations, the complete load-CMOD curve can be attained if the stress-crack opening curve and elastic modulus of concrete are known. The Young's modulus, *E*, can be obtained using the linear elastic fracture mechanics (LEFM) principles, as:

$$E = \frac{6Pla_0}{CMOD\, bH^2} v_1(x) \tag{3.21}$$

where $v_1(x)$ for a beam with a span/depth ratio of 3.33 (Stephen et al., 2018) is,

$$v_1(x) = 0.197 + 17.816x - 107.63x^2 + 338.21x^3 - 494.26x^4 + 298.86x^5;\ x = \frac{a_0}{H} \tag{3.22}$$

Since Young's modulus is an elastic property of a material, it can be determined prior to the inverse analysis by utilizing the linear elastic region of the experimentally-obtained load-CMOD curve.

3.3.3 Optimization algorithm

The parameters involved in the construction of σ-w curve are found through an optimization process, since the complexity of the analytical model can lead otherwise to results that are ambiguous (Roelfstra and Wittmann, 1986; Alvaredo and Torrent, 1987). In the present study, the parameters of the curve that provide the best fit of the test data are identified through a random search algorithm called PGSL, which has been used to solve system identification problems in the areas of structural monitoring and optics (Raphael and Smith, 2003). PGSL employs random sampling in order to find the global minimum of a user-defined objective function. Seed values are generated by randomly selecting values of optimization variables within the specified range. A probability density function (PDF) is created for each variable, which is used to generate the values. Initially, a uniform PDF is used and as the optimization advances, higher probability is assigned to the areas where good solutions are found. In this process, a more intense search is performed in the neighbourhood of good solutions and the solution later converges to a local optimum, after which the search is restarted by selecting a subdomain, centred around the current best point (i.e., the point with least error). With such multiple restarts, the regions containing different local optima are explored, giving a high probability of finding the global optimum.

In order to determine the best solution or combination of values of the model parameters, the optimization algorithm minimizes the error between the predicted response and the experimental data. Here, the parameters include the stress points and the corresponding crack openings at the kinks of the σ-w curve (see Figure 3.3c). The error in fitting is computed as the sum of squares of differences between the two curves and is given by,

$$Error = \sqrt{\sum_{i=1}^{n} (P_i^{\exp} - P_i^{th})^2} \tag{3.23}$$

where P_i^{exp} and P_i^{th} are the experimental and analytically-predicted loads at the i^{th} point of the load-CMOD curve.

3.3.4 Comparison of different models for the *σ*-*w* curve

As discussed earlier, bi-, tri- and multi-linear models have been used to represent the *σ*-*w* curves of FRC. In the optimization process for obtaining the parameters of these models, the post-peak region of the load-CMOD curve dominates the error due to the large number of data points compared to the pre-peak region and consequently, the matrix response may not be adequately represented (Barragán, 2002). One way of compensating this is to have weighting functions for giving priority to certain regions of the load-CMOD curve, say the peak load, by reducing the acceptable error levels there compared to other regions (Sousa and Gettu, 2006). The need for weighting functions for the three different orders of *σ*-*w* models have been examined here by comparing the analyses without any weighting function (W1) or equal weightage (i.e., 1) for all regimes of the response, and with a higher weightage (W2) at the first peak (as seen in Figure 3.9). In the case W2 with weightage being applied, a linear increase in weightage in the pre-peak regime until the first peak, followed by linear decrease has been considered. Here, the weightage at the peak is set at 10, which reflects 10 times the weightage for the error than in the post-peak regime, where the weightage is 1. Consequently, the fitting error Eqn. (33) is modified to accommodate the weighting function, as (Sousa and Gettu, 2006):

$$Error = \sqrt{\sum_{i=1}^{n} \psi_i (P_i^{\exp} - P_i^{th})^2} \tag{3.24}$$

where ψ_i is the weighting function at the i^{th} point of the load-CMOD curve. For the purpose of the assessment, the test results of FRCs exhibiting softening (M40SF20) and hardening type (M40SF45) responses have been used. It can be seen in Figure 3.10 that both the trilinear and tetralinear models yield good fits without the need for the weighting function in the case of a softening-type load-CMOD curve. On the other hand, the bilinear model requires the weightage to yield a satisfactory fit in the peak region (Figure 3.10a) or else the peak load is under-estimated by about 8%.

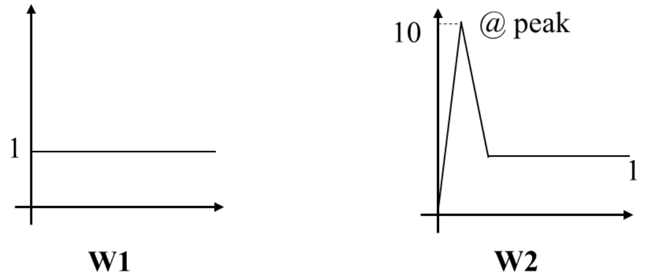

Figure 3.9. Weighting considered in the robustness analysis: W1: uniform weight; W2: higher weight at the peak

In the case of FRC with strain-hardening type response, the fits obtained with the bilinear model are unsatisfactory as the first-peak is not captured, both without and with weightage (Figure 3.11a). The higher order models perform better, with a significant improvement in the fit with the trilinear model by use of weightage (Figure 3.11b). The tetralinear model, however, is found to yield the best fits with practically no difference seen with the weightage (W1 and W2), which confirms that the model has enough parameters to represent all parts of the response adequately (Figure 3.11c). It can, in general, be concluded that the trilinear model would require the use of weighting functions to emphasize the response at the peak. Further, the tetralinear model yields good fits in both strain-softening and hardening type responses, without the need for weightage, making the analysis more objective. Therefore, further discussion in this work will be restricted only to the tetralinear model.

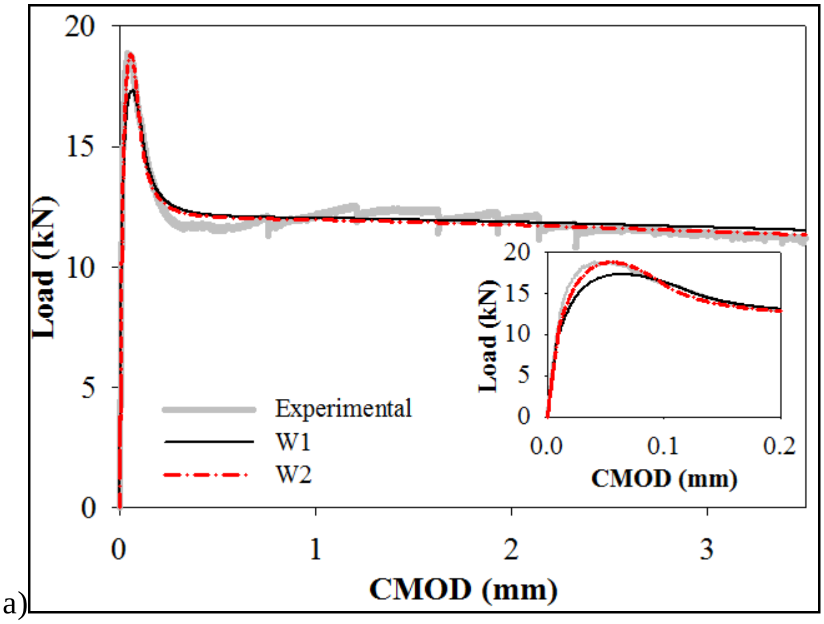

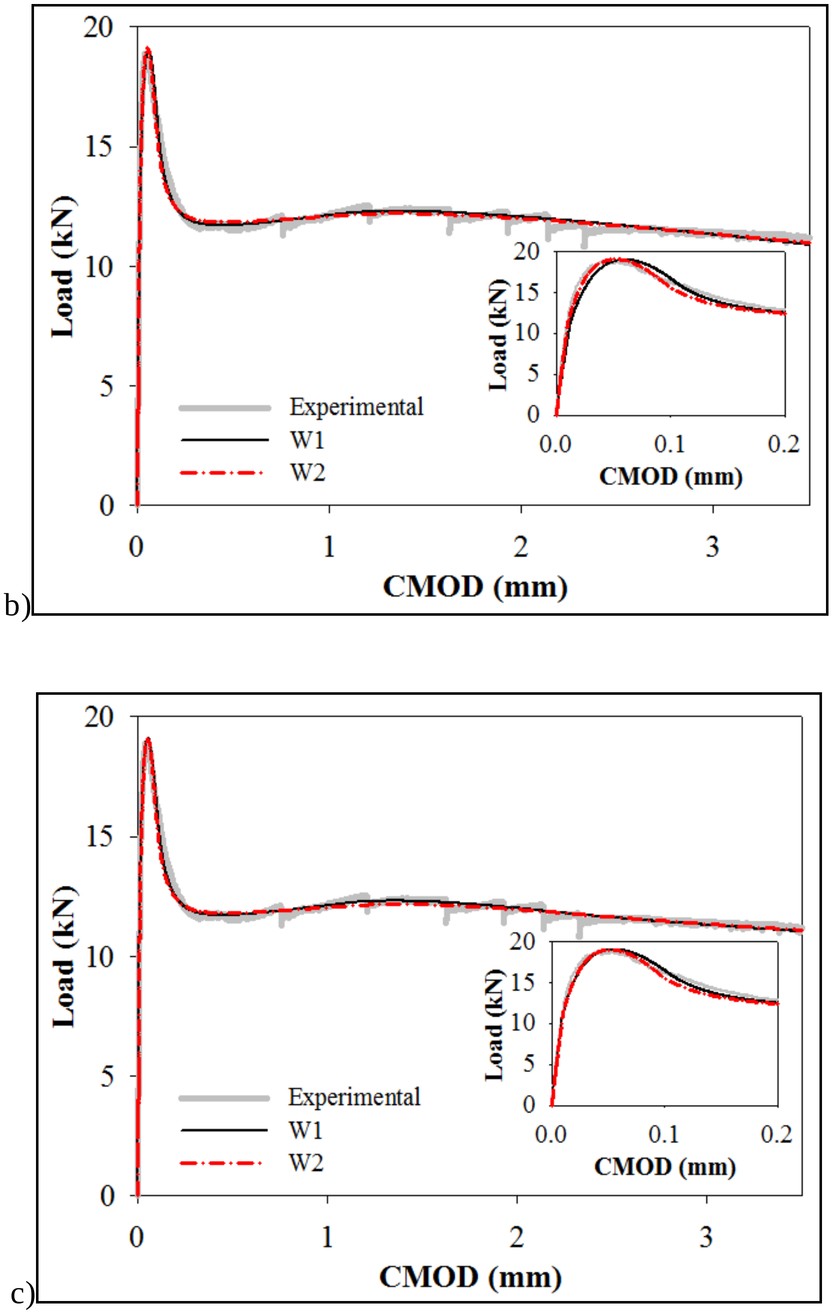

Figure 3.10. Fitting of strain softening type response with a) bilinear, b) trilinear and c) tetralinear models, without (W1) and with (W2) weighting function

a)

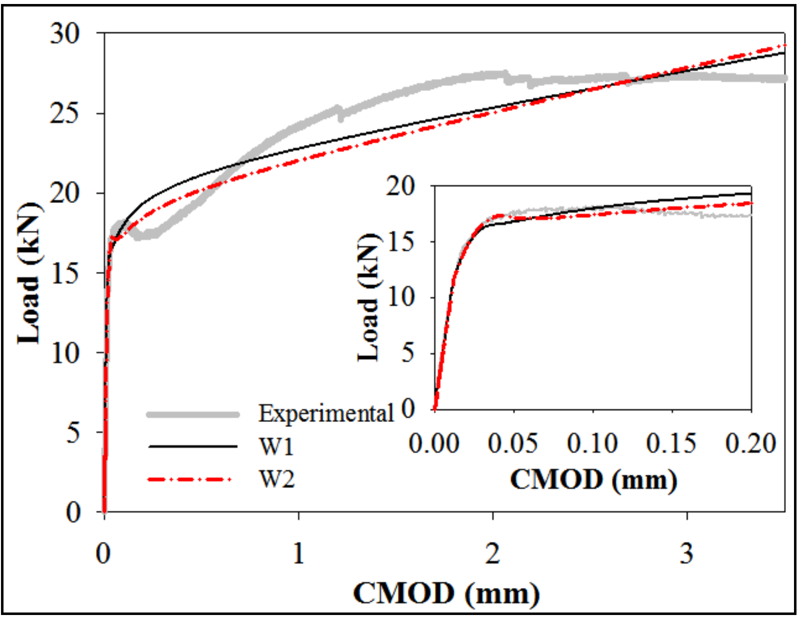

Load (kN)
30
25
20
15
10
5
0
0
1
2
3
CMOD (mm)
Experimental
W1
W2
Load (kN)
20
15
10
5
0
0.00
0.05
0.10
0.15
0.20
CMOD (mm)

b)

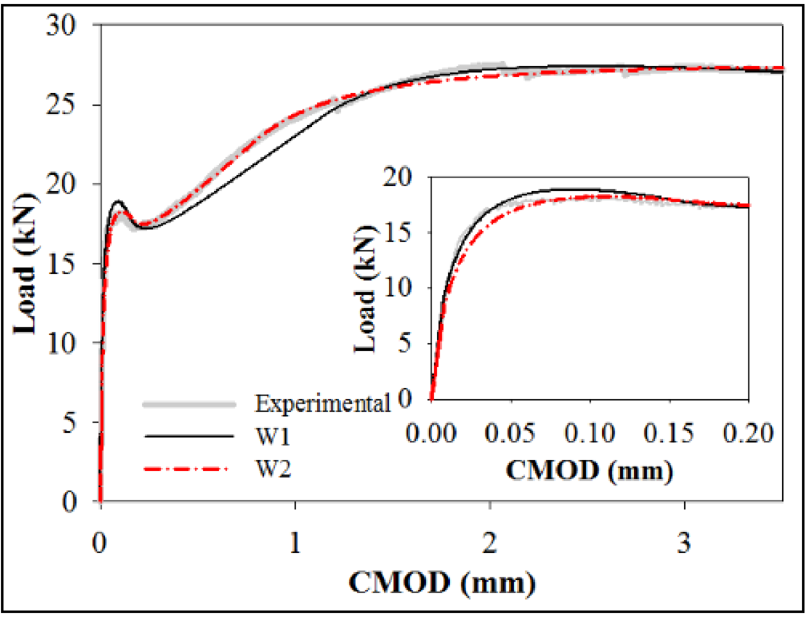

Load (kN)
30
25
20
15
10
5
0
0
1
2
3
CMOD (mm)
Experimental
W1
W2
Load (kN)
20
15
10
5
0
0.00
0.05
0.10
0.15
0.20
CMOD (mm)

c)
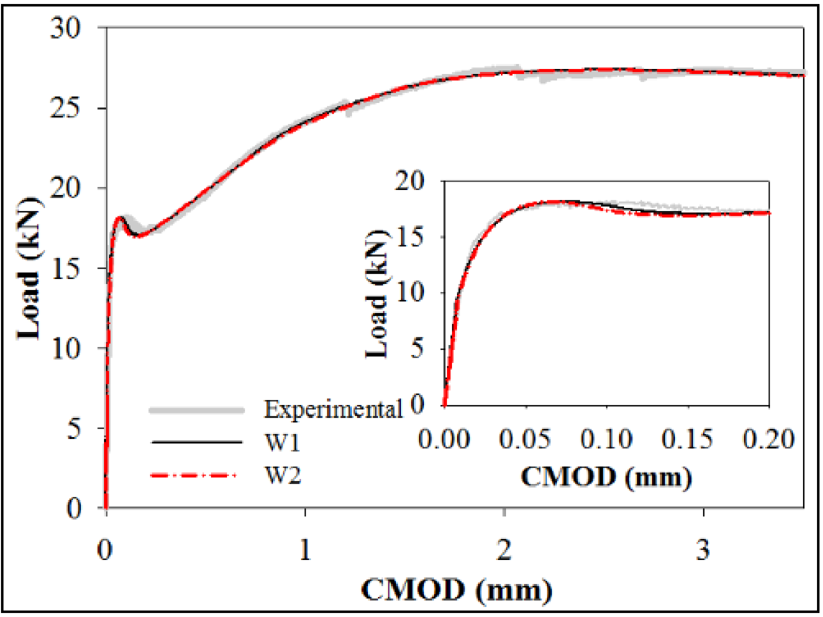

Figure 3.11. Fitting of strain hardening type response with a) bilinear, b) trilinear and c) tetralinear models, without (W1) and with (W2) weighting function

3.3.5 Range of fitting variables

As mentioned earlier, the optimization algorithm used finds a solution for each variable of the model within the specified range. The robustness of the tetralinear model has been further evaluated by varying the range of the fitting variables involved in the construction of the σ-w curve and checking the ability of the algorithm to yield a single solution irrespective of the prescribed range. Usually, it is better to prescribe narrow ranges for the parameters to restrict the optimization time, which could be obtained from the literature (Barragán et al., 2003) or previous fits. This is because a wide range would require more computational time due to many local optima that have to be resolved. Nevertheless, this may be required if a narrower range cannot be chosen a priori. For illustration, the values for the variables of the tetralinear model, viz. f_t, σ_1, σ_2, σ_3, w_1, w_2, and w_3, have been obtained considering narrow and wide ranges of the parameters as shown in Table 3.2, and the fits and the σ-w curves are seen in Figure 3.12. The parameters obtained using both the wider and narrow ranges are similar, indicating that the range prescribed does not influence the optimization significantly in the tetralinear model.

Table 3.2. Fitting ranges and the optimization values obtained

	f_t (MPa)	σ_1/f_t	σ_2/f_t	σ_3/f_t	w_1 (mm)	w_2 (mm)	w_3 (mm)
Narrow range	[2; 6]	[0; 1.5]	[0; 1.5]	[0; 1.5]	[0; 0.1]	[0.11; 1]	[1.1; 3]
Values obtained	3.04	0.64	0.97	1.07	0.08	0.55	1.15
Wider range	[0; 100]	[0; 100]	[0; 100]	[0; 100]	[0; 15]	[0; 15]	[0; 15]
Values obtained	3.24	0.60	0.93	0.99	0.07	0.58	1.22

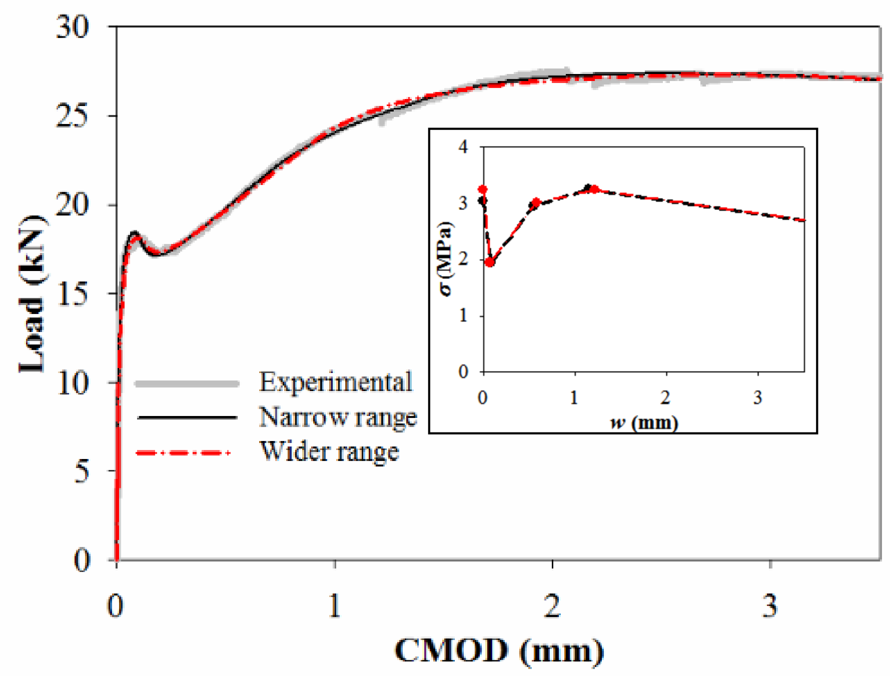

Figure 3.12. Optimization using different ranges of fitting variables

3.3.6 Parametric study

A sensitivity analysis of different parameters of the tetralinear model on the load-CMOD curve has been performed to understand their influence, and to help in troubleshooting during the simulation. In this analysis, the parameter under consideration is varied while the other variables are kept constant. For the sake of discussion, a typical load-CMOD curve for FRC is split into five different regions as shown in Figure 3.13.

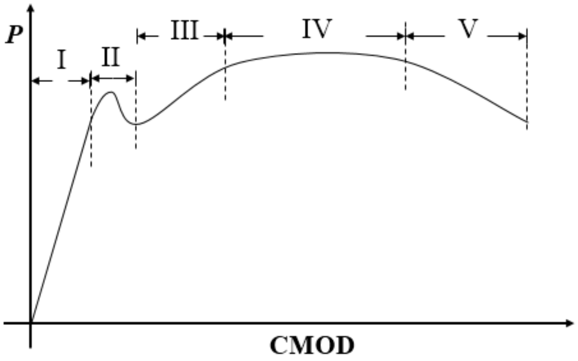

Figure 3.13. Diagrammatic illustration of different regions in the load-CMOD curve

As seen in Figure 3.14, the influence of the elastic modulus (*E*) of concrete is high in the linear part of the load-CMOD curve (Region I), though the entire curve shifts upward slightly with an increase in the *E*-value. A change in the tensile strength (f_t) produces a shift in the nonlinear regions of the load-CMOD curve, as the other stress-based parameters are defined as multiples of the tensile strength, causing a corresponding change in the flexural load-carrying capacity and toughness (Figure 3.15).

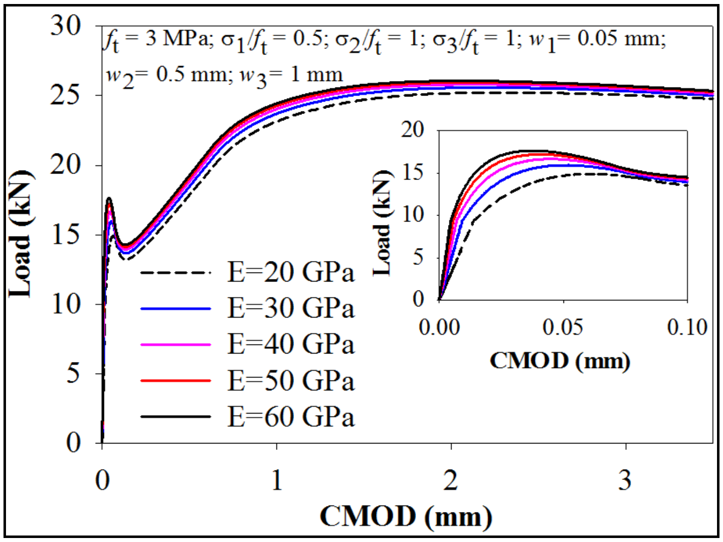

Figure 3.14. Variation of the Load-CMOD curve with the Young's modulus

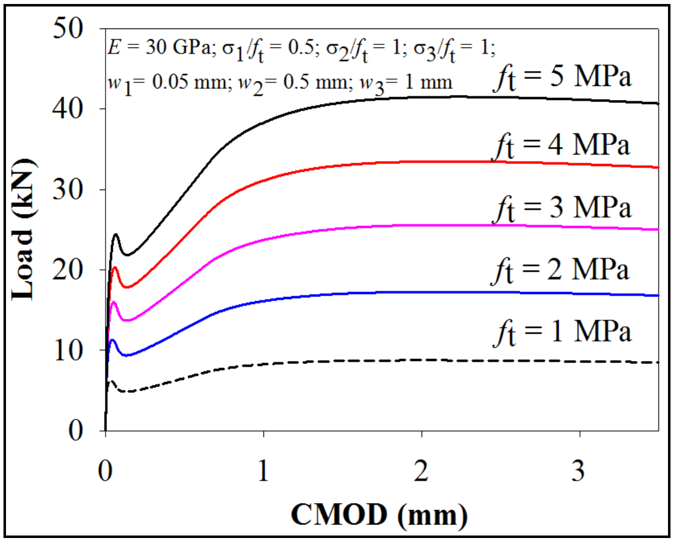

Figure 3.15. Variation of the Load-CMOD curve with the tensile strength

To understand the influence of stress and crack opening parameters of the σ-w curve (refer Figure 3.3c), each has been varied individually, and found that σ_1/f_t and w_1 have major influence on Regions II and III (Figure 3.16), σ_2/f_t and w_2 affect Regions III and IV (Figure 3.17), and σ_3 and w_3 control Regions IV and V (Figure 3.18). The critical crack width (w_c), beyond which the bridging stress drops to zero and the crack becomes a traction-free crack, is found to have only a minor effect on the tail (Region V) of the load-CMOD curve (Figure 3.19), at least until a CMOD of 3.5 mm. So, for the analysis purposes, a quarter-length of the fibre is considered as the critical crack opening in the further analysis (Soetens and Matthys, 2014).

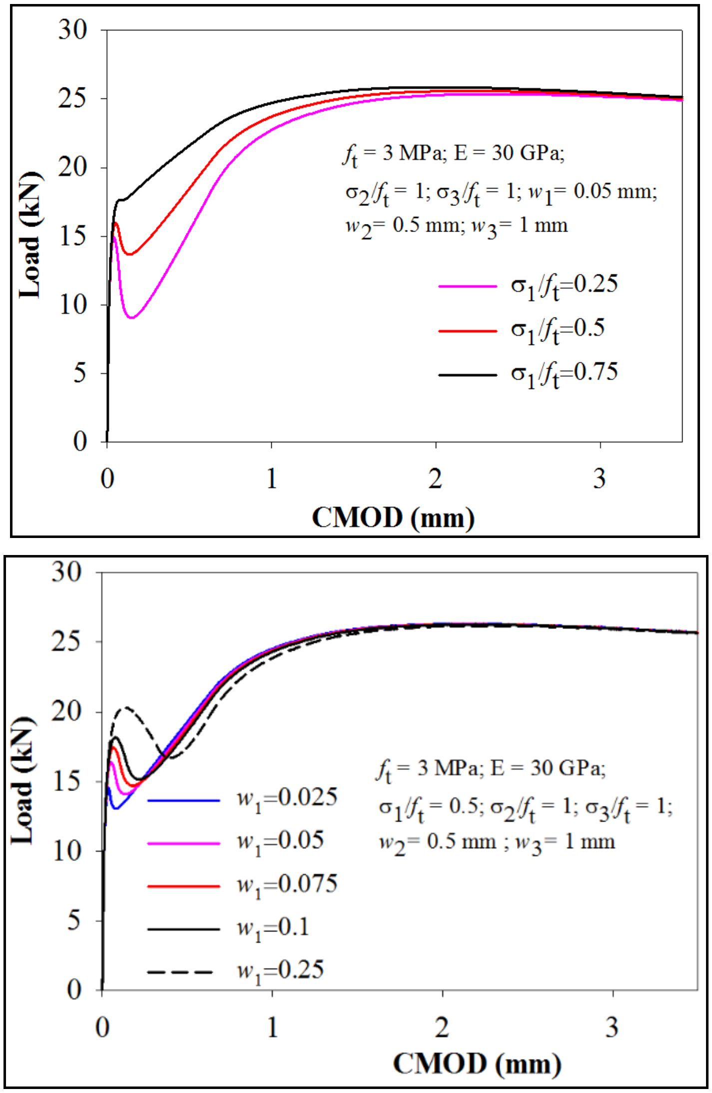

Figure 3.16. Variation of the Load-CMOD curve with σ_1 and w_1

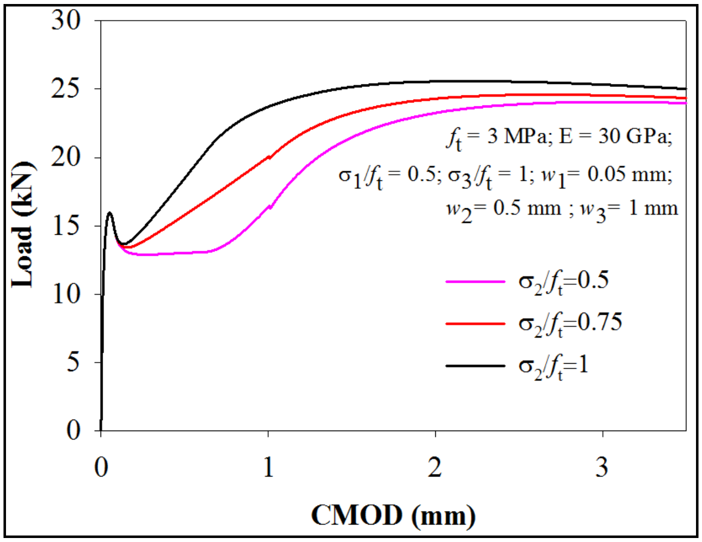

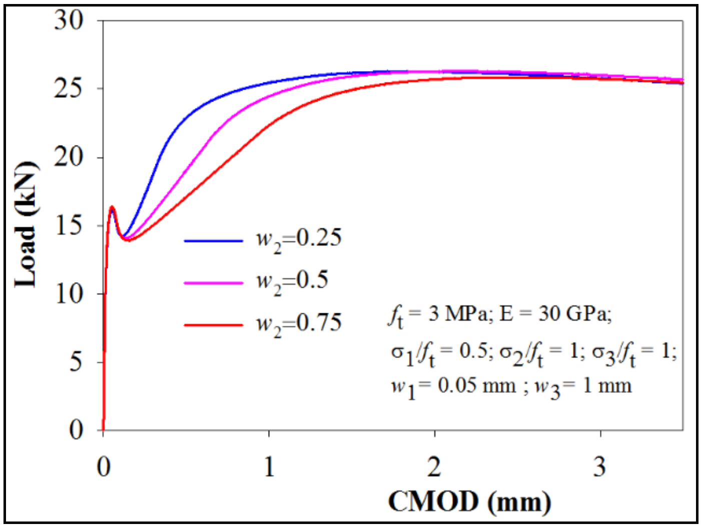

Figure 3.17. Variation of the Load-CMOD curve with σ_2 and w_2

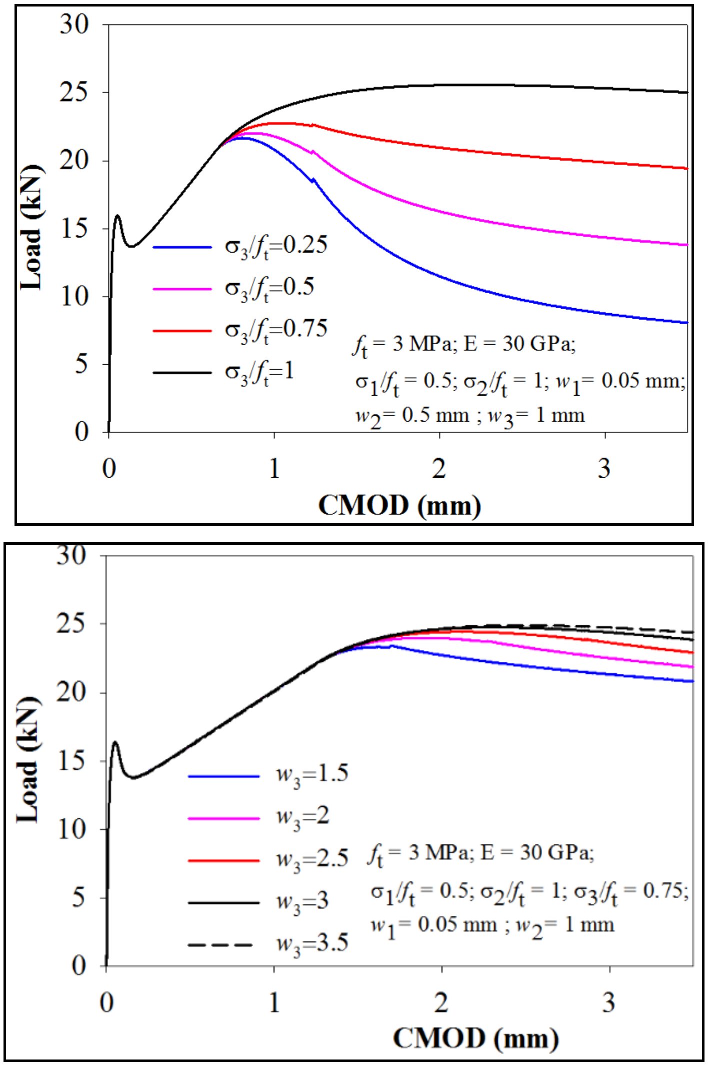

Figure 3.18. Variation of the Load-CMOD curve with σ_3 and w_3

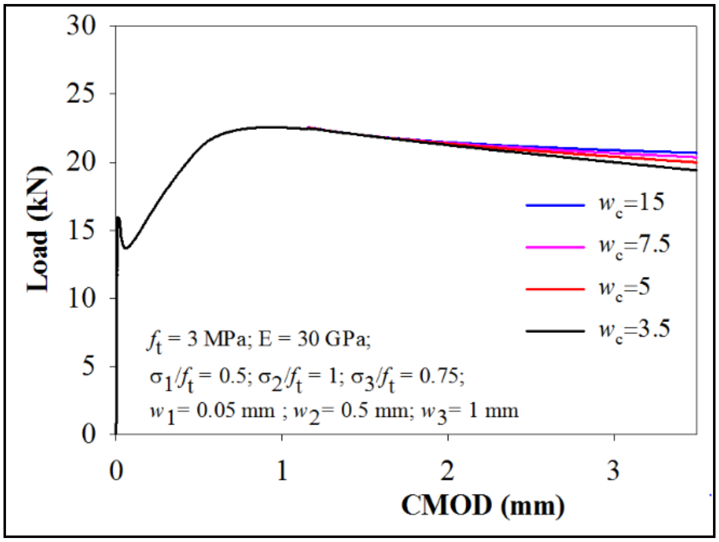

Figure 3.19. Variation of the Load-CMOD curve with the critical crack length

3.4 APPLICATION OF INVERSE ANALYSIS PROCEDURE TO FRC

The inverse analysis approach has been applied to the experimental data of Jose et al. (2018) for concrete with design compressive strength of about 40 MPa (designated as M40), having the proportions of cement: sand: coarse aggregate: water as 1:2:3:0.45, incorporating portland pozzolana cement and aggregates with the maximum size of 20 mm, with different dosages of commonly used cold drawn hooked-ended steel (SF) and polypropylene fibers (PF). The test procedure followed for the flexural toughness characterization conforms to the EN 14651:2005 (E) Standard and the Recommendations of RILEM TC 162-TDF. The configuration of the three-point bend (3PB) notched prism is given in Figure 3.4, using which the load versus crack mouth opening displacement (load-CMOD) curve is obtained. The dimensions of the beam are 150×150×700 mm, with a span of 500 mm; a notch of 25 mm depth is cut at the mid-span of the beam. The notation for each type of concrete is given by the strength of the concrete, type of fiber incorporated and its dosage in kg/m^3; e.g., M40SF30 denotes the 40 MPa grade concrete with steel fibers at 30 kg/m^3 dosage. The experiments have been performed under closed-loop control, which is essential for obtaining a stable response (Gettu et al., 1996). Six concrete beams were tested for each type of concrete, and the average load-CMOD curves are shown in Figure 3.20, The typical load-CMOD curves exhibiting softening and hardening responses are shown in Figure 3.20, and the corresponding *σ*-*w* curves obtained from the inverse analyses are given in Figure 3.21. It can be seen that the bridging stresses (σ) increase with the fibre dosage, in accordance with the load-CMOD curves in Figure 3.20, reflecting the increase in toughness.

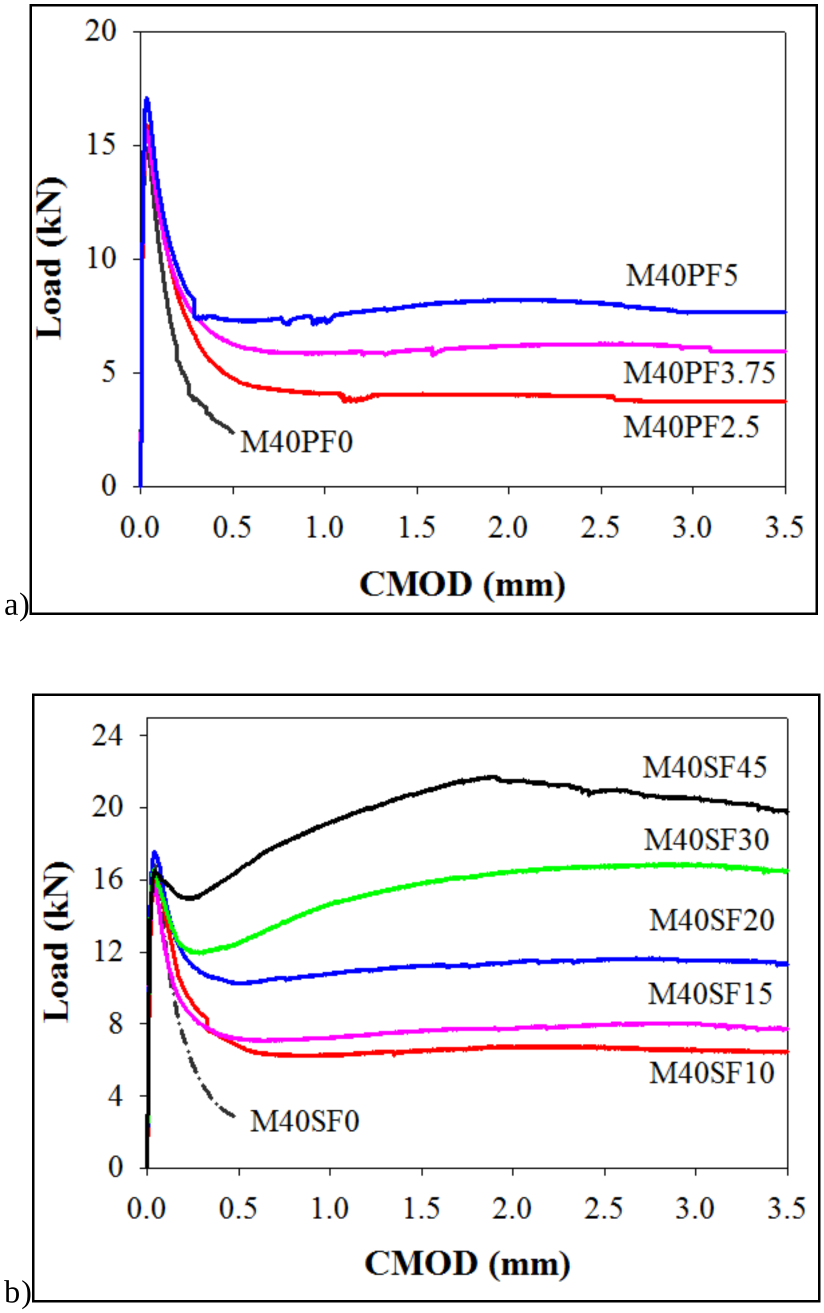

Figure 3.20. Average load-CMOD curve for concrete reinforced with a) steel and b) polymer fibres

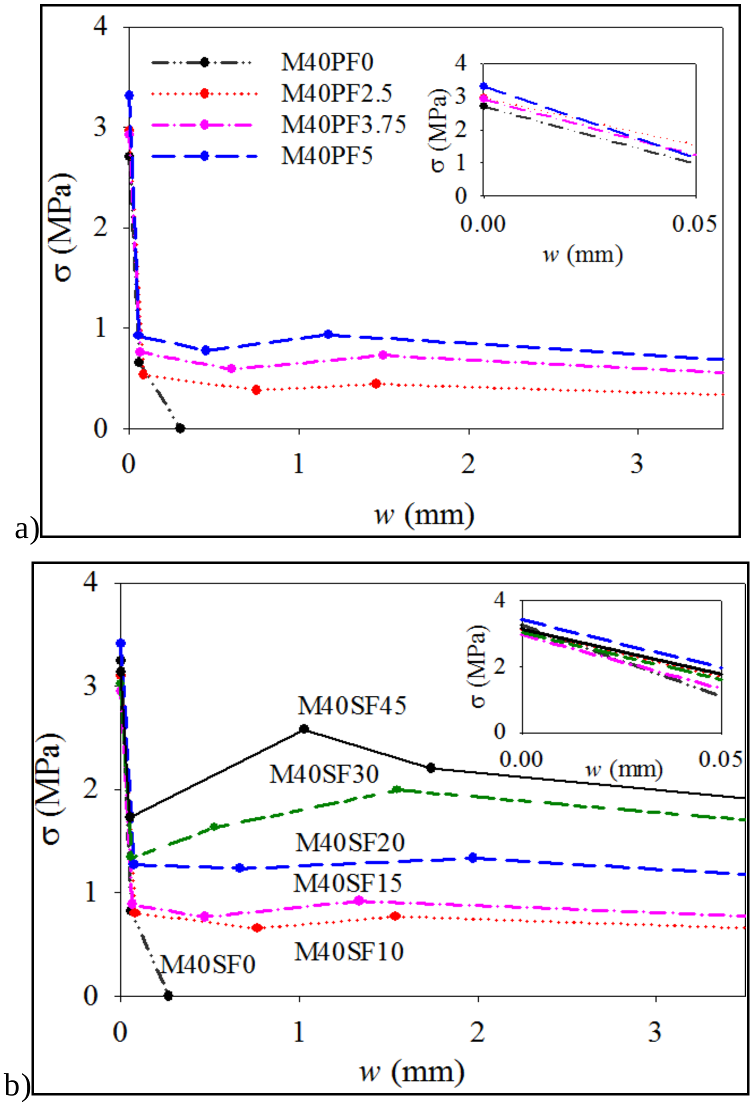

Figure 3.21. Tetralinear σ-w curves for concrete with a) steel and b) polymer fibres

3.5 VALIDATION OF ANALYTICAL MODEL

For validation of the analytical model and to assess the unambiguity of the parameters of the σ-w curve, the results of the inverse analysis for M40SF30 have been used to predict the responses of beams different from that of the standard test and comparisons are made with the relevant experimental data.

3.5.1 Unnotched beam

The first prediction is made with finite element modeling for a third-point loaded unnotched beam (JSCE Part III-2 (SF1–SF4), 1984), using the smeared crack approach

(Rots and Blaauwendraad, 1989) in the TNO DIANA v6 code. The beam is represented by a mesh of quadrilateral elements, and the order of the analysis is quadratic and Gauss integration rule is used. The analysis is done with the element width being kept equal to the hinge width used in the analytical model (i.e., 75 mm). The σ-w curve is converted to a tensile stress-strain curve by dividing the crack width by the element width. The prediction is found to be well within the band of experimental data, as seen in Figure 3.22.

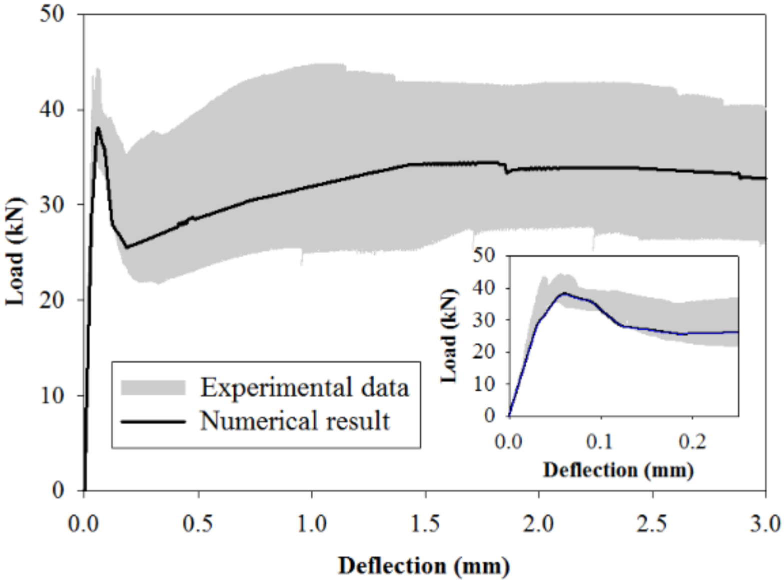

Figure 3.22. Comparison of the predicted load-deflection curve for an unnotched beam with experimental data

3.5.2 Notched beam with different geometry

Further, the responses of the notched beams tested under three-point bending with different notch depth and span from the standard specimen have been modeled using the discrete crack approach in the TNO DIANA v6 code. The mesh sensitivity assessment on the numerical model can be found in Appendix A. A cohesive crack model for tensile (Mode I) fracture is implemented through interface elements, and the uncracked region is modeled using a mesh of triangular and quadrilateral finite elements. The 7-point Gauss rule in triangular elements and the 3-point Newton-Cotes rule in the interface elements have been used for integration. In this case, the interface is placed along the likely crack path. The numerical results obtained are found to be within the experimental band of data upto a CMOD of about 2 mm as seen in Figures 3.23 and 3.24. The overestimation in the tail region can be attributed to the reduction of the fracture process zone length when the crack reaches the edge of the specimen, which becomes more significant in these specimens with short ligament lengths (Stephen et al., 2018).

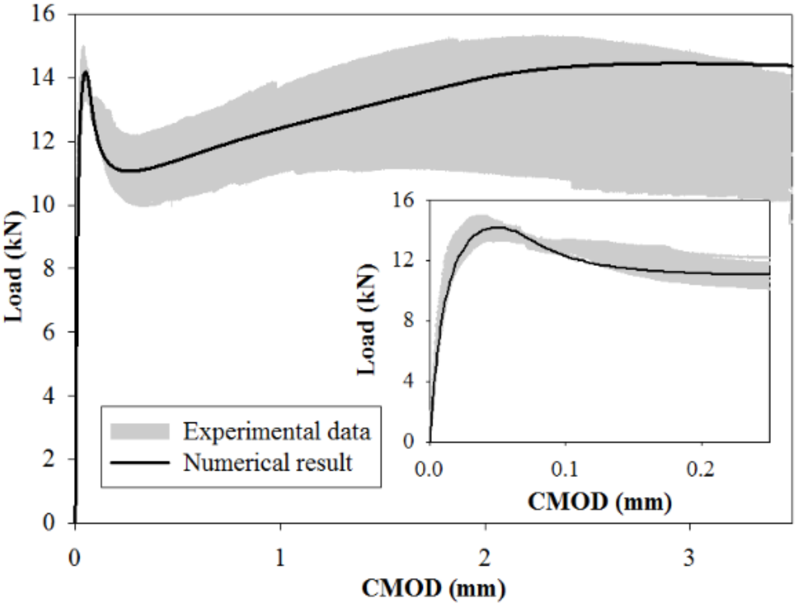

Figure 3.23. Comparison of numerically obtained load-CMOD curve for beam with span=600 mm with experimental data

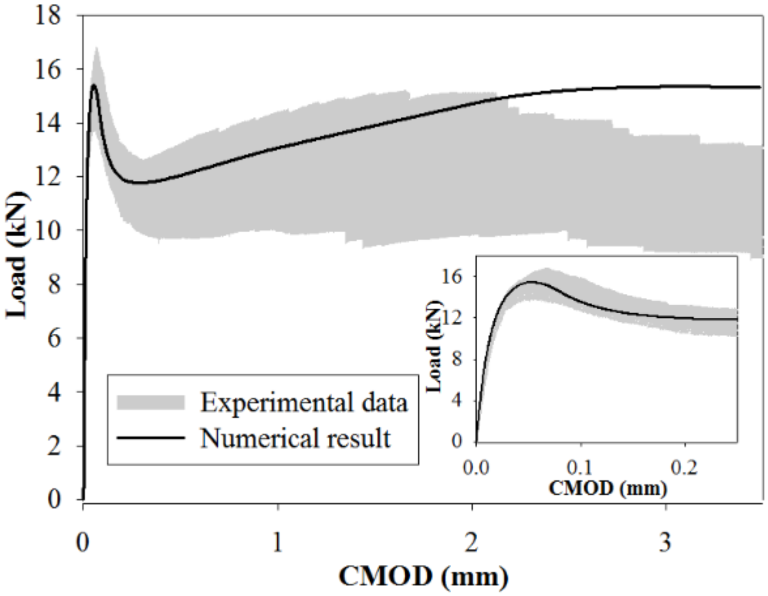

Figure 3.24. Comparison of numerically obtained load-CMOD curve for beam with notch length=30 mm with experimental data

3.6 CONCLUSIONS

A closed-form solution for relating the multi-linear stress-crack opening relation of fibre reinforced concrete (FRC) to the load-CMOD curve has been obtained by extending the cracked hinge model. The parameters of the σ-w curve for FRC with steel and polymer fibres have been found by inverse analysis of experimentally-obtained results using an optimization method based on the PGSL algorithm. From the assessment of different models (i.e., bi-, tri- and tetra-linear), it is found that the bilinear model does not represent the hardening response of FRC satisfactorily, with the usage of a weighting function. Trilinear and tetralinear models gave satisfactory results for FRCs with both softening and hardening flexural response, although the trilinear model requires a weighting function at the peak load for better fitting. The tetralinear model of the σ-w curve is found to be robust as it does not involve any weighting functions and is not affected by the choice of the range of the fitting variables. A parametric study has been performed on the tetralinear model to demonstrate how the fracture parameters are related to different aspects of the flexural response, which could help troubleshoot problems during simulation. The model is validated by predicting the flexural response of unnotched and notched beams, and comparing the results with experimental test data. It is seen that the σ-w curve obtained using the standard specimen could lead to an overestimation of the load-carrying capacity in latter part of the fracture response, which is attributed to the interaction of the fracture process zone with the edge of the specimen.

4 RATE-DEPENDENCE OF THE FRACTURE PROPERTIES IN THE QUASI-STATIC REGIME

4.1 INTRODUCTION

The compressive strength and tensile properties of concrete have shown to exhibit a dependency on the loading rate. Since FRC is used in applications such as tunnel linings and industrial slabs, where the members must resist loads ranging from dynamic to sustained loading, it would be useful to incorporate such rate effects in the analysis and design of FRC structures. The influence of impact loading on the fracture properties of FRC, has been investigated by various researchers. However, the effects of very low loading rates on the fracture behaviour of FRC has not been explored extensively. The influence of slower loading rates on fracture behaviour is important for the analysis of FRC structures, specifically tunnel lining, which has cracks propagating slowly during service life due to soil pressure and ground settlement.

This chapter exclusively deals with the study of static fracture, ranging from quasi-static to slow loading rates, thereby considering creep effects. Three-point bending tests are performed at crack mouth opening displacement (CMOD) rates covering 5 orders of magnitude and the variation of fracture properties (from inverse analysis) is compared to obtain trends. The underlying mechanism of rate-dependent crack propagation is investigated by using the obtained fracture properties as input in the finite element model. The variation of rate-dependence of concrete with different type and dosage of fibres is assessed to determine the benefits of fibre inclusion.

4.2 RATE EFFECTS OF PLAIN AND FIBRE REINFORCED CONCRETE

Substantial studies have been carried out on the impact response of fibre reinforced concrete (FRC), where the incorporation of fibres is found to increase the strength, as well as the energy absorption, at high loading rates (Soufeiani et al., 2016) due to the rate-sensitivity of the concrete matrix and tensile response of the fibres (Naaman and Gopalaratnam, 1983). Similarly, the response of FRC at low loading rates or long-term loads can be related to that of the concrete matrix, as well as the fibre pull-out behaviour, and is of significant relevance for structures that could experience slow crack growth, e.g., embedded concrete structures subject to soil settlement. Under slow loading, creep mechanisms influence the fracture behaviour of the concrete matrix and consequently the failure loads decrease (Bažant and Gettu, 1992). The relaxation of the tensile stresses in the fracture process zone (FPZ) ahead of the crack-tip, which is attributed to time-dependent stress-crack opening response, and the lower fracture energy often results in longer cracks (Rosa et al., 2012). The decrease in fracture resistance is also manifested in fracture surfaces that are more tortuous at slower loading rates (Mechtcherine, 2009), indicating propagation through low resistance paths as opposed to the straighter and multiple cracking that occurs at higher loading rates.

There has been limited investigation of the fracture response of FRC subjected at slow loading rates. Recent fibre pull-out studies have shown the bond strength to decrease with loading rates due to the time-dependence of the fibre-matrix interaction and tensile strength of the fibre. However, for fibres with good tensile strength and strong bond response, such as hooked-ended steel fibres, the pull-out behaviour has been found to be significantly less rate-sensitive (Banthia, 1990; Babafemi and Boshoff, 2017). On the other hand, the behaviour for polypropylene fibres is highly rate-sensitive as they undergo creep and there is progressive softening in the fibre-matrix interface at longer loading durations (Nieuwoudt and Boshoff, 2017; Babafemi et al., 2018). From tests of notched beams, Zhang et al. (2014) observed that the flexural strength and fracture energy of concrete with a volume fraction of 0.8% of hooked-ended steel fibres decreased by about 10% as the loading rate was reduced over 3 orders of magnitude. However, Meng et al. (2017) obtained about 40% reductions in the tensile and bridging strengths for a ultra-high-performance fibre reinforced concrete with a volume fraction of 2% of steel fibres (as a combination of straight and hooked-ended fibres). Bernad et al. (2002) concluded, from relaxation tests on plain and steel fibre reinforced concrete beams, that the bridging stresses in the fracture process zone reduce with time under load, which could lead to the decrease in flexural strength and post-crack load-carrying capacity observed at slower loading rates. Further research is warranted for better understanding of the time-dependence so that its implications for FRC applications can be assessed.

The objective of the present study is to understand the loading rate-dependence of the fracture response in FRC through tests with crack mouth opening displacement

(CMOD) rates varying over five orders of magnitude. Notched specimens of concrete reinforced with steel fibres (SF), at three dosages, and polymer fibres (PF) have been tested under three-point bending, and inverse analysis (Olesen, 2001; Sousa and Gettu, 2006; Stephen et al., 2019) has been employed to obtain σ-w curves from the experimental load-CMOD response. The trends observed have been modelled empirically for use in structural analysis and design. Fracture analysis, based on the finite element method, is used to simulate the development of the FPZ at different loading rates for substantiating the conclusions.

4.3 EXPERIMENTAL PROGRAM

4.3.1 Specimen preparation

The present study is based on fracture tests of concrete with 28-day characteristic cube strength of 40 MPa (having proportions of cement: sand: coarse aggregate: water as 1:2:3:0.45 and incorporating portland pozzolana cement and maximum aggregates of 20 mm size). The fibres described in Table 4.1 have been incorporated in the concrete; note that the volume fraction corresponding to 3.75 kg/m^3 of polymer fibres is 0.4%, which is the same for 30 kg/m^3 of steel fibres, whereas the toughness of the polypropylene fibre reinforced concrete (PFRC) is expected to be similar to that of concrete with 10 kg/m^3 of steel fibres. Six batches of concrete were made for each type, and 5 concrete beams were cast from each batch, along with cubes for compressive strength assessment.

Table 4.1. Details of the fibres

Parameter	**Steel**	**Polypropylene**
Fibre geometry	Hooked-ended	Straight
Specific gravity (g/cc)	7.8	0.92
Tensile strength (MPa)	1225	620
Length (mm)	60	40
Diameter (mm)	0.75	0.44
Dosages	10, 30, 45 kg/m^3	3.75 kg/m^3

Six beams of each concrete were tested, at the age of 28 days, for every loading rate, drawing one from each batch. The beams, with the dimensions of the specimen being 700×150×150 ($L \times b \times h$) mm, were demoulded the next day of casting and subsequently cured in mist room (100% humidity) for 28 days. A notch of depth (a_0) 25mm is cut before testing at the face perpendicular to the direction of casting.

4.3.2 Three-point bending test (3PBT)

The deformation-controlled three-point bending tests were performed in a 1 MN MTS closed loop servo-hydraulic system with a 100 kN load cell, under constant CMOD rate; the CMOD rates used are 100, 10, 1, 0.1 and 0.01 μm/s. The procedure used for the notched beam tests conforms to EN 14651:2005 (EN 14651, 2005), with span (l) of 500 mm. The beam was loaded (F) such that the direction of casting is perpendicular to the loading direction (Figure 4.1). The CMOD was measured using a clip gauge mounted on knife edges across the notch faces. The fastest loading rate takes only 35 seconds to complete, while the slowest takes 5 days to complete. The specimens for the tests with the longest duration were sealed by wrapping with aluminium foil to prevent drying shrinkage. During the whole testing, the data (load and CMOD) was acquired and saved in the computer and the test was stopped when the CMOD reaches 3.5 mm.

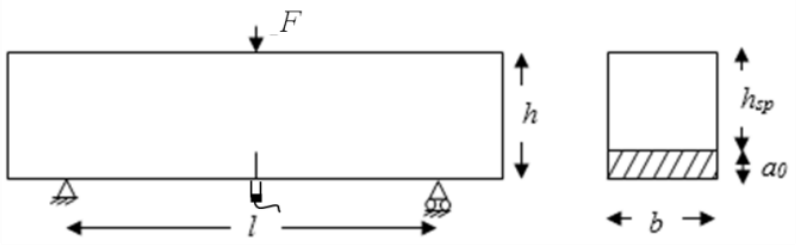

Figure 4.1. Testing configuration

4.4 TEST RESULTS

4.4.1 Flexural tests

Typical load-CMOD curves for the fibre reinforced concretes are shown in Figure 4.2, corresponding to one of the six batches made for each type of concrete. All the results in this programme are given in Appendix C. Note that the notation used for the different cases indicates the strength of the concrete, type of fibre incorporated, its dosage in kg/m^3 and the CMOD rate of the test in μm/s; e.g., M40SF30_0.1 denotes the 40 MPa grade concrete with steel fibres at 30 kg/m^3 dosage, tested at 0.1 μm/s. It can be seen that results for the PFRC show that the peak load and post-peak load-carrying capacity generally increase with an increase in loading rate. For SFRC, the peak load increases with the loading rate, though the difference is less significant at the higher fibre dosages. The post-peak load carrying capacity of SFRC for the dosage of 10 kg/m^3 does not show any clear trend but it increases with loading rate at higher fibre dosages, especially at smaller crack widths, with the intermediate dosage of 30 kg/m^3 giving the most significant trend. In all cases, the cracking, as observed visually on the surface, becomes less tortuous as the loading rate increases, as reported previously for plain concrete (Mechtcherine, 2009). Also, at the highest rate, multiple cracks were observed to initiate at the notch tip, of which one propagates further. The crack patterns reflect the increased energy demand of fracture propagation at faster loading rates caused by multiple crack initiation and straighter cracks that would require aggregate rupture and propagation along paths that are not necessarily those of least resistance. These mechanisms do not occur at slow crack propagation mainly due to the relaxation of the bridging stresses, as suggested previously (Bažant and Gettu, 1992; Bernad et al., 2002; Rosa et al., 2012).

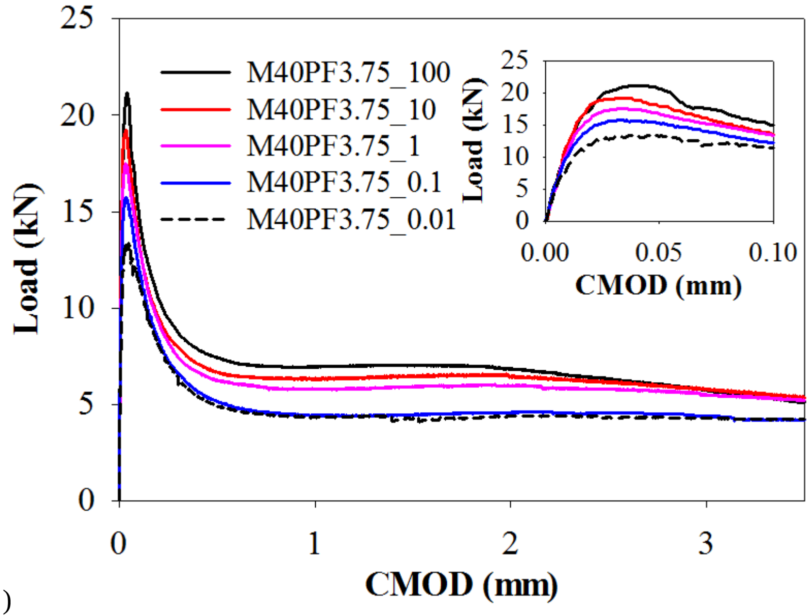

a)

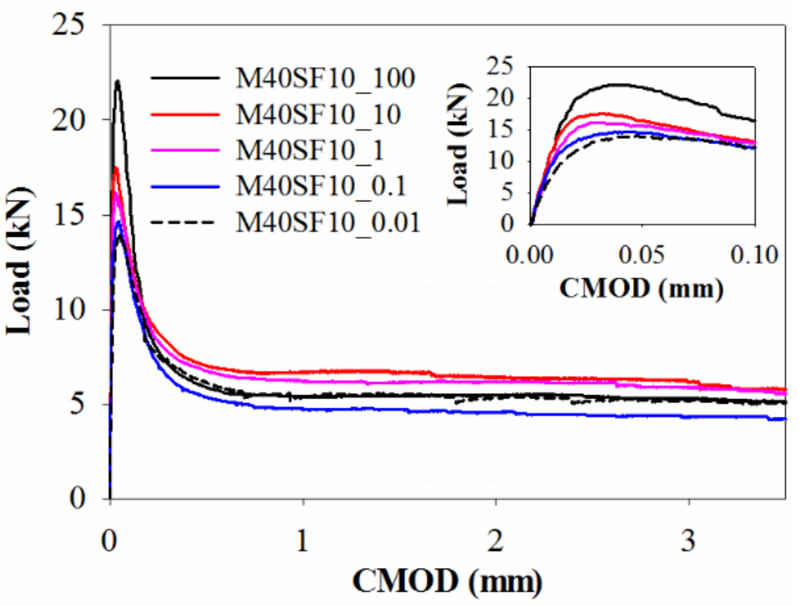
Load (kN)
CMOD (mm)
M40SF10_100
M40SF10_10
M40SF10_1
M40SF10_0.1
M40SF10_0.01
0
5
10
15
20
25
0
1
2
3
0.00
0.05
0.10

b)

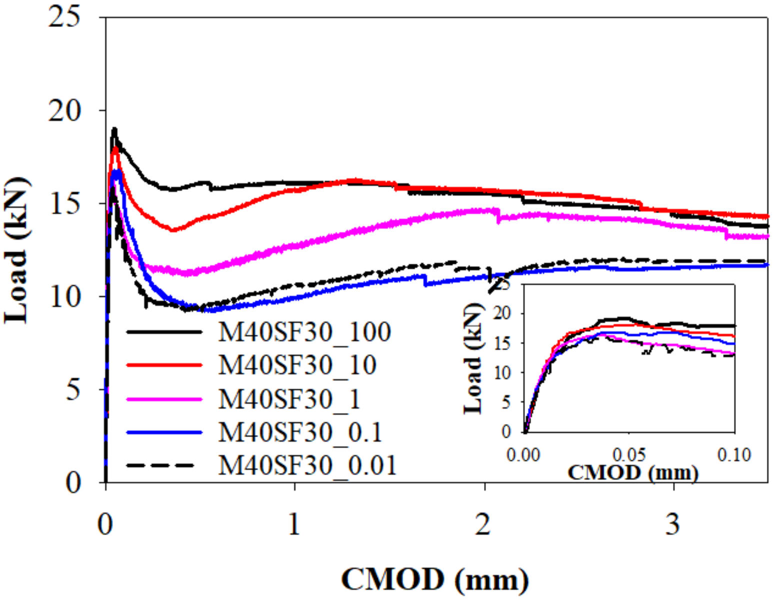
Load (kN)
CMOD (mm)
M40SF30_100
M40SF30_10
M40SF30_1
M40SF30_0.1
M40SF30_0.01
0
5
10
15
20
25
0
1
2
3
0.00
0.05
0.10

c)

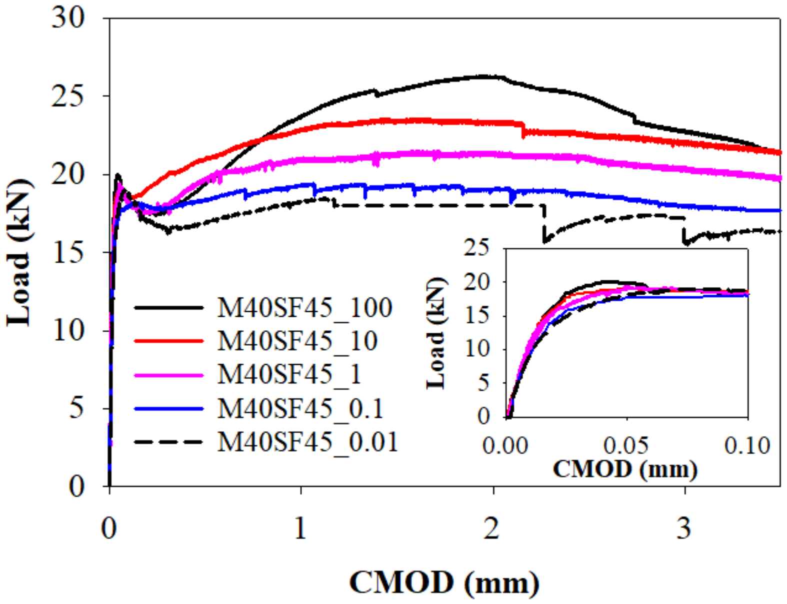

d)

Figure 4.2. Typical flexural response of concrete with a) 3.75 kg/m^3 PF, b) 10 kg/m^3 SF, c) 30 kg/m^3 SF, and d) 45 kg/m^3 SF at different loading rates

4.4.2 σ-w curves at different rates

An inverse analysis procedure developed previously (Stephen et al., 2019) based on the cracked hinge model of Olesen (Olesen, 2001) was used for obtaining the tensile constitutive relation (σ-w) corresponding to each experimentally-obtained load-CMOD curve. The inverse analysis yields σ-w relations that provide the best fit of the data, using the Probabilistic Global Search Lausanne (PGSL) algorithm for the minimzation of the error (Raphael and Smith, 2003). The parameters obtained correspond to the FPZ characteristics ahead of the stress-free crack tip, as shown in Figure 4.3 for the tetralinear model adopted here (Stephen et al., 2019), with the critical crack width, w_c, taken as one-fourth of the fibre length; note that for plain concrete, the shape of the curve is taken to be bilinear. When the stress developed in the concrete adjacent to the notch-tip reaches the tensile strength (f_t), the crack initiates. On further application of load, the crack propagates without significant contribution from the fibres until w_1. The peak load consequently depends on the stresses in the FPZ occuring between crack initiation (i.e., f_t) and the crack opening of w_1 (i.e., σ_1), which are dominated by the matrix response. The post-peak response is dominated by the σ-w curve beyond w_1, which is governed mainly by the matrix-fibre interaction.

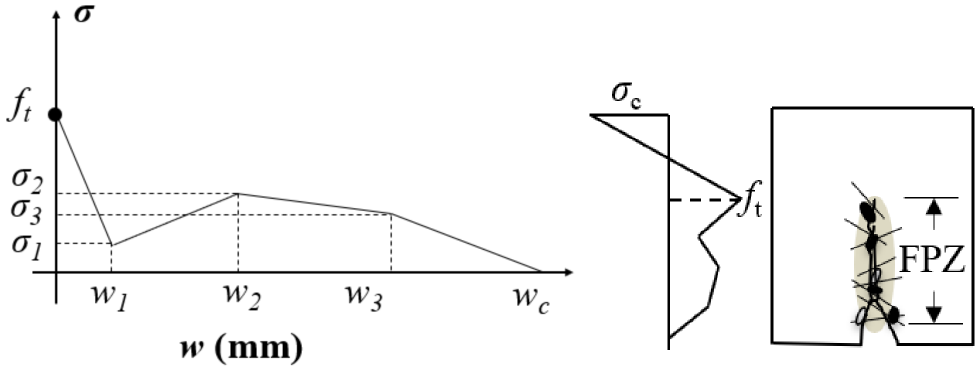

a) b)

Figure 4.3. a) Tetralinear tensile constitutive relation considered for FRC, and b) the corresponding stress distribution in the FPZ

From extensive runs of the inverse analysis scheme, it was seen that the crack openings (i.e., w_2 and w_3) at the kinks in the σ-w curve are similar at different loading rates for a particular FRC, implying that w_2 and w_3 are practically rate-independent, varying only with the fibre type and dosage. Therefore, fitting of the other parameters was done with the values of w_2 and w_3 obtained at the standard CMOD rate of 1 μm/s. The σ-w curves for different FRCs at different loading rates obtained from the inverse analyses of experimental data are shown in Figure 4.4 and the parameters of the σ-w curves (Figure 4.3) consequently obtained are presented in Table 4.2, in terms of the mean and standard deviation. In general, it is seen that the tensile strength (f_t) is higher and the initial drop in cohesive stresses is steeper (i.e., the diffference f_t - σ_1 is larger) at higher loading rates, more predominantly in concretes with lower toughness. Comparing the highest and lowest loading rates used here, the tensile strength is found to decrease approximately by 35% for plain concrete (similar to that observed previously Rosa et al. (2012); Santos and Sousa, 2015), 40% for M40PF3.75 and M40SF10, and 15% for M40SF30 and M40SF45, over 5 orders of magnitude of loading rate. It is evident, from Figure 4.4, that the rate-dependence of the tensile strength is less significant at higher dosages of steel fibres, which is in accordance with the data of Zhang et al. (2014). The higher tensile strength observed at faster loading rates can be attributed, as discussed earlier, to the lower tortuosity of the cracks and multiple cracking, which leads to a higher energy requirement. The reduction in tensile strength at slower loading rates is attributed to the relaxation of stresses near the crack tip; it is seen that the crack opening at the initiation of fibre bridging, w_1, is larger at slower loading rate, for all the concretes. In general, the rate-sensitivity of the bridging stresses in PFRC is much higher than SFRC, which is in accordance with the rate-sensitivity of the pull-out response observed by previous researchers (Babafemi and Boshoff, 2017; Nieuwoudt and Boshoff, 2017).

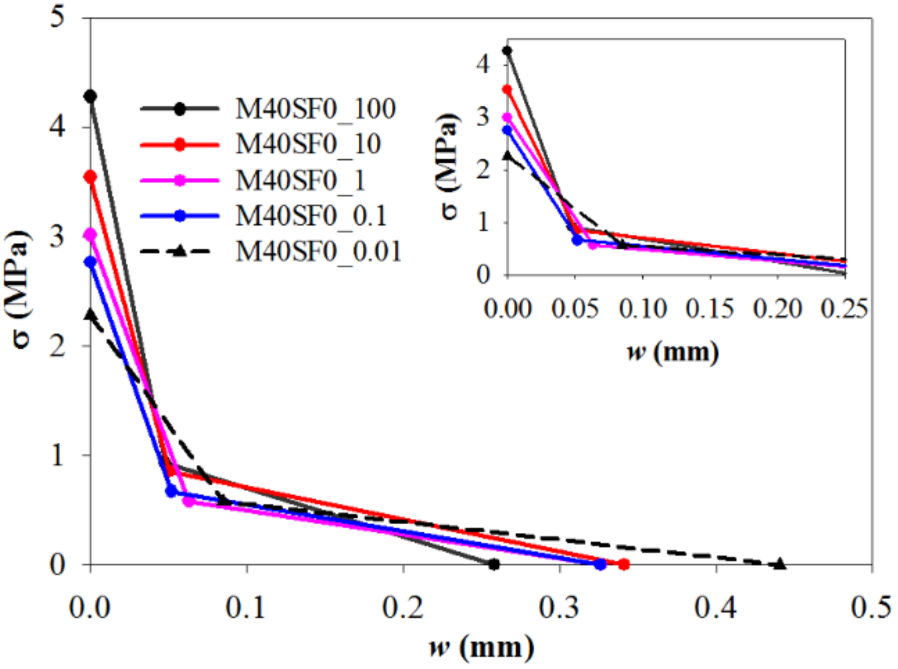

a)

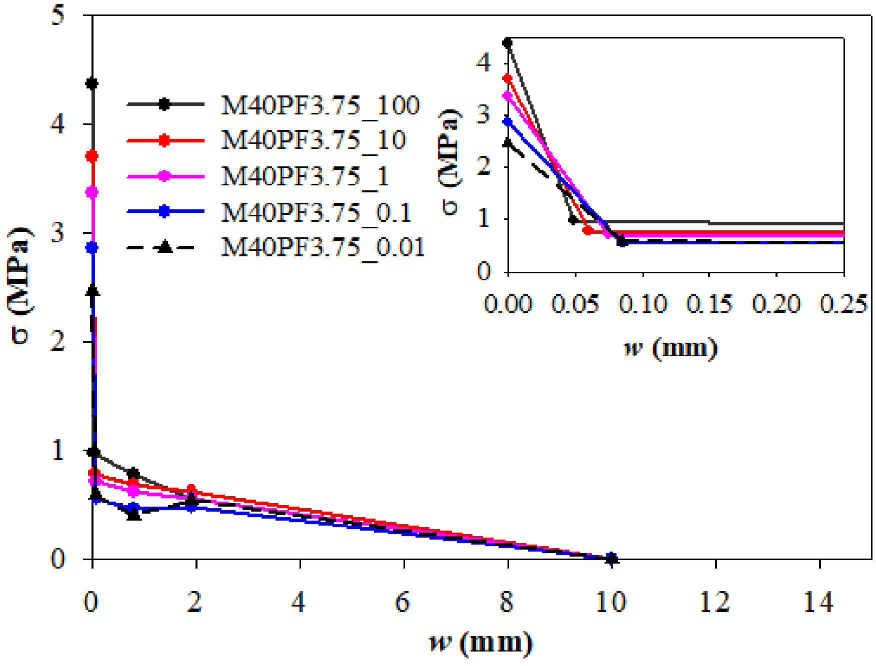

b)

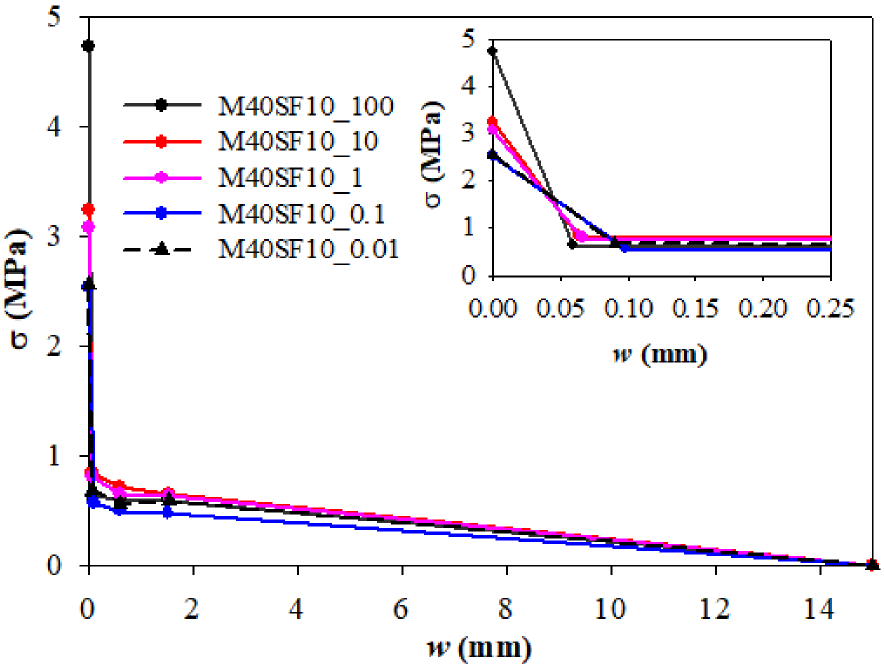
σ (MPa)
w (mm)
0
1
2
3
4
5
0
2
4
6
8
10
12
14
M40SF10_100
M40SF10_10
M40SF10_1
M40SF10_0.1
M40SF10_0.01
σ (MPa)
w (mm)
0.00
0.05
0.10
0.15
0.20
0.25

c)

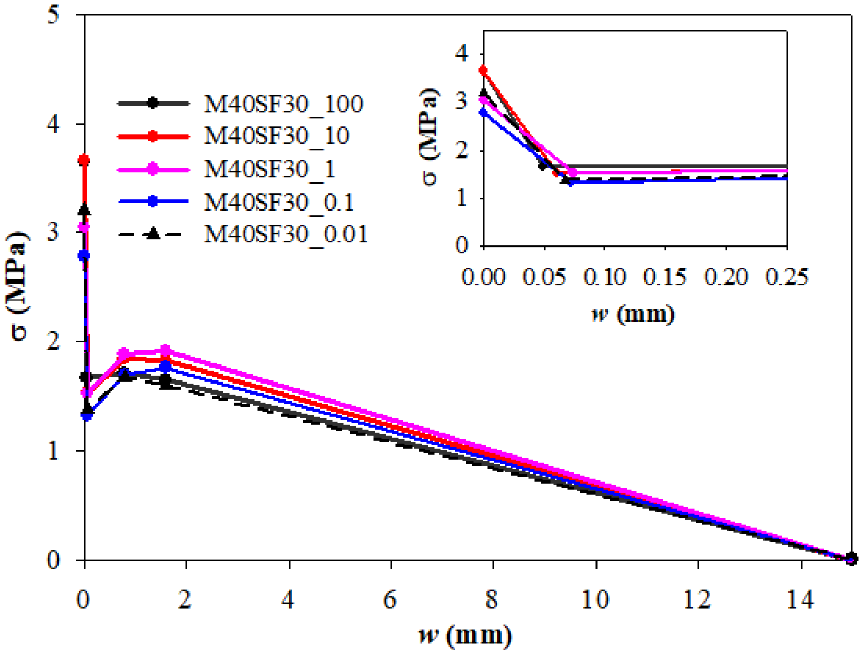
σ (MPa)
w (mm)
0
1
2
3
4
5
0
2
4
6
8
10
12
14
M40SF30_100
M40SF30_10
M40SF30_1
M40SF30_0.1
M40SF30_0.01
σ (MPa)
w (mm)
0.00
0.05
0.10
0.15
0.20
0.25

d)

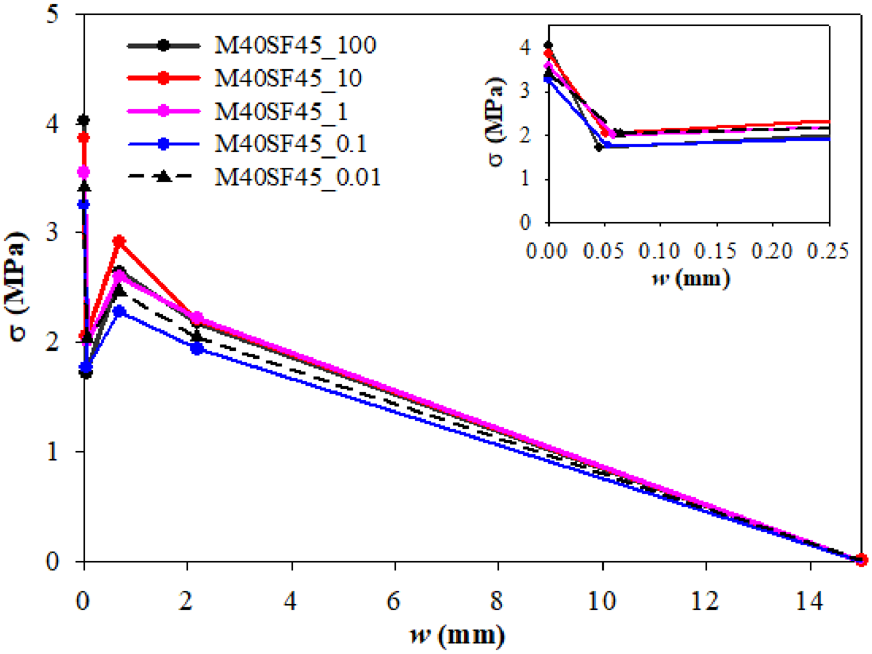

e)

Figure 4.4. Stress-crack opening curve concrete with a) 3.75 kg/m^3 PF, b) 10 kg/m^3 SF, c) 30 kg/m^3 SF, and d) 45 kg/m^3 SF at different loading rates

The consequence of the rate-dependence of the bridging stresses has been further investigated by modelling the development of the fracture process zone (FPZ) characterized by the parameters given in Table 4.2. In order to determine the FPZ characteristics, finite element modelling of a simply supported three-point notched beam having dimensions of 700×150×150 mm, with a span length of 500 mm and notch length of 25 mm, was performed using the discrete crack approach in the TNO DIANA v6 code (Figure 4.5). The size of the mesh is reduced near the interface elements, placed along the crack path (i.e., at mid-span). The stress-crack opening curve obtained by inverse analysis was used as the tensile constitutive relation of the interface and the uncracked region represented by a mesh of triangular and quadrilateral finite elements. The 3-point Newton-Cotes scheme is used for the integration in the interface elements.

Table 4.2. Parameters of σ-w curves obtained from inverse analyses (mean ± standard deviation)

Concrete	**CMOD rate (μm/s)**	f_t **(MPa)**	σ_1 **(MPa)**	w_1 **(mm)**	σ_2 **(MPa)**	w_2 **(mm)**	σ_3 **(MPa)**	w_3 **(mm)**	w_c **(mm)**
M40SF0	0.01	2.77±0.29	0.82±0.13	0.05±0.01	-	-	-	-	0.33±0.05
	0.1	2.83±0.18	0.84±0.15	0.04±0.01	-	-	-	-	0.28±0.08
	1	3.41±0.14	0.78±0.33	0.06±0.01	-	-	-	-	0.27±0.03
	10	3.93±0.80	1.03±0.52	0.05±0.03	-	-	-	-	0.31±0.08
	100	4.36±0.55	1.00±0.37	0.04±0.01	-	-	-	-	0.25±0.04
M40PF3.75	0.01	2.39±0.26	0.59±0.03	0.09±0.02	0.41±0.05	0.79	0.55±0.13	1.91	10
	0.1	2.86±0.38	0.58±0.13	0.09±0.02	0.47±0.12		0.48±0.09		
	1	3.18±0.34	0.67±0.18	0.09±0.01	0.65±0.12		0.55±0.18		
	10	3.70±0.20	0.79±0.16	0.06±0.01	0.68±0.02		0.62±0.16		
	100	4.20±0.53	0.81±0.14	0.07±0.02	0.78±0.09		0.59±0.05		
M40SF10	0.01	2.67±0.47	0.69±0.11	0.09±0.02	0.56±0.11	0.61	0.58±0.22	1.52	15
	0.1	2.54±0.33	0.55±0.08	0.10±0.02	0.50±0.09		0.48±0.14		
	1	3.08±0.24	0.81±0.12	0.07±0.02	0.66±0.10		0.64±0.11		
	10	3.24±0.21	0.85±0.27	0.06±0.01	0.72±0.23		0.66±0.14		
	100	4.58±0.32	0.64±0.11	0.06±0.01	0.64±0.10		0.60±0.12		
M40SF30	0.01	3.21±0.37	1.38±0.32	0.07±0.02	1.67±0.43	0.79	1.60±0.37	1.59	15
	0.1	2.78±0.26	1.33±0.32	0.07±0.02	1.60±0.33		1.69±0.25		
	1	3.05±0.63	1.52±0.39	0.07±0.03	1.89±0.48		1.91±0.62		
	10	3.66±0.41	1.53±0.25	0.06±0.01	1.84±0.46		1.82±0.45		
	100	3.65±0.15	1.66±0.25	0.05±0.01	1.71±0.40		1.65±0.33		
M40SF45	0.01	3.26±0.58	2.07±0.21	0.07±0.03	2.43±0.37	0.69	2.05±0.30	2.19	15
	0.1	3.26±0.41	1.77±0.40	0.05±0.01	2.28±0.39		1.94±0.20		
	1	3.55±0.39	2.00±0.34	0.06±0.02	2.51±0.35		2.22±0.22		
	10	3.93±0.12	2.26±0.44	0.05±0.01	3.19±0.29		2.33±0.18		
	100	4.03±0.17	1.72±0.29	0.05±0.01	2.64±0.59		2.18±0.31		

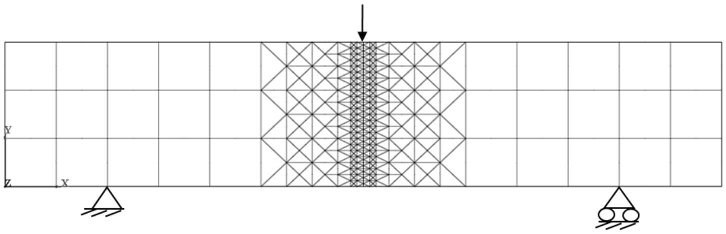

Figure 4.5. Finite element mesh used

Non-linear analysis is performed for each loading rate and the interfacial stresses along the ligament depth at various stages of crack propagation is determined. The stress profile at the first-peak load and at a CMOD of 0.5 mm are shown in Figure 4.6, for the different concretes studied. It can be seen that at peak load, the stresses developed are larger at higher loading rates, implying higher energy dissipation. In the case of plain concrete at the slowest loading rate, there is some bridging action at the notch tip, whereas at other loading rates, a traction-free crack (indicated by zero bridging stress) occurs ahead of the notch tip. This could explain the reduction in brittleness of the concrete at slower loading rate. In case of fibre reinforced concrete (FRC), the FPZ at a CMOD of about 0.5 mm is found to be virtually the same for all loading rates. At this CMOD, the crack has progressed until the edge of the specimen and FPZ seems to be unaffected by the loading rate.

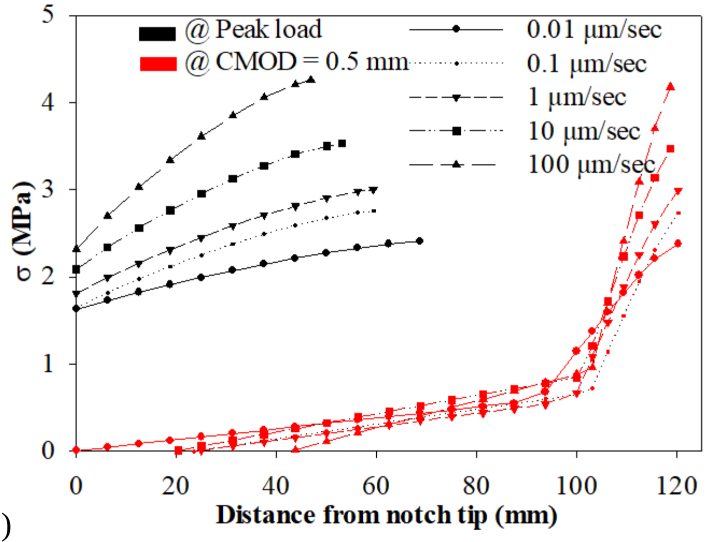

a)

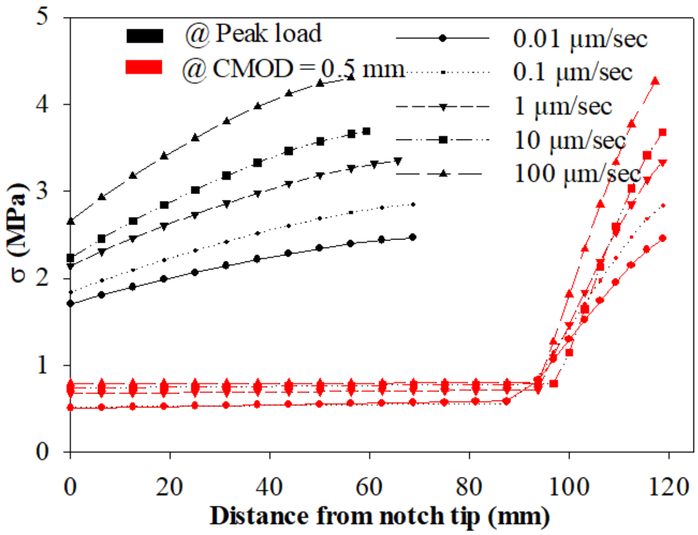
@ Peak load
@ CMOD = 0.5 mm
0.01 µm/sec
0.1 µm/sec
1 µm/sec
10 µm/sec
100 µm/sec
σ (MPa)
0
1
2
3
4
5
0
20
40
60
80
100
120
Distance from notch tip (mm)

b)

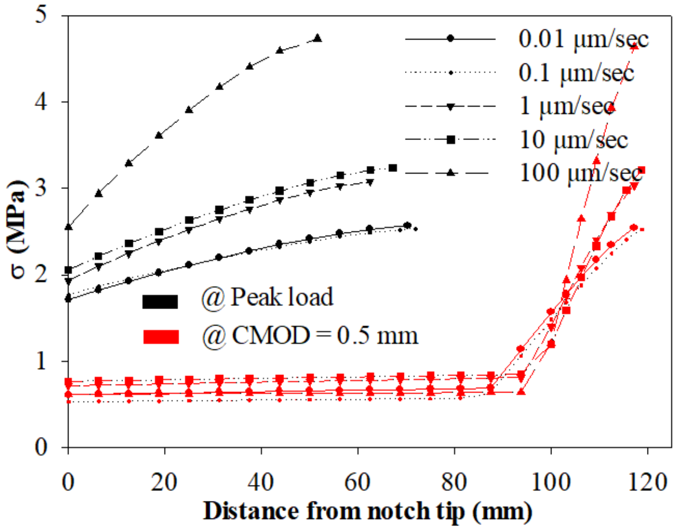
0.01 µm/sec
0.1 µm/sec
1 µm/sec
10 µm/sec
100 µm/sec
@ Peak load
@ CMOD = 0.5 mm
σ (MPa)
0
1
2
3
4
5
0
20
40
60
80
100
120
Distance from notch tip (mm)

c)

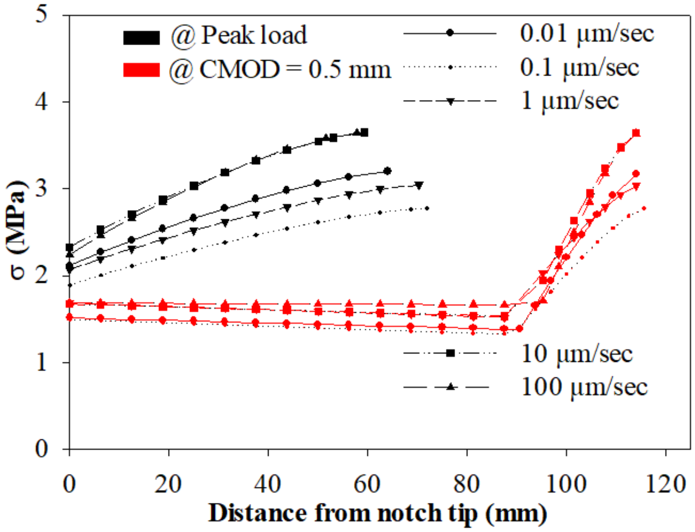
@ Peak load
@ CMOD = 0.5 mm
0.01 µm/sec
0.1 µm/sec
1 µm/sec
10 µm/sec
100 µm/sec
σ (MPa)
0
1
2
3
4
5
0
20
40
60
80
100
120
Distance from notch tip (mm)

d)

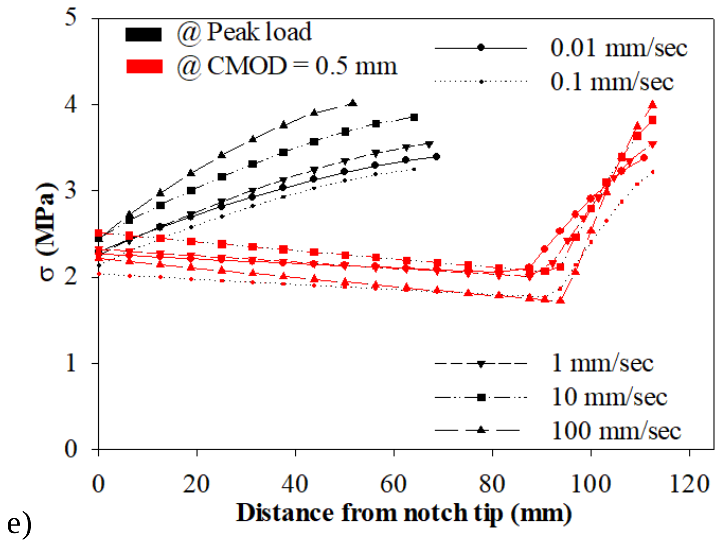

Figure 4.6. Bridging stress variation in the FPZ of concrete with a) 3.75 kg/m³ PF, b) 10 kg/m³ SF, c) 30 kg/m³ SF, and d) 45 kg/m³ SF at different loading rates

It is seen from the analyses that the length of FPZ at peak load increases significantly with an increase in the time to peak (Figure 4.7a), which is in accordance with the conclusions of Rosa et al. (2012). When the CMOD reaches 0.5 mm (Figure 4.7b), the FPZ covers the ligament length, in all cases, and the crack is fully developed. Therefore, the peak load generally decreases with the loading rate due to the governing role of matrix cracking whereas the response at larger CMOD only depends on the fibre-matrix interaction (i.e., fibre type and dosage, and pull-out response) and consequently, on its time-dependence.

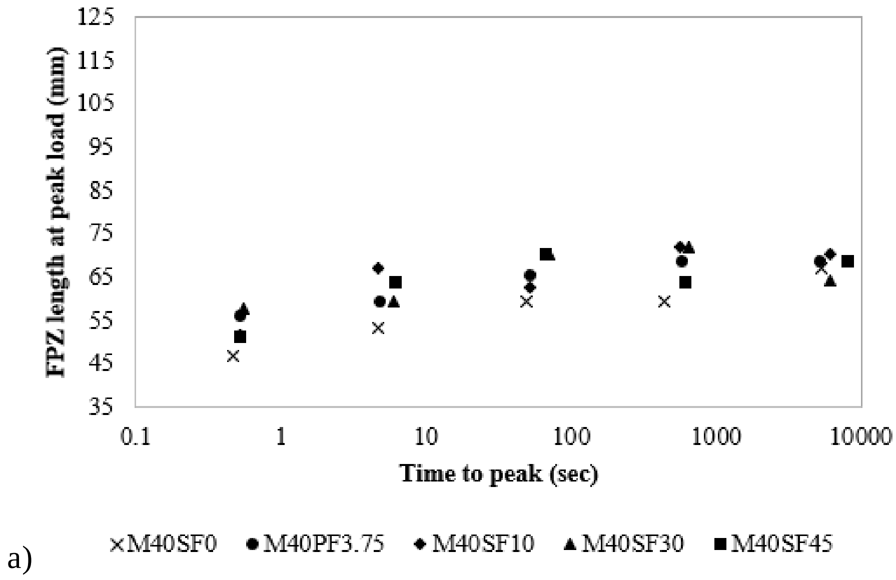

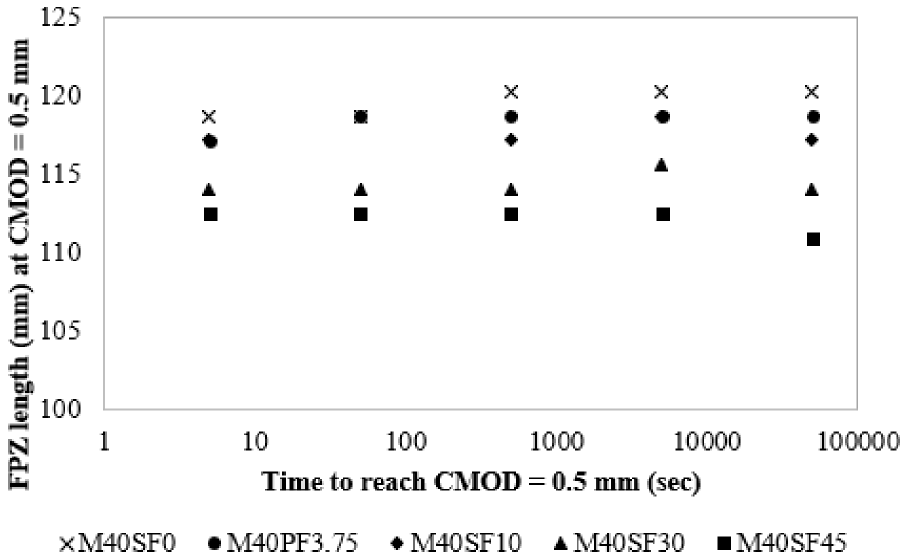

b)

Figure 4.7.Variation of fracture process zone length at a) peak load and b) CMOD = 0.5 mm, with respect to time

4.5 DISCUSSION OF THE TRENDS

For modelling the trends in the σ-w curves as a function of the crack opening rate, with the possibility of using them in numerical analysis, the CMOD was related to the crack-tip opening displacement (CTOD), using rigid body mechanics, as:

$$\mathrm{CMOD} = 1.2\mathrm{CTOD} \tag{4.1}$$

The different parameters of the σ-w curves are discussed hereafter with respect to the CTOD rate. It is seen in Figure 4.8 that the rate-dependence of the tensile strength of plain, polymer and lower dosage steel fibre in concretes is similar and much pronounced than that of the other concretes. It also confirms that the incorporation of higher dosages of fibres moderates the crack rate-dependence of FRC. The trends obtained can be modelled as:

$$f_{t,x} = f_{t,std} + m\, log_{10}(\dot{\mathrm{CTOD}}_x) \tag{4.2}$$

where, $f_{t,x}$ = tensile strength of concrete at the CTOD rate of $\dot{\mathrm{CTOD}}_x$ and $f_{t,std}$ = tensile strength of concrete at the standard loading rate. For the present data, linear regression yields m = 0.46 MPa.s/µm for M40SF0, M40PF3.75 and M40SF10, and m = 0.18 MPa.s/µm for M40SF30 and M40SF45.

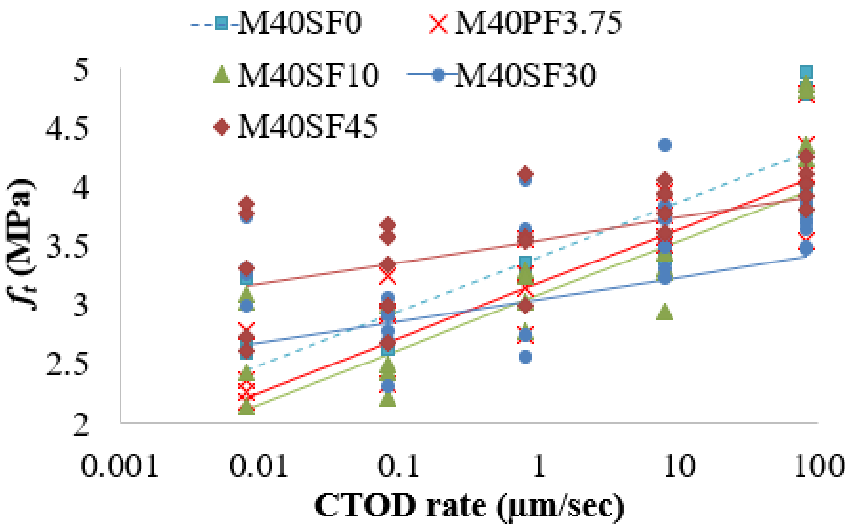

Figure 4.8. Variation of tensile strength with the loading rate

The plots of the variation in the change in bridging stresses with cracking rate, in Figure 4.9, show that the rate-dependence seems to be independent of the fibre type and dosage. Consequently, the rate-dependence of the bridging stress could be decoupled as the rate-dependencies of the tensile strength of the matrix (i.e., plain concrete) and the fibre bridging, as:

$$(\sigma_{i,x} - \sigma_{i,std}) = (f_{t,conc,x} - f_{t,conc,std}) + c\, log_{10}(\dot{\mathrm{CTOD}}_x), \text{ where } i = 1,2,3 \qquad (4.3)$$

where c is a constant considered to be independent of the fibre type and dosage, and $f_{t,conc,_x}$ and $\sigma_{i,_x}$ are the tensile strength of the plain concrete and the bridging stress at the CTOD rate of $\dot{\mathrm{CTOD}}_x$, respectively. For Eqn. (4.3), linear regression analysis yields the value c = -0.39 MPa.s/µm.

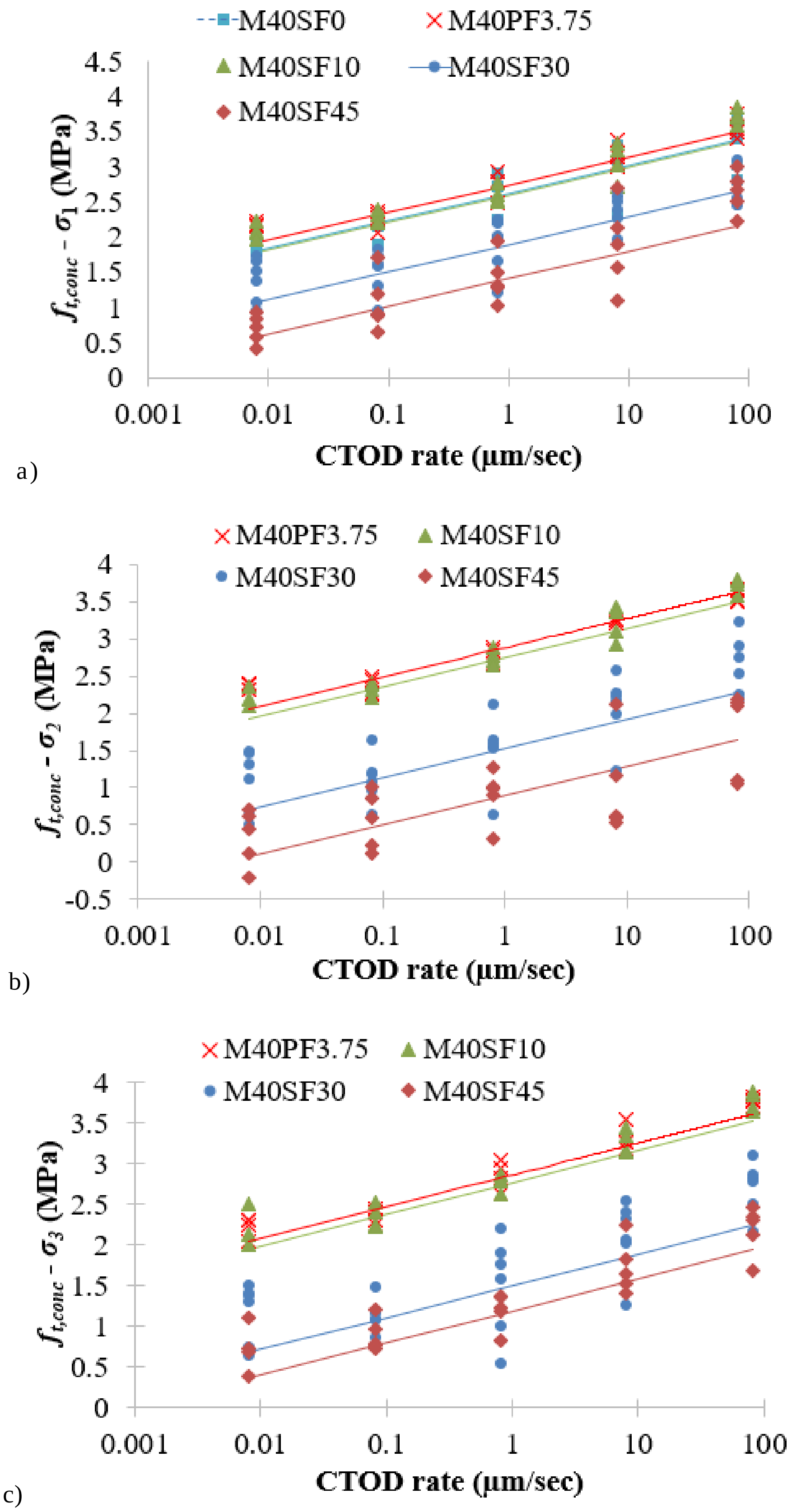

Figure 4.9. Variation of a) σ_1, b) σ_2 and c) σ_3 with CTOD rate for different concretes

The proposed Eqns. (4.2) and (4.3) consequently comprise the model for rate-dependence of the fracture of FRC that can be used in analysis and design.

4.6 EFFECT OF LOADING ON THE TOUGHNESS PARAMETERS

In the design of FRC structures, such as tunnel segments, pavements and slabs-on-grade, the residual flexural strength of the material is utilised as the input parameter (Nayar, 2015; ACI 544.7R, 2016). The limit of proportionality (LOP) or flexural strength and the residual strengths ($f_{R,j}$) at various CMOD values, as defined by EN 14651 (2005), along with the Young's modulus obtained from the initial slope of the load-CMOD curve (as explained in Chapter 3 Section 3.3.2), are given in Table 4.3 for the different concretes and loading rates. The first peak flexural strength or limit of proportionality (LOP) is given be the expression:

$$f_L = \frac{3F_L l}{2bh_{sp}^2} \tag{4.1}$$

where F_L is the load corresponding to the first peak load, l is the length of the span, b is the width of the specimen, h_{sp} is the distance between the tip of the notch and the top of the specimen. The residual flexural strength at different CMODs is calculated using the following equation:

$$f_{R,j} = \frac{3F_j l}{2bh_{sp}^2} \tag{4.2}$$

where F_j is the load corresponding with $CMOD = CMOD_j$ Even though there is no significant trend in the Young's moduli with loading rate, all the concretes exhibit the least values at the slowest rate.

Table 4.3. Toughness parameters at different loading rates (mean ± standard deviation)

Concrete	**CMOD rate (µm/s)**	**E (GPa)**	**LOP* (MPa)**	**Residual flexural strength at different CMODs**			
				0.5 mm $f_{R,1}$ (MPa)	**1.5 mm $f_{R,2}$ (MPa)**	**2.5 mm $f_{R,3}$ (MPa)**	**3.5 mm $f_{R,4}$ (MPa)**
M40SF0	0.01	34.54±2.41	4.85±0.24	0.99±0.31	-	-	-
	0.1	41.26±3.61	5.05±0.22	0.82±0.26	-	-	-
	1	37.50±2.10	5.61±0.10	0.69±0.21	-	-	-
	10	41.18±1.89	6.06±0.37	0.92±0.24	-	-	-
	100	36.76±2.31	6.24±0.41	0.74±0.22	-	-	-
M40PF3.75	0.01	31.95±3.66	4.51±0.23	1.57±0.17	1.36±0.07	1.38±0.05	1.35±0.06
	0.1	33.68±1.85	5.13±0.52	1.65±0.37	1.42±0.34	1.45±0.3	1.34±0.25
	1	39.97±3.71	5.47±0.30	1.99±0.41	1.89±0.35	1.85±0.35	1.67±0.39
	10	39.64±5.89	6.31±0.24	2.27±0.16	2.14±0.09	2.09±0.12	1.88±0.08
	100	37.06±6.92	6.82±0.29	2.60±0.25	2.35±0.18	2.15±0.13	1.73±0.10
M40SF10	0.01	29.21±11.3	4.48±0.13	1.85±0.25	1.59±0.42	1.50±0.54	1.39±0.49
	0.1	33.88±4.43	4.76±0.62	1.75±0.17	1.59±0.32	1.55±0.28	1.46±0.21
	1	33.84±5.18	5.15±0.40	2.05±0.27	1.89±0.31	1.90±0.26	1.76±0.36
	10	43.05±1.97	5.58±0.31	1.99±0.47	1.85±0.44	1.85±0.42	1.72±0.41
	100	34.80±3.83	7.24±0.23	1.95±0.16	1.88±0.24	1.86±0.20	1.76±0.27
M40SF30	0.01	22.17±3.74	5.11±0.54	3.42±0.47	3.90±0.41	3.96±0.30	3.77±0.26
	0.1	37.38±2.64	5.23±0.31	3.69±0.52	4.49±0.62	4.72±0.64	4.65±0.56
	1	40.24±4.50	5.52±0.47	4.09±0.59	4.86±0.83	5.04±0.91	4.92±0.94
	10	37.97±3.02	6.11±0.35	4.17±0.37	4.69±0.46	4.75±0.52	4.56±0.56
	100	33.72±4.77	6.25±0.26	4.87±0.52	5.12±0.75	5.05±0.78	4.85±0.84
M40SF45	0.01	28.16±0.77	5.84±0.40	5.77±0.60	6.62±0.99	6.43±0.85	6.15±0.79
	0.1	30.91±2.95	6.01±0.27	5.87±0.04	6.74±0.52	6.51±0.46	6.06±0.36
	1	37.45±2.20	6.21±0.47	6.11±0.33	6.85±0.08	6.82±0.29	6.41±0.33
	10	37.67±2.73	6.31±0.45	5.97±1.36	7.34±1.69	7.09±1.46	6.57±1.21
	100	34.42±1.20	6.41±0.30	5.51±0.95	6.92±1.36	6.94±1.22	6.33±1.02

*Note that the LOP is based on the first peak load, in each case.

The flexural strength and toughness parameters in Table 4.3 are represented diagrammatically to visualize the trend in Figures 4.10 and 4.11. The flexural strength is found to generally decrease with a decrease in crack rate, varying from the fastest to slowest rate by about 20% for the plain concrete, and 35% for the PFRC and M40SF10 concrete. For higher dosages of steel fibres, the variation over the crack rate range is only about 15%, which is in accordance with the moderation of rate-dependence discussed earlier.

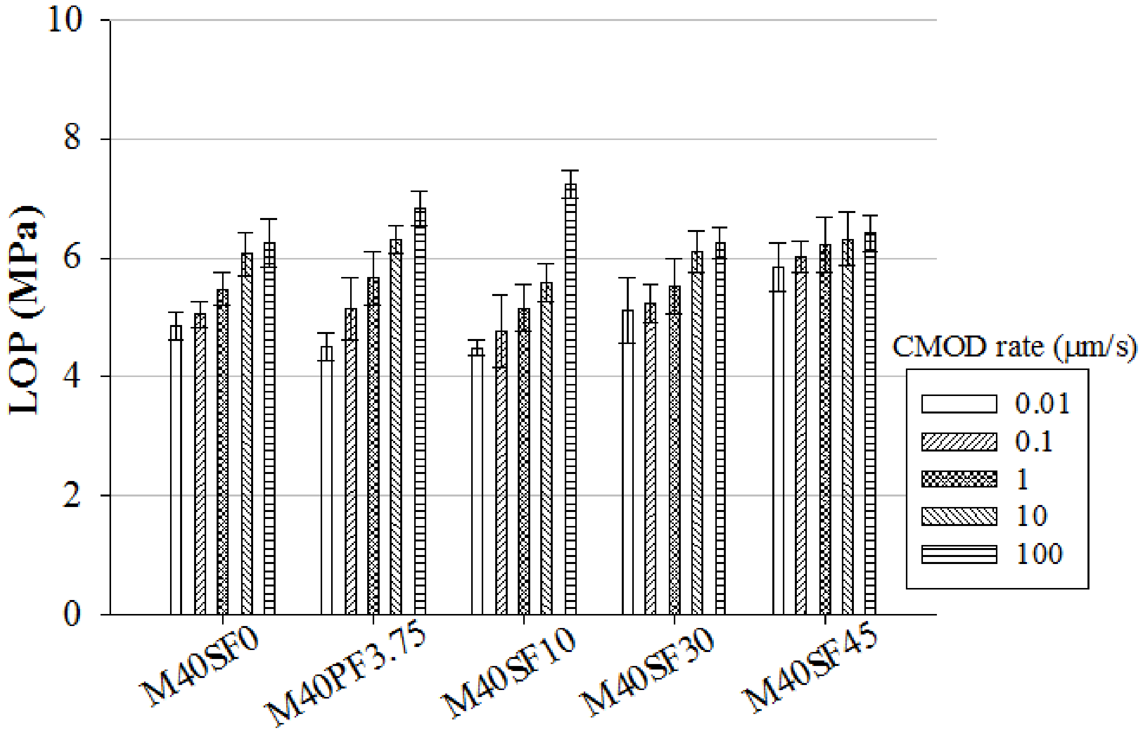

Figure 4.10. Effect of loading rate on LOP for different types of concrete

The residual flexural strengths reduce by about 40% for PFRC and 20% for M40SF10 and M40SF30, over the loading rates studied here. The FRC with the highest dosage of SF (i.e., M40SF45) showed the least rate-dependence (i.e., about 10% decrease in residual strength from fastest to slowest loading rate). It is evident that the flexural strength and toughness are rate-dependent, especially for low toughness concrete, and this would need to be accounted for in the design of FRC structures where appropriate.

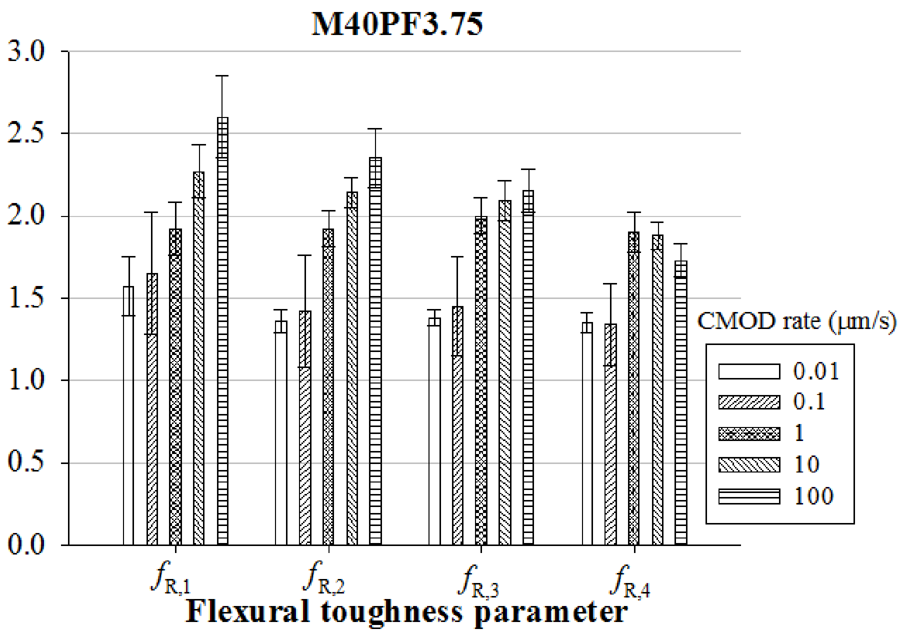
M40PF3.75
3.0
2.5
2.0
1.5
1.0
0.5
0.0
$f_{R,1}$
$f_{R,2}$
$f_{R,3}$
$f_{R,4}$
Flexural toughness parameter
CMOD rate (μm/s)
0.01
0.1
1
10
100

a)

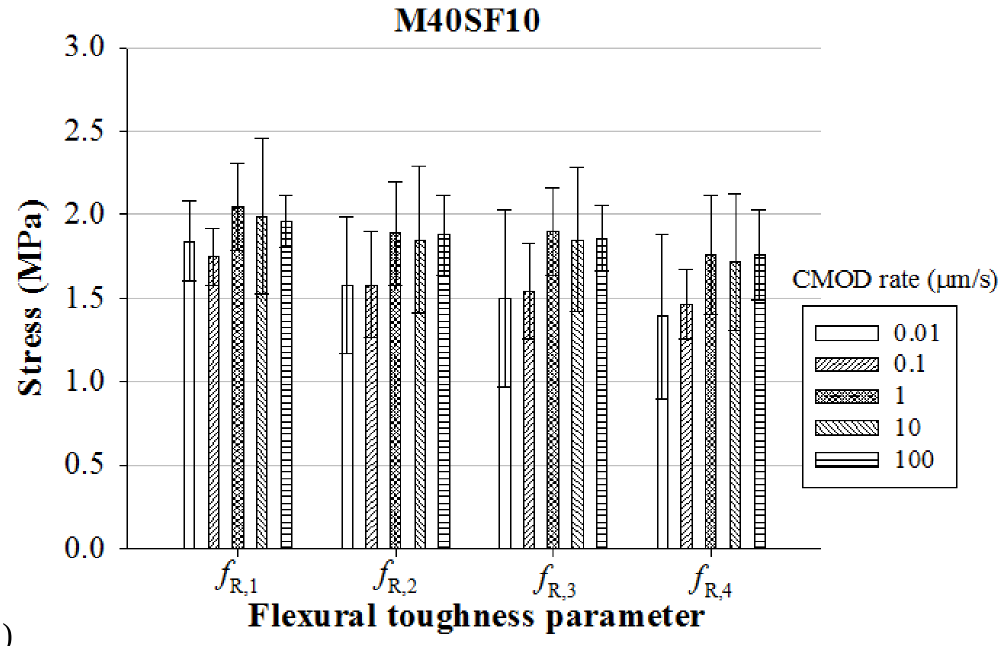
M40SF10
Stress (MPa)
3.0
2.5
2.0
1.5
1.0
0.5
0.0
$f_{R,1}$
$f_{R,2}$
$f_{R,3}$
$f_{R,4}$
Flexural toughness parameter
CMOD rate (μm/s)
0.01
0.1
1
10
100

b)

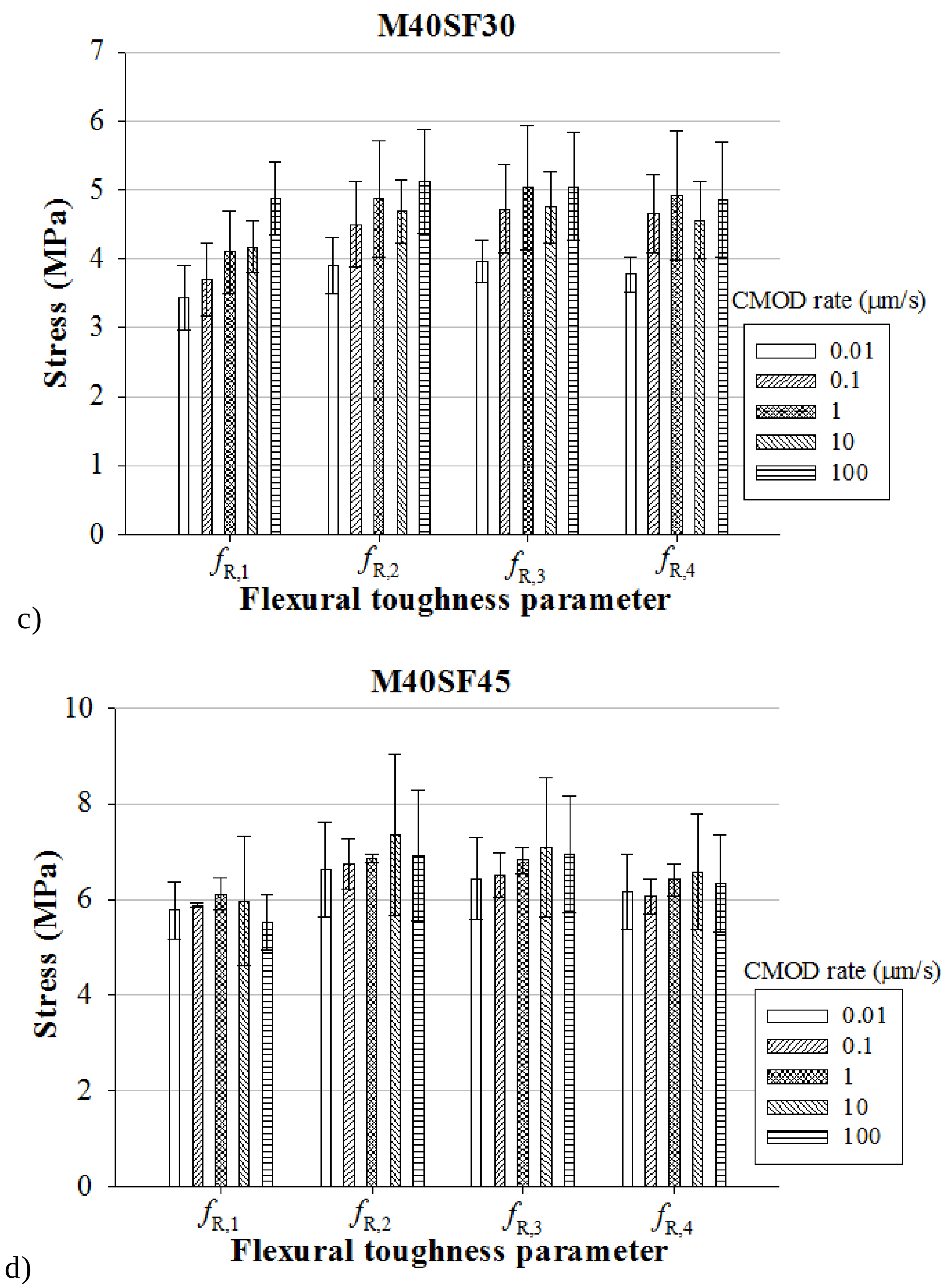

Figure 4.11. Effect of loading rate on flexural toughness parameter for concrete with a) 3.75 kg/m^3 PF, b) 10 kg/m^3 SF, c) 30 kg/m^3 SF, and d) 45 kg/m^3 SF

4.7 CONCLUSIONS

Three-point bending tests have been performed on fibre reinforced concrete (FRC) with steel and polymer fibres, at different loading rates (over 5 orders of magnitude), and the data has been used to determine the tensile stress-crack opening (σ-w) curves by inverse analyses. It is seen that the rate-dependence is stronger for FRCs with polypropylene fibres than with higher dosages of steel fibres. It is evident that the rate-dependence should be incorporated where appropriate in the design of FRC structures. For this purpose, an empirical model has been proposed to represent the variations in the tensile constititutive relation of FRC with the crack opening rate.

The results of the study further lead to the following specific conclusions:

- The tensile and flexural strength of concrete reduce by 40% for low toughness concrete, when comparing the slowest and fastest loading rates over 5 orders of magnitude. The lowering of the tensile strength can be attributed to the relaxation of stresses near the crack tip, which leads to an increase in the FPZ length, as seen in the finite element simulations. The reduction in strength is found to be much lower in concretes with higher dosages of steel fibres.

- The residual flexural strength (or toughness) of polymer fibre reinforced concrete (PFRC) is found to exhibit higher rate-dependence (i.e., 40% reduction from the fastest to slowest loading rate) compared to steel fibre reinforced concrete (i.e., 20% decrease). This could be a consequence of fibre creep and weakening of the fibre-matrix interface in PFRC at slower crack rates. FRC with the highest dosage of steel fibres, showed the least rate-dependence with only about 10% lower residual strength from fastest to slowest loading rate. Higher dosages of steel fibres in concrete seem to be beneficial for structures subjected to different loading rates.

- The analytical results from the inverse analysis of flexural test data allowed to obtain the rate-dependent model for predicting the tensile strength and cohesive stresses developed during crack propagation at different loading rates.

- The σ-w curve for different loading rates seem to be modelled well using the proposed model based on the σ-w curve at the standard rate for the corresponding FRC and the rate-dependence of the tensile strength. The resulting σ-w curve can be conveniently used in the numerical analysis to predict the structural response at different loading rates.

5 POST-PEAK FATIGUE BEHAVIOUR OF CRACKED FRC IN FLEXURE

5.1 INTRODUCTION

In the previous chapter, the behaviour of fibre reinforced concrete (FRC) structures under different quasi-static loading rates was discussed. Many FRC structures, such as pavements, industrial slabs, bridge deck slabs, and tunnel lining segments, are also subjected to cyclic loads, in the form of traffic movement, wind and wave action, thermal variation and machine vibration. These structures experience upto millions of stress cycles during their service life, which could have detrimental effects on material properties, such as strength, stiffness, toughness, and durability. Since the inelastic design of these structures includes the residual flexural strength of the material as an input parameter, whose degradation during fatigue loading is unknown, there is the need for the study of fatigue performance in the post-peak regime. Fatigue loading could also pose problems in terms of aggravating crack widths and deflections, and it could affect the Serviceability Limit State (SLS), even if fatigue failure does not occur. Though there have been many studies on the fatigue of plain and fibre reinforced concrete in the uncracked (pre-peak) state, the post-peak fatigue response of cracked elements has not been extensively explored.

In this context, with the primary objective to determine the fatigue performance in the post-peak regime, concrete beams reinforced with different dosages of steel fibres are assessed by subjecting them to fatigue loading after inducing a small crack. From the fatigue tests, the S-N model or Wöhler diagram, a plot between applied stress expressed as a fraction of the static strength (S) and the number of cycles to failure (N_f), is derived for each type of concrete. In order to understand the fatigue damage mechanisms in the post-peak region, the level of damage is evaluated by examining the increase in crack opening with the cycles. The role of fibres in mitigating the crack growth is examined by calculating the stiffness, as the slope of the load-crack mouth opening displacement curve for a cycle. The S-N model based on number of cycles to reach the critical crack opening, which is the crack opening at which the fatigue crack growth becomes unstable, is derived from the test results. The significance of this model is also discussed in terms of safety of the structure subjected to fatigue.

5.2 FATIGUE FRACTURE OF FRC IN FLEXURE

Fatigue is a process of progressive detrimental changes occurring in a structure, or structural member, subjected to repeated loading. The fatigue damage of concrete is generally divided into three stages (Batson et al., 1972). The first stage is flaw initiation, which depends on the quality of concrete in terms of porosity and matrix-aggregate interface properties. The second stage is slow progression of crack to a critical size. In the third stage, the crack propagates rapidly, and when the unstable cracks coalesce to form a continuous crack, failure occurs.

Various studies have been performed on plain and fibre reinforced concrete to obtain fatigue response, which mostly consist of assessing the fatigue strength, endurance limit and level of damage. Fatigue strength is defined as the repetitive stress as a fraction of static strength that can be sustained for a given number of cycles and endurance limit is referred as the maximum stress at which 2 million cycles of fatigue load can be sustained without failure (Li and Matsumoto, 1998). Due to lack of standards, there have been numerous variables such as loading frequency, stress ratio (ratio between upper and lower fatigue stress limits), testing configuration, and type of concrete (Wei et al., 1996), which cause variations in the test results (listed in Table 5.1) within the literature.

Typically, fatigue testing is conducted in a load-controlled mode with specified lower and upper fatigue stress limits under constant amplitude non-reversed sinusoidal loads, with frequency varying between 2 and 20 Hz. The speed of testing (loading frequency) between 1 to 7 Hz, in general, appears to be insignificant, although very low frequencies of application of load are generally associated with somewhat lower fatigue strengths and greater permanent deformation (Murdock, 1965; Lloyd et al., 2007).

In the case of stress ratio, the fatigue life is highly sensitive to the upper fatigue stress limit and to some extent the lower fatigue stress limit (Zhang et al., 1999). Usually, the lower fatigue stress limit is maintained constant, and the upper fatigue limit is varied until the endurance limit is reached (Johnston and Zemp, 1992). The relation between stress ratio and fatigue life (stress-number of cycles to failure; *S*-*N*) is found to be inversely proportional. Higher fatigue stress is associated with faster degradation of mechanical properties, as a result of the progressive increase in deformation, and thus approaching the critical size faster. It is believed that high fatigue loads are associated with matrix cracking and low fatigue loads are related to bond cracking (Grzybowski and Meyer, 1993).

In terms of the testing configuration, most fatigue testing has been performed on unnotched beams (refer Table 5.1). However, with the need of assessing the level of damage, due to fatigue loading, in terms of crack opening and stiffness degradation, researchers have had interest on notched beam testing (Gopalaratnam and Cherian, 2002). The fatigue models developed using notched beam data (Chang and Chai, 1995; Banjara and Ramanjaneyulu, 2018)is found to be more conservative than that of the model developed using unnotched beam (Johnston and Zemp, 1992; Cachim, 1999). However, since the fracture surface of the fatigue crack is defined, the scatter in the result is lower in notched beam data.

Fibre addition is more useful in resisting larger fatigue stresses than lower fatigue stresses, as the fibre bridging and pull-out play a dominant role in inhibiting the crack growth in the concrete matrix during fatigue loading (Spadea and Bencardino, 1997). Larger the fibre content and fibre aspect ratio, higher is the stiffness of FRC and thus higher is the fatigue life (Johnston and Zemp, 1992; Chang and Chai, 1995). The fatigue performance of concrete reinforced with steel fibres is superior to that reinforced with polymer or glass fibres. This is because of the high stiffness modulus of the fibre, which helps in improving the pull-out strength under fatigue. Hooked ended steel fibres are found to have higher endurance limit compared to straight or corrugated fibres because of the enhanced anchorage mechanism (Ramakrishnan et al., 1989; Zhang et al., 1999).

Extensive research has been carried out, and several researchers (Lee and Barr, 2004) have developed fatigue models in which unnotched (Cachim, 1999) or notched beams (Banjara and Ramanjaneyulu, 2018) are tested in the pre-peak region to determine the response of FRC (IRC:58, 2010; IRC:SP:46, 2013). The different models based on pre-peak fatigue performance available in the literature are compared in Figure 5.1 along with the model suggested in the IRC Standard for FRC (IRC:58, 2010; IRC:SP:46, 2013), which is also based on pre-peak fatigue performance,. It is seen that the model suggested

Table 5.1 Review of literature related to the flexural fatigue response of FRC

Investigators	**Region of fatigue loading**		**Specimen details**		**Stress ratio**	**Frequency**	**Fibre details**		**Main conclusions**
	Pre-peak	**Post-peak**	**Unnotched**	**Notched**			**Type**	**Volume fraction**	
Batson et al. (1972)	●		●		60% to 70% of F_{cr}	3 Hz	SF	2 and 3%	• EL increases with fibre dosage
Ramakrishnan et al. (1989)	●		●		55% to 80% of F_L	20 Hz	SF, PF	0.5 and 1%	• EL for SFRC is higher than PFRC • Hooked ended SF provides higher fatigue life than straight SF
Johnston and Zemp (1991)	●		●		75% to 98% of F_L	15 Hz	SF	0.5 to 1.5%	• Steel fibre content higher than 1% are found to give better fatigue life. • Higher the aspect ratio, higher is the resistance to fatigue loads.
Wei et al. (1996)	●		●		60% to 95% of F_L	5 Hz	SF	1 to 1.5%	• Increase in matrix-aggregate and fiber-matrix interfacial strength improves the fatigue performance
Cachim (1999)	●		●		70% to 100 of F_{cr}	2 Hz, 5 Hz	SF	0.5%	• No increase in fatigue performance observed with incorporation of steel fibres. • No significant variation in fatigue performance is found for specimens loaded at different loading frequency.
Goel and Singh (2014)	●		●		65% to 90% of F_L	10 Hz	SF	0.5%, 1% and 1.5%	• Fatigue failure is observed with fibre pull out, indicating that fibre bridging is affected by the fatigue loading.
Chang and Chai (1995)	●			●	70% to 85% of F_{cr}.	10 Hz	SF	0.5 to 1.5%	• Higher the fibre content and aspect ratio, higher is the stiffness of SFRC and the fatigue performance

Zhang et al. (1999)	●			●	70% to 90% of F_L	4.5 Hz	SF	1%	- Higher the minimum load longer is the fatigue life, because of decreased bridging degradation
Granju et al. (2000)		●		●	50% to 80% of F_R	5 Hz	SF	0.8%	- Post-peak fatigue strength is 50% of the residual strength
Gopalaratnam and Cherian (2002)	●			●	60% to 90% of F_L	20 Hz	SF, PF	0.5%	- The fatigue performance of SFRC is better than PFRC - The fatigue strength for SFRC samples are found to be 60% of static flexural strength
Germano et al. (2016)		●		●	65% to 85% of F_L stress ratio is maintained constant by varying both the maximum and minimum fatigue loads.	3 Hz	SF	0.5 and 1%	- Pre-cracked SFRC is effective in resisting low-cycle fatigue with few cycles of high stress levels than plain concrete.
Banjara and Ramanjaneyulu (2018)	●			●	65% to 85% of F_L	5 Hz	SF	0.5%, 1% and 2%	- Stiffness degradation occurs faster in specimens loaded under higher fatigue loads. - The crack opening rate is moderated with the incorporation of a higher dosage of steel fibres.

SF – Steel fibres; PF - Polymer fibres; GF – Glass fibres; Hybrid – Steel and polymer fibres; F_L- static flexural strength; F_{cr} – static flexural cracking strength; F_R – static residual strength after cracking; EL - Endurance limit by IRC 58 is highly conservative, compared to other models available in the literature, at all stress ratios, whereas IRC 46 is more reasonable.

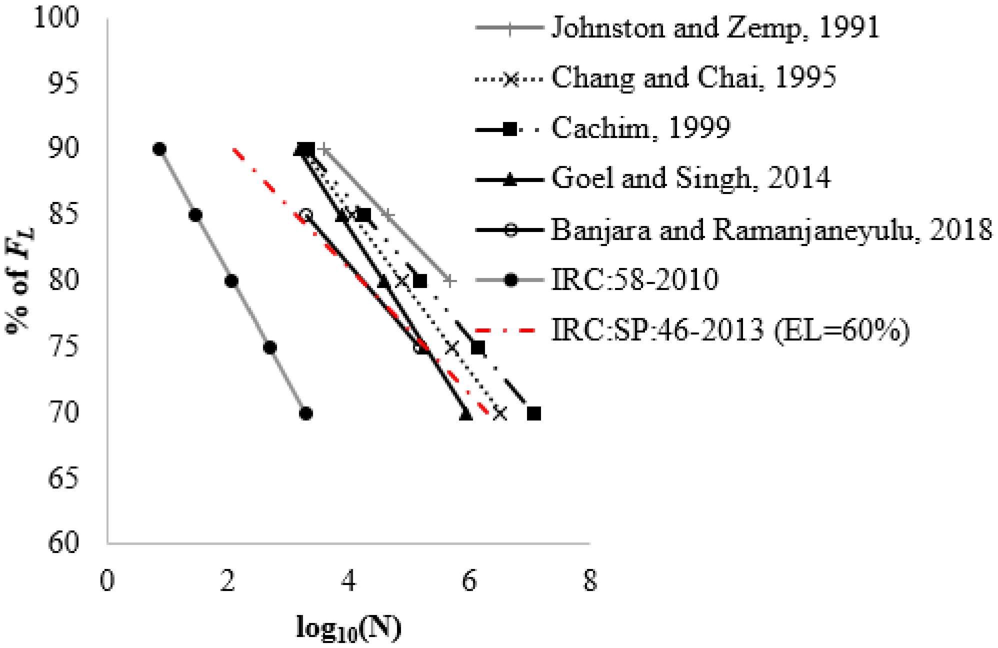

Figure 5.1 Comparison of *S-N* models based on pre-peak fatigue performance for FRC under flexure (40 kg/m^3 of steel fibres) with the model for plain concrete suggested in IRC:58-2010

Since the role of fibres is evident in the fracture process zone (i.e., in the post-peak region), it would be appropriate to determine the fatigue performance after the formation of FPZ as it replicates the real scenario of the structure under service loads (Nayar, 2015; Germano et al., 2016). However, experience in post-peak fatigue response of cracked FRC element is limited. Considering that most inelastic design of FRC structures includes the residual flexural strength of the material as input (IRC:SP:46, 2013; TR34, 2013; ACI 544.7R, 2016), for which the degradation during fatigue loading is unknown, the need for the study of fatigue performance in the post-peak regime has become imperative.

Granju et al. (2000) performed fatigue tests in the post-peak region at different stress ratios and found that the SFRC with hooked-ended steel fibres at the dosage of 65 kg/m^3 (SF65) reaches the endurance limit at 50%, in terms of the residual load carrying capacity after cracking. Germano et al. (2016) performed fatigue tests at a constant stress ratio by varying both the upper and lower fatigue limits in the post-peak region and found that when the dosage of fibres is increased from 40 kg/m^3 (SF40) to 80 kg/m^3 (SF80), the benefits of the fibres are lost and the fatigue performance decreases (Figure 5.2). However, research in the pre-peak region indicates the contrary (Ramakrishnan et al., 1989; Johnston and Zemp, 1992; Chang and Chai, 1995). This could be attributed to the fact that the specimens of Germano et al. (2016) were subjected to fatigue loading at different crack openings, unlike in the work of Granju et al. (2000). The comparison between both these works seems to be out of context as the testing procedures and types of fibres are different. Hence, in order to get a clear picture of the influence of fibre dosage in the post-peak fatigue performance, the testing procedure adopted by Granju et al (2000) is used, as the fibres are similar to those used here.

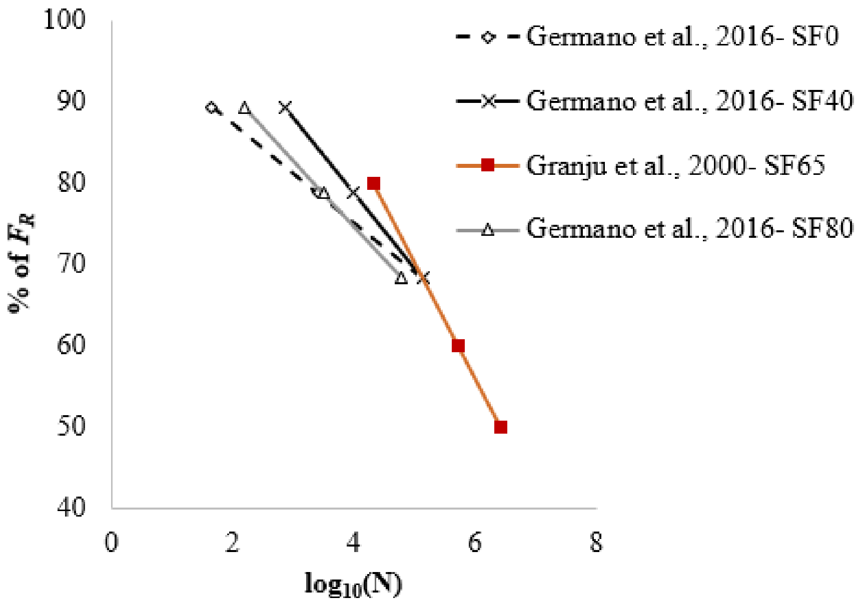

Figure 5.2 Comparison of *S-N* models available for cracked FRC in literature

From the literature survey, the suitable parameters for the current study are summarised as follows:

- In terms of testing configuration, three-point bending testing on the notched beam is chosen, so that the level of fatigue damage in terms of the crack opening can be assessed during the experiment.

- Since most of the FRC structures are designed based on inelastic analysis, it will be appropriate to perform the testing in the post-peak region to obtain the fatigue life of a structure under service. Also, there are limited investigations on the influence of fibre dosage on the post-peak fatigue characteristics, thus necessitating this study
- Fatigue testing procedure similar to that of Granju et al. (2000) is adopted, except that the pre-cracking is done until 0.5 mm instead of 0.3 mm, so that the fatigue loads can be applied as a fraction of the residual load carrying capacity at a CMOD of 0.5 mm, $F_{R,1}$, which is the main design parameter for most of the FRC structures in the serviceability limit state (SLS).
- Since the speed of loading (i.e., loading frequency) ranging between 1 and 7 Hz in general, does not significantly modify the fatigue strength of concrete (Murdock, 1965; Lloyd et al., 2007) a frequency of 5 Hz is applied in this work. Further, the frequency of traffic movement in typical urban roads in India ranges between 3 and 16 Hz (Shukla et al., 2012). Moreover, 5 Hz is the fastest loading that can be applied in the testing system available.
- The range of fatigue loading should be chosen such that the derived S-N curve can be later used for both high- and low-level fatigue stresses. Hence, the upper fatigue loading level is varied from 50 to 90% of $F_{R,1}$ (similar to Granju et al., 2000), while the lower fatigue loading level is kept constant (10% of $F_{R,1}$), and the endurance is defined at 2 million cycles.

5.3 EXPERIMENTAL PROGRAMME

Using the parameters discussed so far, the experimental programme for flexural fatigue testing is framed. The testing programme is intended to develop a fatigue model in the post-crack regime for FRC with different dosage of steel fibres. Also, an attempt is made to understand the fatigue fracture mechanisms at different fatigue loading levels.

5.3.1 Specimen details

Flexural fatigue tests were performed on M40 grade concrete reinforced with different dosages of hooked-ended steel fibres (SF), 10 kg/m^3, 30 kg/m^3 and 45 kg/m^3 (same as in the previous chapter, as discussed in Section 4.3), along with tests on reference plain concrete. Since the fatigue testing progresses for several days, the ages of all the tested specimens were more than three months, so that there was no variation of strength between the specimens. Six batches of concrete were made for each type, and five concrete beams were cast from each batch, along with cubes for compressive strength assessment. Six beams of every batch of concrete were tested for each loading range, at the age of 3 months, drawing one from each batch. The beams were given notations based on the compressive strength of the concrete, type of fibres incorporated, fibre dosage in kg/m^3 and the maximum fatigue loading level expressed as percentage of $F_{R,1}$; e.g., M40SF45_90% denotes the 40 MPa grade concrete with steel fibres (SF) at 45 kg/m^3 dosage, tested under fatigue with a maximum fatigue load of 90% of $F_{R,1}$.

5.3.2 Test procedure

The flexural testing was performed in a 1 MN closed-loop servo-controlled MTS testing system. The beam configuration conforms to EN 14651:2005, with the dimensions of the specimen being 150×150×700 mm, having a span of 500 mm; a notch of 25 mm depth was cut at the mid-span (refer Figure 4.1 in the previous chapter). The beam was loaded such that the direction of casting was perpendicular to the loading direction. The CMOD (crack mouth opening displacement) was measured using a clip gauge (of 15 mm span; the accuracy of 0.001 microns) mounted on knife edges placed across the notch faces. The beam was loaded monotonically at a standard rate under CMOD control at a rate of 1 μm/sec until it reached 0.5 mm (corresponding to the maximum allowable crack opening at SLS). At this point, the beam was unloaded and the residual load carrying capacity of the beam at a CMOD of 0.5 mm, $F_{R,1}$, was noted. Then the fatigue test was performed under load control in the post-peak region between upper fatigue load, F_u (50 to 90% of $F_{R,1}$), and lower fatigue load, F_l (10% of $F_{R,1}$), on the cracked beams at a frequency of 5 Hz. The fatigue test was performed until 2 million cycles of loading, and the application of fatigue cycle was stopped when the specimen completely broke, or the CMOD reached 5 mm, whichever occurred first. Finally, the number of cycles to failure (smaller than 2 million cycles) was plotted against the percentage of $f_{R,1}$, residual strength at a CMOD of 0.5 mm. If a specimen survives the 2 million fatigue cycle (i.e., run-out specimen), then it was tested under static loading to determine the post-fatigue response (as illustrated in Figure 5.3). The testing parameters are summarised in Table 5.2. The load-CMOD response and the corresponding number of cycles applied were acquired for every 100 cycles and for the last 100 cycles, data is logged per cycle.

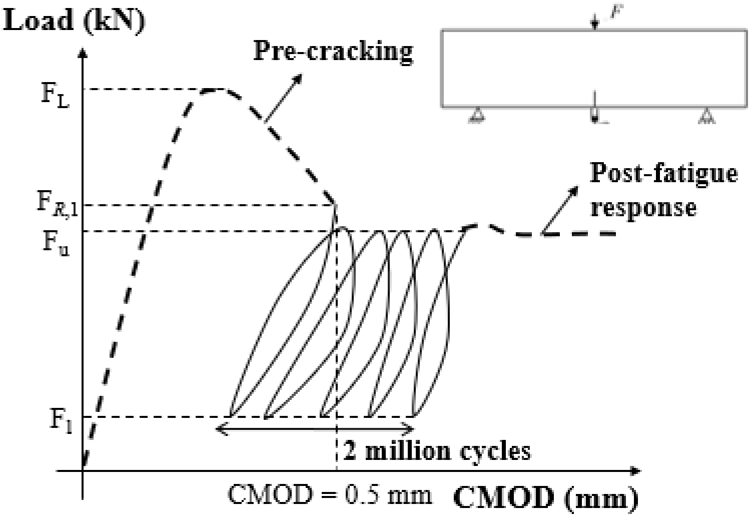

Figure 5.3 Illustration of fatigue test procedure

Table 5.2 Fatigue test parameters

Parameters	
Upper limits of load	90, 80, 70, 60, 50% of $F_{R,1}$
Lower limit of load	10% of $F_{R,1}$
Frequency of loading	5 Hz
Maximum number of cycles	2 million

5.4 RESULTS AND DISCUSSION

5.4.1 Flexural fatigue behaviour

Typical load-CMOD curves for the FRC beams obtained during pre-cracking and fatigue testing, on 3-month old specimens are shown in Figure 5.4, along with the monotonic flexural response at 28 days (grey band). The load-CMOD response for the last 100 cycles, where most of the fatigue damage occurs, is shown on the graph for the specimens that failed under fatigue loading. The curves corresponding to all the specimens are reported in Appendix D. For the plain concrete, only the number of cycles to failure is reported. Generally, for all concretes, the slope of the loading-unloading response is found not to vary significantly during the initial cycles. However, for specimens loaded at high fatigue loads, there is a significant decrease in the slope during the last few cycles before failure. At low load fatigue, there is no significant change in the slope of the loading-unloading loop for these specimens, as they undergo minor and gradual deformation. The specimens that did not fail until 2 million cycles are the ones with high dosages of steel fibres (M40SF30 and M40SF45), subjected to only 50% of $F_{R,1}$.

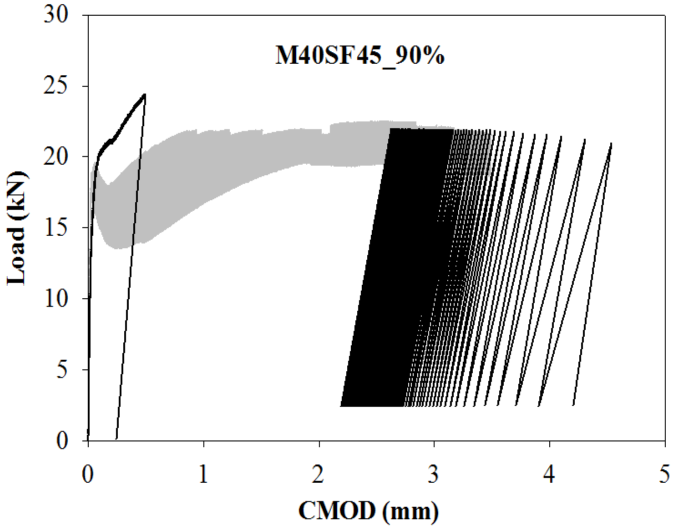

a)

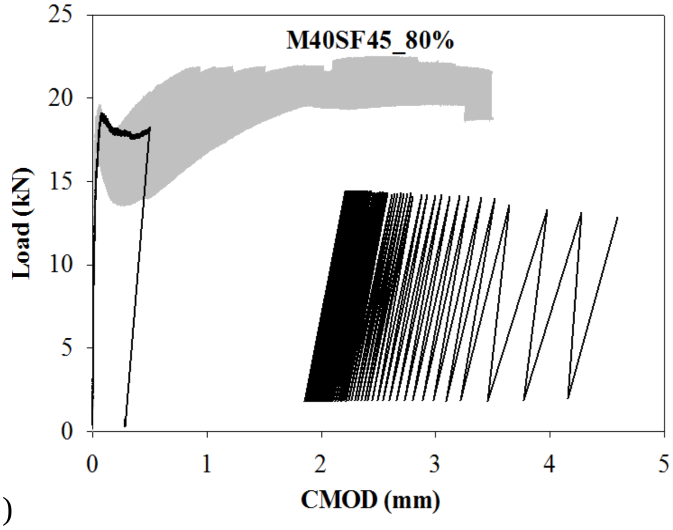

b)

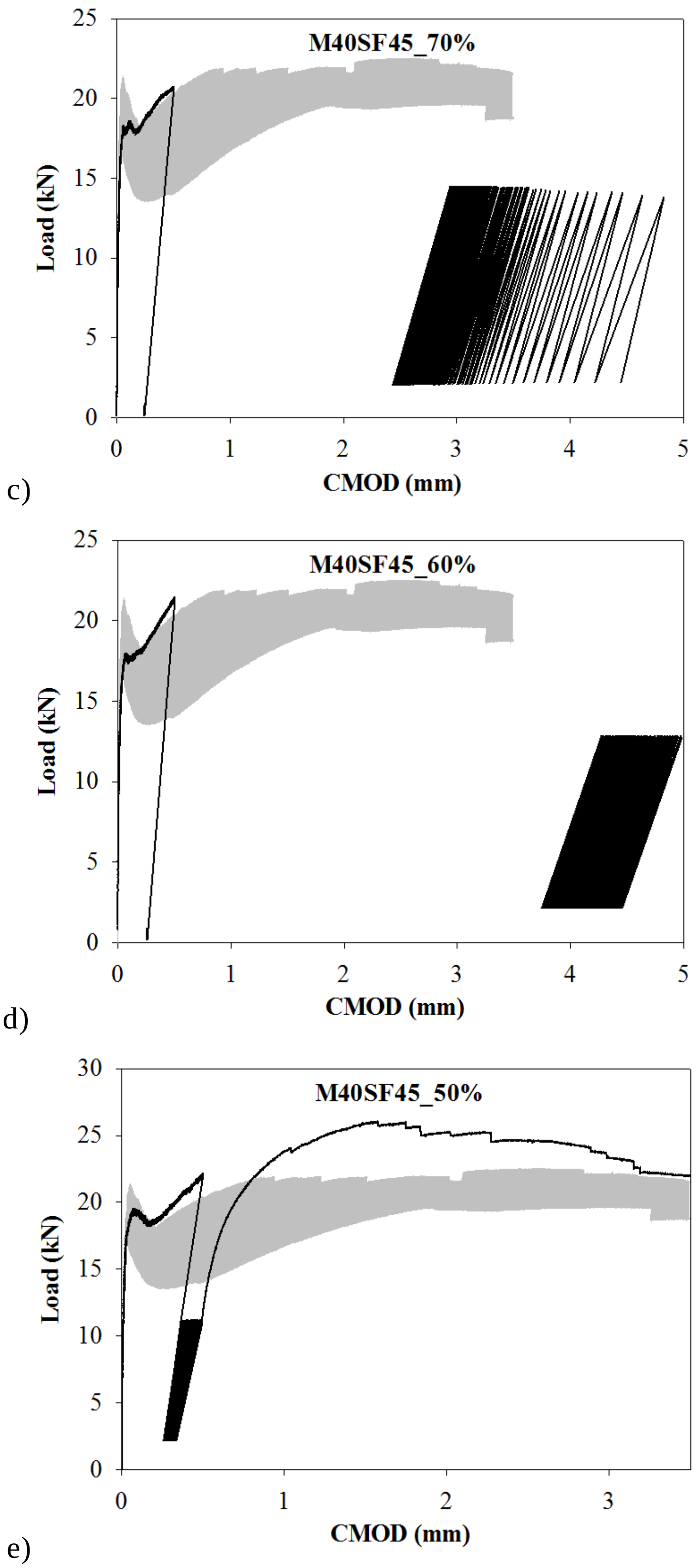

Figure 5.4 Typical load versus CMOD curves for M40SF45 concrete beams under different fatigue loading levels

The typical CMOD response of FRC with different dosages of steel fibres subjected to the different fatigue loads are shown in Figure 5.5. The rate of increase in CMOD with each cycle is found to reflect the failure mechanism described earlier (i.e., three stages of cracking). The first phase is the stabilization phase of damage, which happens at the beginning of fatigue loading. The second phase is the slow and steady damage phase, which can be identified by a linear slope in the CMOD-N curve. At this phase, fibres help mitigate the crack and limit the fatigue damage. Higher the fibre content, prolonged will be the second phase of fatigue damage. The third phase is the critical zone, where there is a sharp increase of crack opening and failure occurs consequently. The specimens loaded at high fatigue loads showed higher CMOD rates in the second stage of cracking because of the high energy imposed on the specimen within a short duration of time, which causes higher damage in the FPZ. The higher load provided causes more permanent damage during fatigue and fibres are pulled out considerably, which is reflected by the higher crack opening rate (in accordance with the work of Germano et al., 2016). Higher the crack opening rate, earlier the critical size of the crack is reached, and the specimen fails at lower cycles. In the case of M40SF10, there are lesser number of fibres in the FPZ for redistributing the stresses and prevent fatigue damage, which makes the crack progress without any inhibition. In concretes with higher dosages of steel fibres (M40SF30 and M40SF45), the growth of microcracks in the second stage is inhibited by the more closely spaced fibres in the concrete matrix and the number of cycles to failure increases compared to concrete with low dosage of fibres. The enhanced bond strength and mechanical anchorage of hooked-ends (i.e., fibre bridging and pull-out action) help in delaying fatigue damage. It is also observed that the specimens that withstood 2 million cycles only undergo first and second stages of damage under fatigue, as the critical CMOD is never reached (Figure 5.5). The damage in the FPZ is minimal because of the application of low fatigue load (50% of $F_{R,1}$), and the fatigue loading does not cause any significant damage. Consequently, the residual load-carrying capacity does not decrease beyond this load level. Also, there is no increase in FPZ, and the undamaged ligament length helps in resisting the fatigue loading.

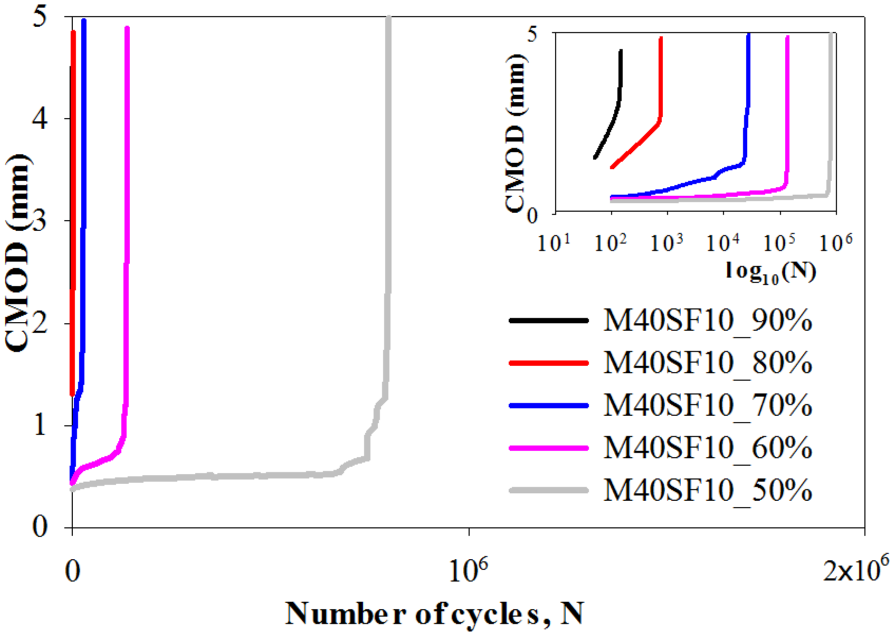
CMOD (mm)
0
1
2
3
4
5
0
10^6
2x10^6
Number of cycles, N
CMOD (mm)
0
5
10^1
10^2
10^3
10^4
10^5
10^6
log10(N)
M40SF10_90%
M40SF10_80%
M40SF10_70%
M40SF10_60%
M40SF10_50%

a)

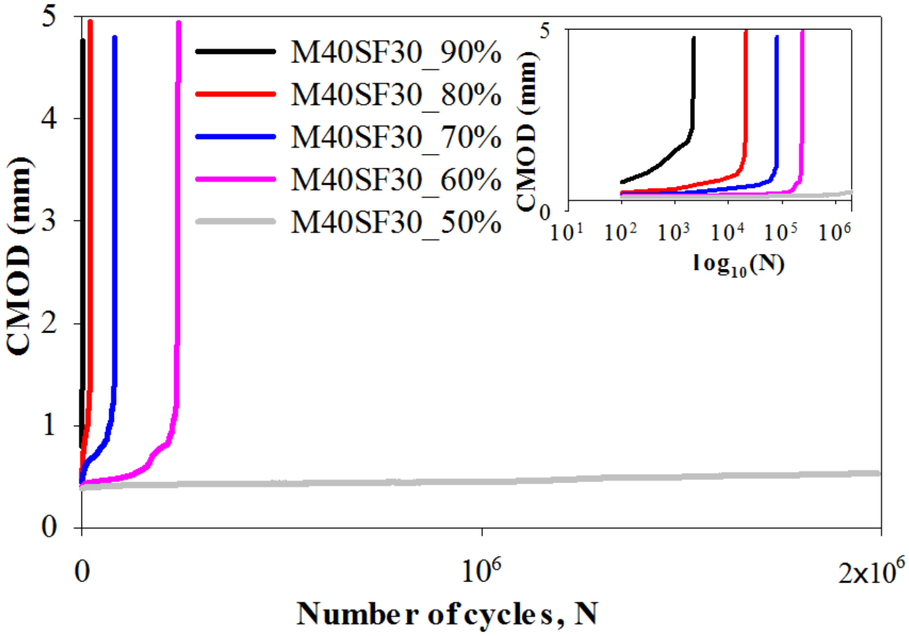
CMOD (mm)
0
1
2
3
4
5
0
10^6
2x10^6
Number of cycles, N
M40SF30_90%
M40SF30_80%
M40SF30_70%
M40SF30_60%
M40SF30_50%
CMOD (mm)
0
5
10^1
10^2
10^3
10^4
10^5
10^6
log10(N)

b)

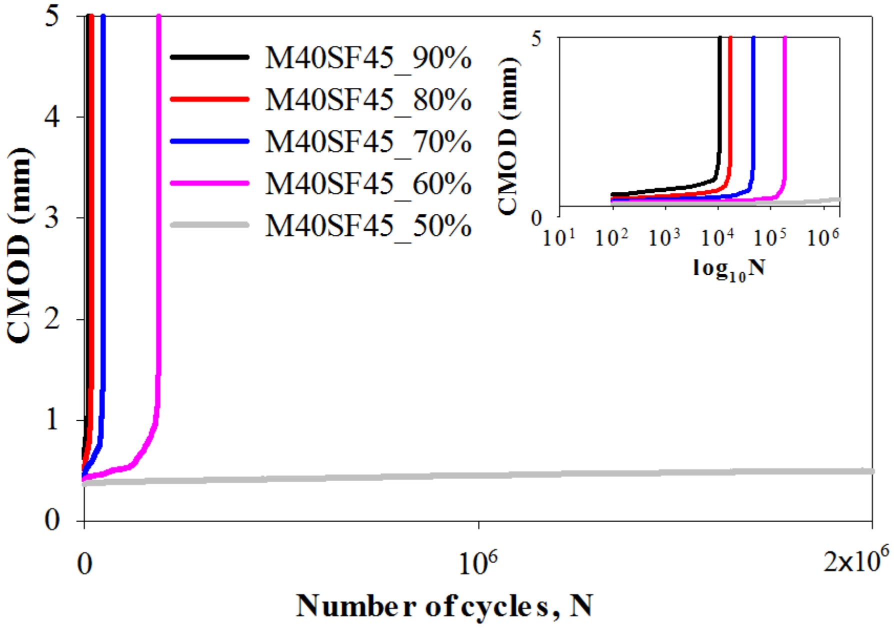

c)

Figure 5.5 Typical CMOD vs. N response of a) M40SF10 b) M40SF30 and c) M40SF45 concrete (inset CMOD vs. $\log_{10}N$)

The rate of increase in CMOD with fatigue loading is computed as $\Delta CMOD = (CMOD_n - CMOD_m)/(n-m)$, $CMOD_n$ and $CMOD_m$ being the CMODs at the end of n and m cycles, respectively. It is observed that the CMOD rate per cycle generally decreases and then increases (see Figure 5.6 to 5.8) There is a distinctive critical point, denoted as $CMOD_{cr}$ where the CMOD rate starts increasing (Figure 5.6 to 5.8, and Table 5.3). It is seen that the rate of crack opening is very steep for specimens loaded under high fatigue loads. Also, it is observed that $CMOD_{cr}$ is lower for specimens subjected to lower fatigue loads, when compared to that of higher fatigue loads. Even though the increase in CMOD is gradual at low fatigue loads, due to the higher fatigue cycles, the FPZ is progressively damaged leading to a lower $CMOD_{cr}$.

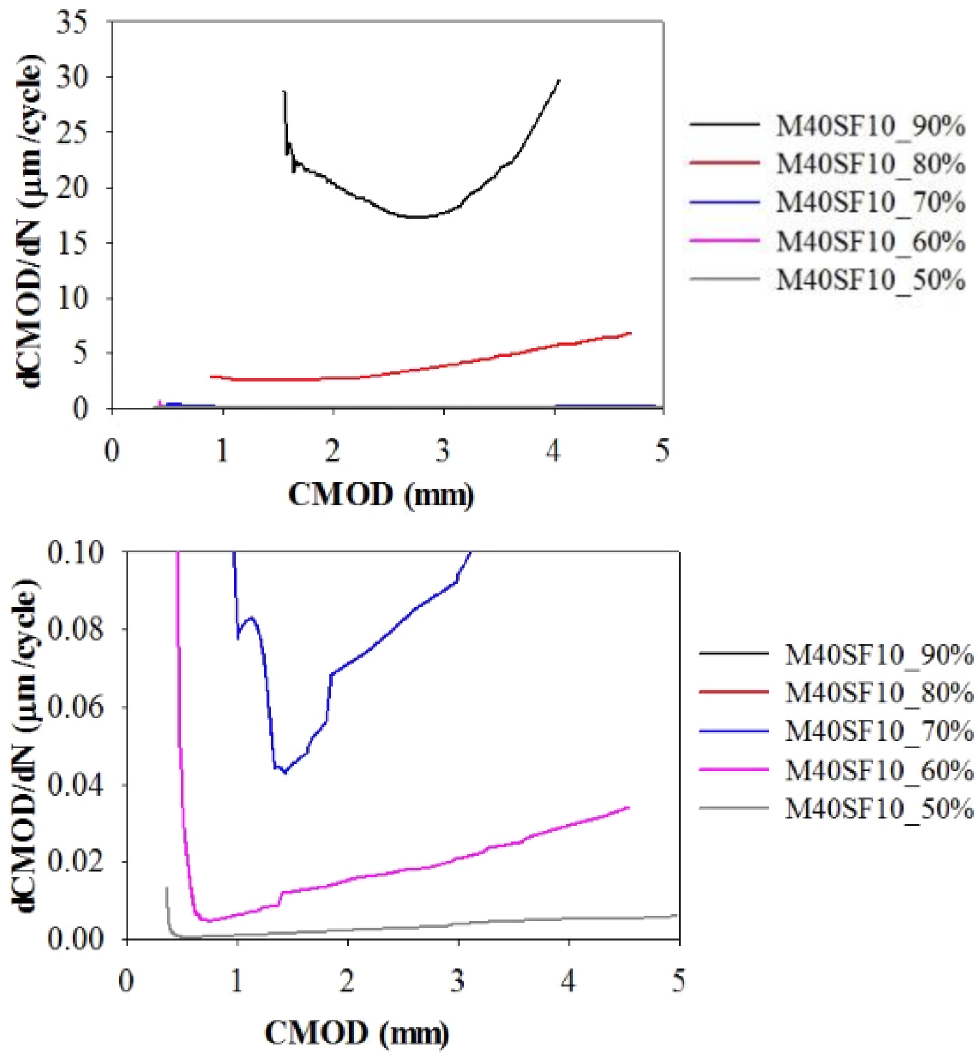

Figure 5.6 Typical CMOD rate under fatigue loading for M40SF10

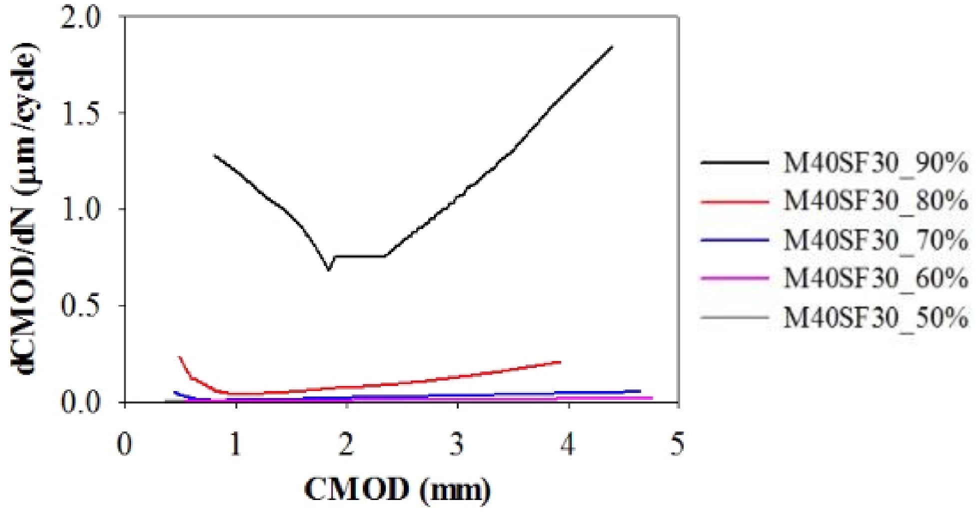

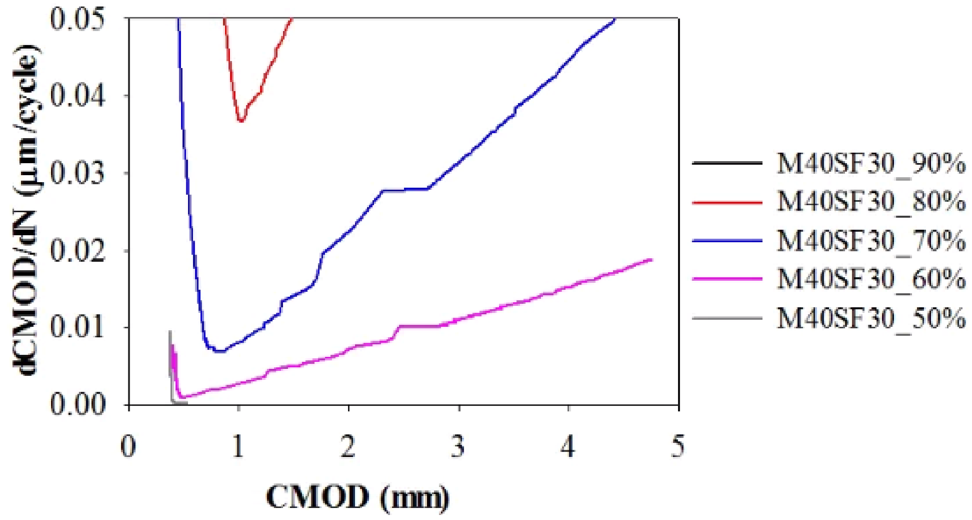

Figure 5.7 Typical CMOD rate under fatigue loading for M40SF30

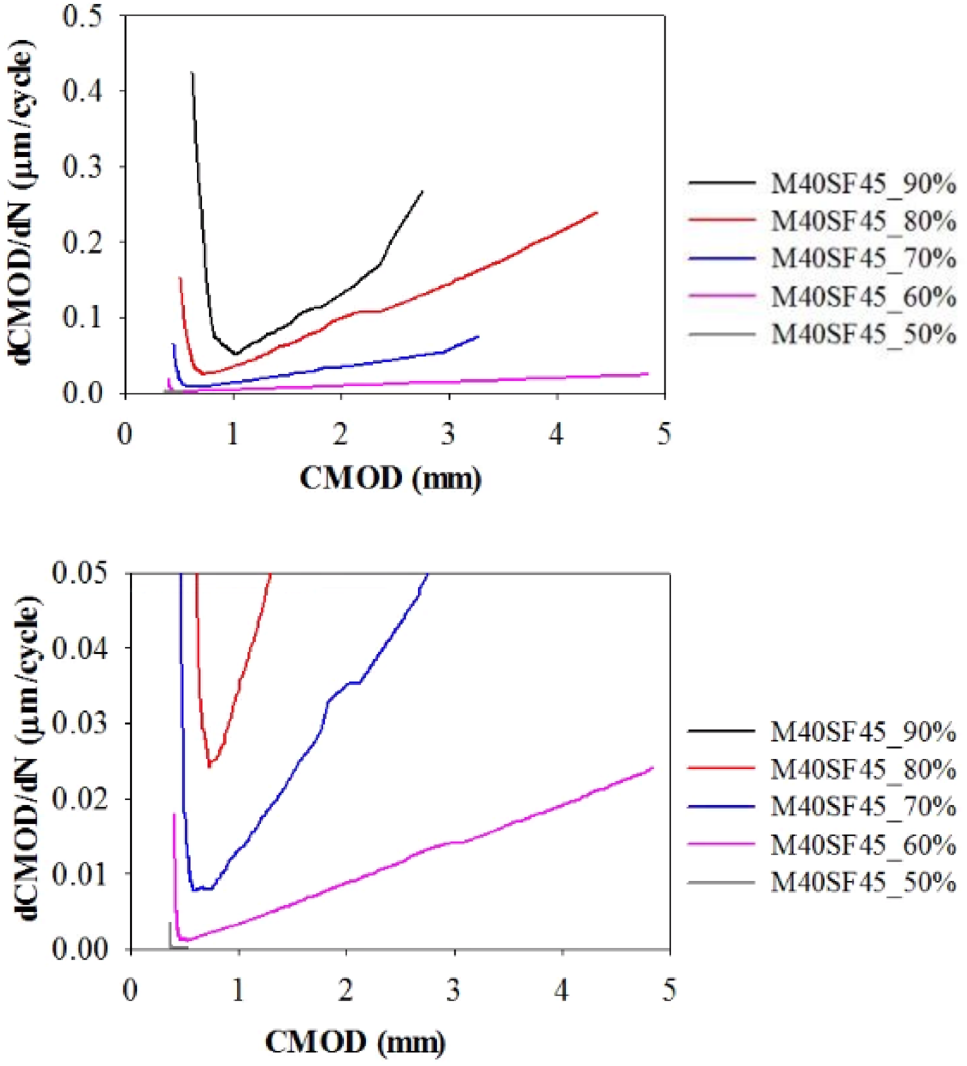

Figure 5.8 Typical CMOD rate under fatigue loading for M40SF45

Table 5.3 Critical CMOD at different fatigue loading levels

Specimen ID	**%$f_{R,1}$**	**CMOD$_{cr}$ (mm)**
M40SF10	90	1.68±0.71
	80	1.98±0.61
	70	1.19±0.29
	60	0.60±0.09
	50	0.51±0.07
M40SF30	90	1.99±0.45
	80	1.13±0.21
	70	0.79±0.17
	60	0.54±0.07
	50	-
M40SF45	90	1.19±0.16
	80	0.96±0.15
	70	0.63±0.06
	60	0.56±0.07
	50	-

The degradation in load-CMOD slope also represents the reduction in stiffness of the concrete, which is prominent in specimens loaded at high fatigue loads (see Figure 5.9). The flexural stiffness of the specimen, calculated as the secant stiffness computed between the maximum and minimum fatigue load levels of each cycle, has been determined using the load-CMOD response during fatigue load application (Figure 5.9). The degradation in stiffness is more rapid for specimens loaded at higher fatigue loading levels as the crack opens more when compared to that subjected to lower fatigue loads. Higher the fibre content, higher is the absolute stiffness during fatigue (which is in accordance with the work of Chang and Chai, 1995), due to the lower fatigue damage. For concrete with a higher dosage of steel fibres subjected to low fatigue loads, the degradation of stiffness is found to be very low and gradual compared to that subjected to higher fatigue loads.

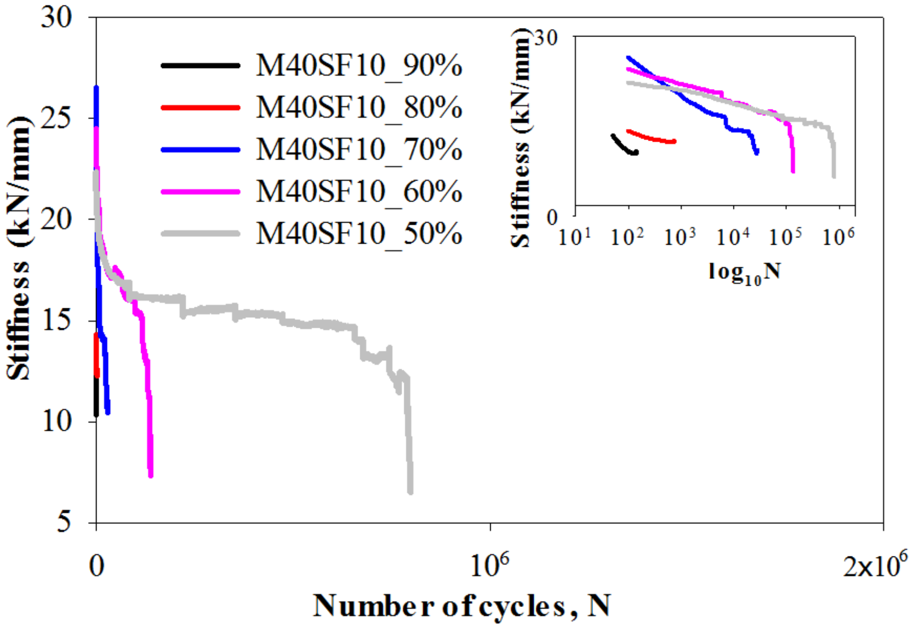

a)

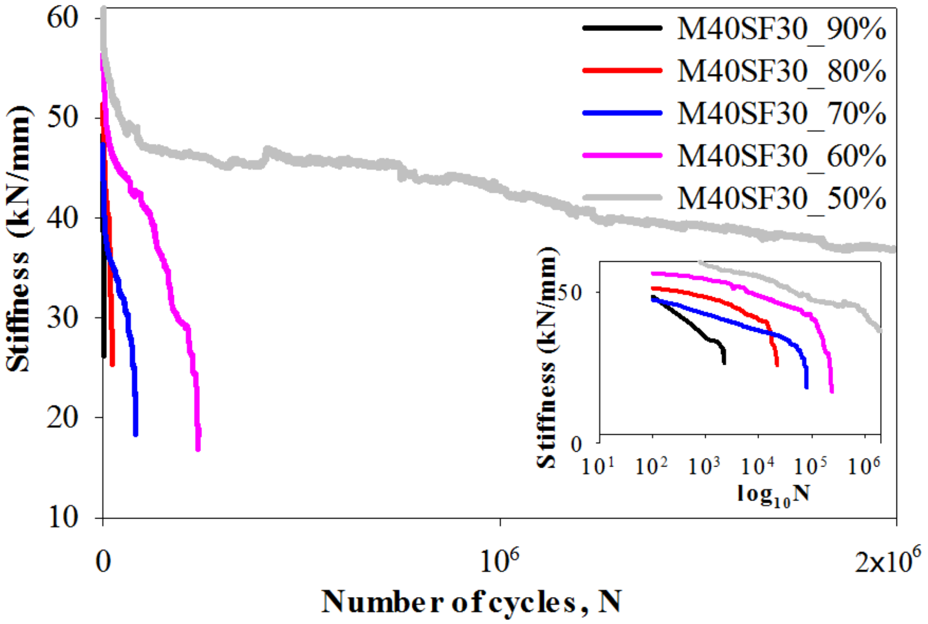

b)

c)

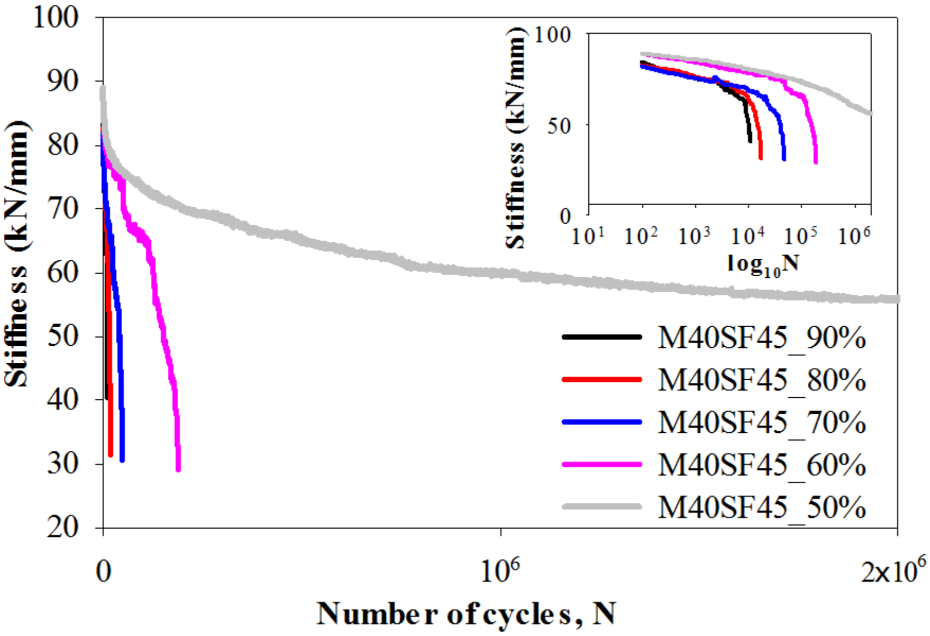

Figure 5.9 Typical degradation of stiffness with fatigue cycles for different concretes

Thus, the increase in CMOD at upper fatigue load can be generally represented using Figure 5.10a. The CMOD at the end of the second phase is termed as critical CMOD ($CMOD_{cr}$), which is subsequently followed by a sharp increase in CMOD prior to failure (failure is denoted as × in Figure 5.10). The corresponding increase in CMOD rate and reduction in flexural stiffness with fatigue damage are shown in Figure 5.10 b) and c). During the first few fatigue cycles, the FPZ is smaller than that created earlier by the pre-cracking loading. With the application of the fatigue loading, only few fibres are active and hence there is an increase in CMOD with decreasing rate as more fibre are activated. However, when the FPZ increases, the number of fibres taking part in the crack bridging increases and hence the CMOD increase is gradual at this stage. Upon further increase in fatigue cycles, the fibre breaks or pulls out increasing the crack length, which eventually reduces the residual strength of the material. This causes a rapid rise in CMOD, which in turn reduces the stiffness significantly, causing failure. When the load carrying capacity at a particular CMOD is lower than the applied fatigue load, the specimen fails, as expected.

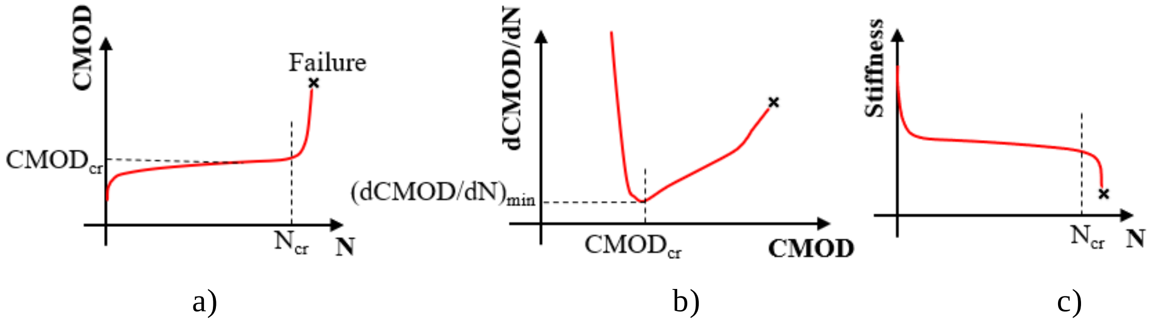

Figure 5.10 Fatigue response: a) increase in CMOD during fatigue loading, b) rate of increase in CMOD during fatigue loading and c) decrease in stiffness with fatigue loading

5.4.2 *S-N* models for representing fatigue failure

The relationships between the maximum fatigue loading as a percentage of the monotonic capacity $F_{R,1}$ and the number of cycles to failure, commonly referred as the *S-N* relationships, are derived based on linear regression performed on each set of data (i.e., 6 specimens for each loading level) and plotted in semi-logarithmic scale. The *S-N* or Wöhler diagrams along with the 95% confidence band for each type of concrete are shown in Figure 5.11. The experimental results for each maximum fatigue loading level for a particular dosage were statistically analyzed based on the ASTM E739-10 (2015) Standard, that defines the 95% confidence band. The 95% confidence band is hyperbolic, and here the statistical analysis is conducted with the runout result. The solid line in the diagram represents the linear fit (*S-N* curve) and is expressed by the following equation as (ASTM E739-10, 2015):

$$Y = A + BX\,;\, Y = \log_{10} N \text{ and } X = \log_{10}(\%F_{R,1}) \tag{5.1}$$

where A and B parameters of the *S-N* model, *N* corresponds to number of cycles to failure and $\%F_{R,1}$ corresponds to the maximum fatigue loading level as a percentage of $F_{R,1}$. A and B can be determined by the following equations:

$$A = \overline{Y} - B\overline{X} \tag{5.2}$$

$$B = \frac{\sum_{i=1}^{k}(X_i - \overline{X})(Y_i - \overline{Y})}{\sum_{i=1}^{k}(X_i - \overline{X})^2}\,;\, \sum_{i=1}^{k}\overline{X} = \frac{X_i}{k} \text{ and } \sum_{i=1}^{k}\overline{Y} = \frac{Y_i}{k} \tag{5.3}$$

where k is the total number of samples tested. The dotted lines in Figure 5.11 are the upper and lower limits of the 95% confidence band computed using the following equation:

$$A+BX\pm\sqrt{2F_p}\,\sigma\left[\frac{1}{k}+\frac{(X-\overline{X})^2}{\sum_{i=1}^{k}(X_i-\overline{X})^2}\right]^{1/2} \tag{5.4}$$

where F_p depends on the sample size and is derived from ASTM STP:313 (1962). The expression for estimating the variance of the normal distribution (σ) for $\log_{10}N$ is

$$\sigma=\left[\frac{\sum_{i=1}^{k}(Y_i-\widehat{Y}_i)^2}{k-2}\right]^{1/2}\quad;\widehat{Y}_i=A+BX_i \tag{5.5}$$

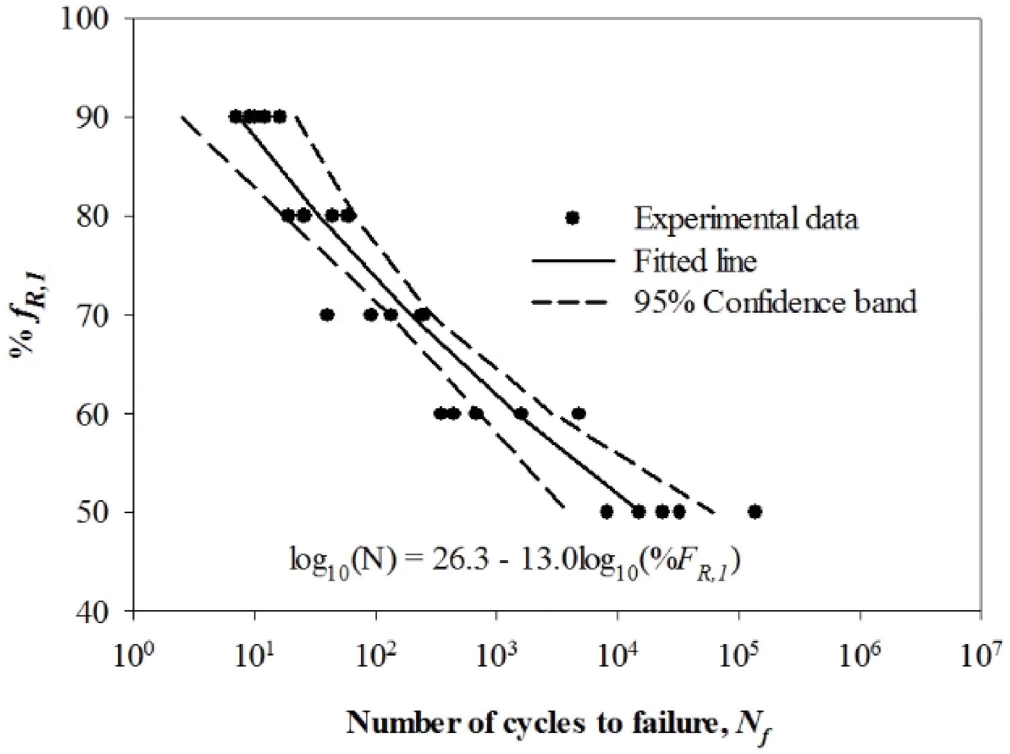

a)

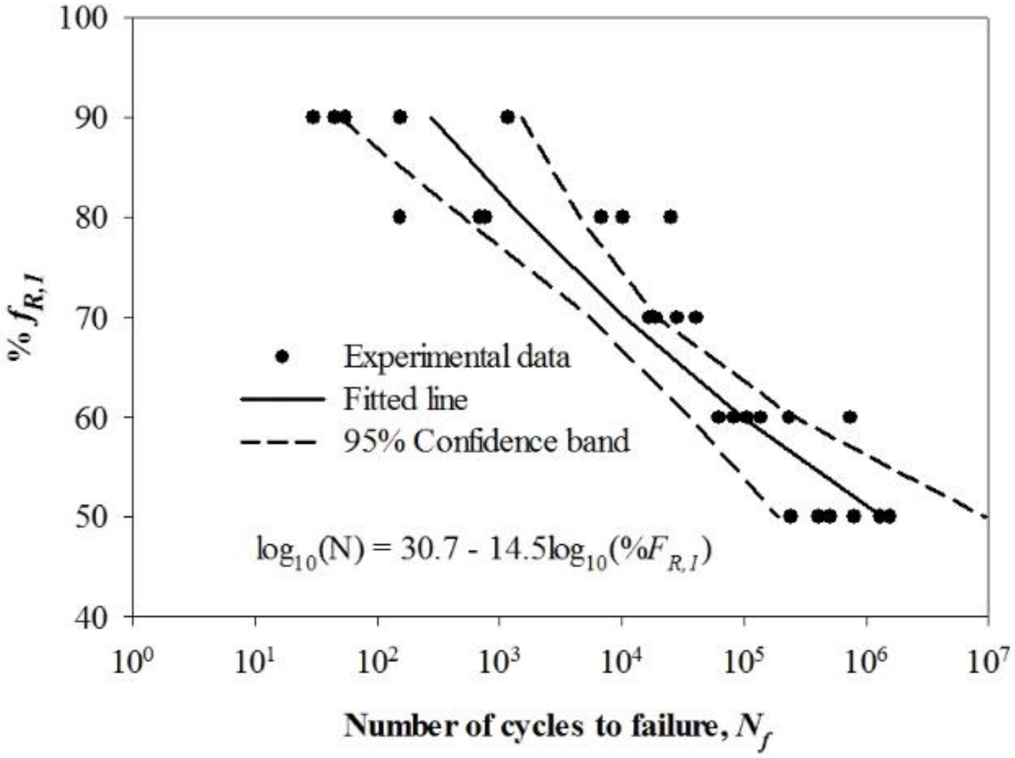
100
90
80
70
60
50
40
% $f_{R,1}$
Experimental data
Fitted line
95% Confidence band
$\log_{10}(N) = 30.7 - 14.5\log_{10}(\%F_{R,1})$
10^0
10^1
10^2
10^3
10^4
10^5
10^6
10^7
Number of cycles to failure, N_f

b)

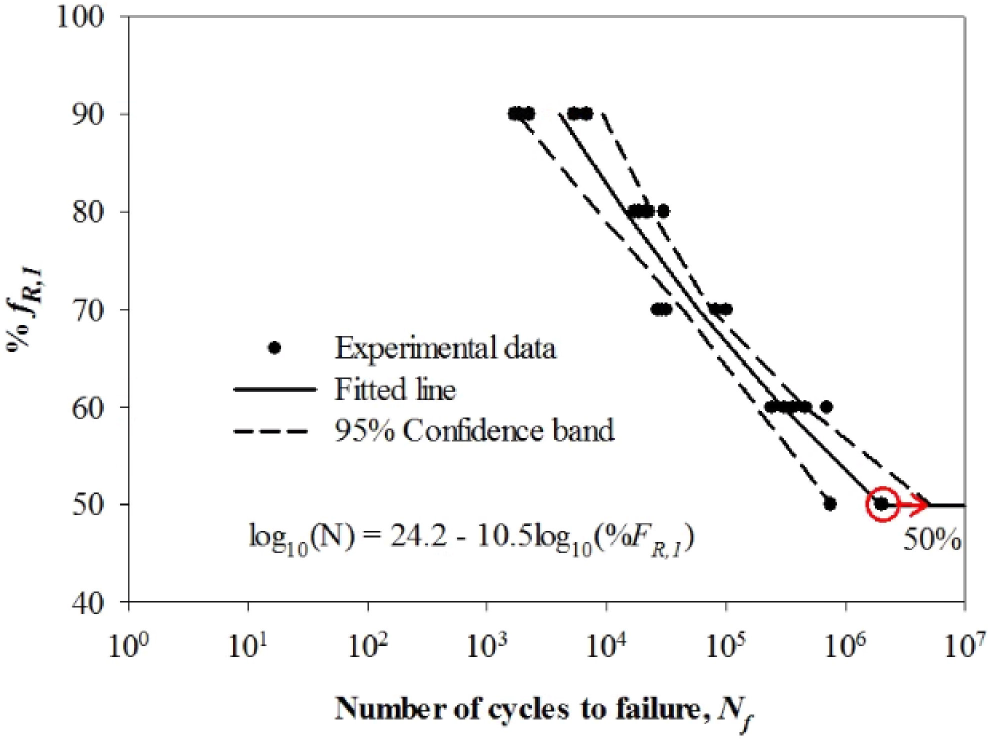
100
90
80
70
60
50
40
% $f_{R,1}$
Experimental data
Fitted line
95% Confidence band
$\log_{10}(N) = 24.2 - 10.5\log_{10}(\%F_{R,1})$
50%
10^0
10^1
10^2
10^3
10^4
10^5
10^6
10^7
Number of cycles to failure, N_f

c)

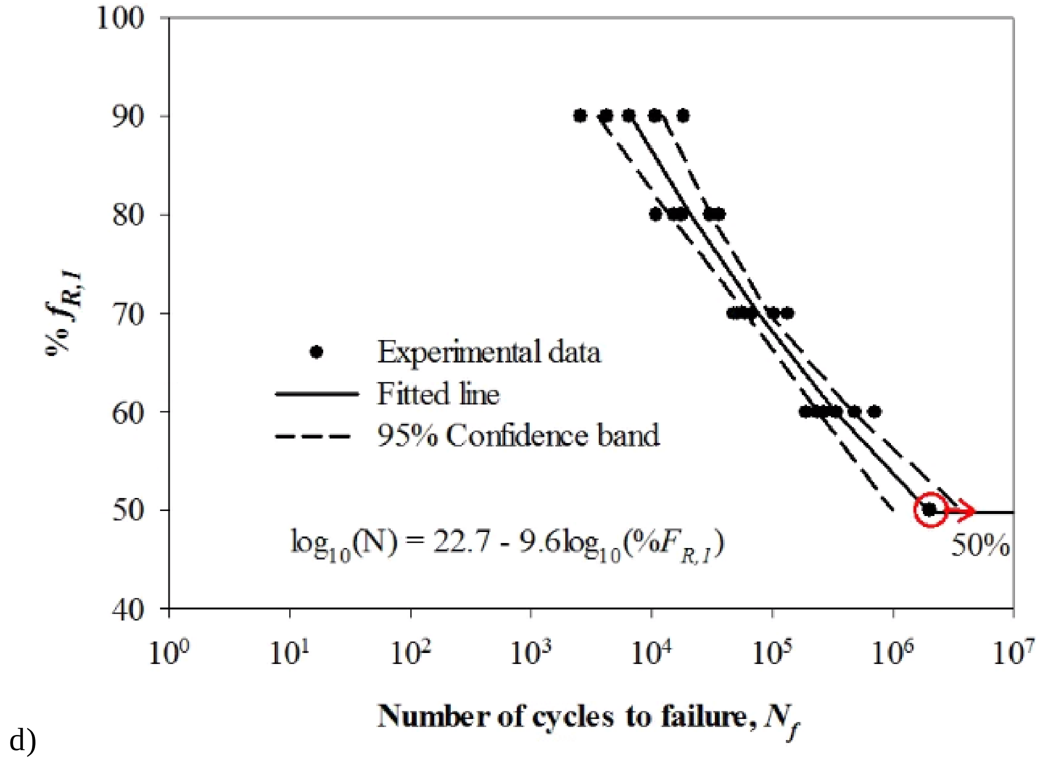

Figure 5.11 *S-N* curves for FRC reinforced with a) 0 kg/m^3 b) 10 kg/m^3, c) 30 kg/m^3, and d) 45 kg/m^3 of steel fibres

Using the above equations, the *S-N* curve is drawn in each case. It is evident that, by applying high fatigue loads, the fatigue damage occurs faster, and specimen fails after fewer cycles and vice versa. It is observed that the concrete with a lower dosage of steel fibres exhibited higher scatter when compared to concrete with a higher dosage of steel fibres. Incorporation of higher dosage of fibres reduces the probability of failure significantly. The circles in the plots (Figure 5.11c and d) represents specimens that withstood 2 million cycles (i.e., run-out specimens) at very low fatigue levels. The number of specimens that survived the fatigue failure is 5 for M40SF30 and 6 for M40SF45. Since the runout occurs at the lowest loading level, it could be considered that the endurance limits for both M40SF30 and M40SF45 are about 50% of $F_{R,1}$, which is in accordance with the conclusion of Granju et al. (2000) for similar fibres at the dosage of 65 kg/m^3

The *S-N* curves obtained for each concrete are superimposed to understand the increase in fatigue performance with the dosage of fibres in Figure 5.12. When the *S-N* models of concrete with and without fibres are compared (i.e., M40SF0 and M40SF10), there is a significant shift in the regression line to the right, representing the increase in fatigue life in all loading levels. From this behaviour, it could be conjectured that the incorporation of even a low dosage of fibres could significantly improve the fatigue performance of concrete due to the crack bridging ability. With further increase in fibre dosage, the slope of the regression line becomes steeper. This implies that the benefit of the addition of fibre is more pronounced in high fatigue loading levels and is not significant at low loading levels. In the case of high fatigue loading, the energy supplied is high and the crack opening is wider that the length of FPZ, which is formed during pre-cracking, increases. For concrete with a high dosage of steel fibres, the number of fibres in the FPZ resisting crack opening will be higher and hence the fatigue life is increased, compared to that with a low dosage of fibres. However, when low fatigue loads are applied, there is no significant difference in life with the incorporation of high dosage of fibres (M40SF30 and M40SF45). This is because of the lower energy supplied to the specimen and lower crack widths during the fatigue loading, which does not further increase the length of FPZ. Only some of the fibres that are already present in the FPZ will help in resisting the fatigue damage. The fatigue life of M40SF30 and M40SF45 is seen to be similar. Moreover the data of Granju et al. (2000) for the SFRC with 65 kg/m^3 of steel fibres had almost similar fatigue life as that of 45 kg/m^3, which means that the fatigue performance of the concrete does not improve substantially after a certain dosage of steel fibres.

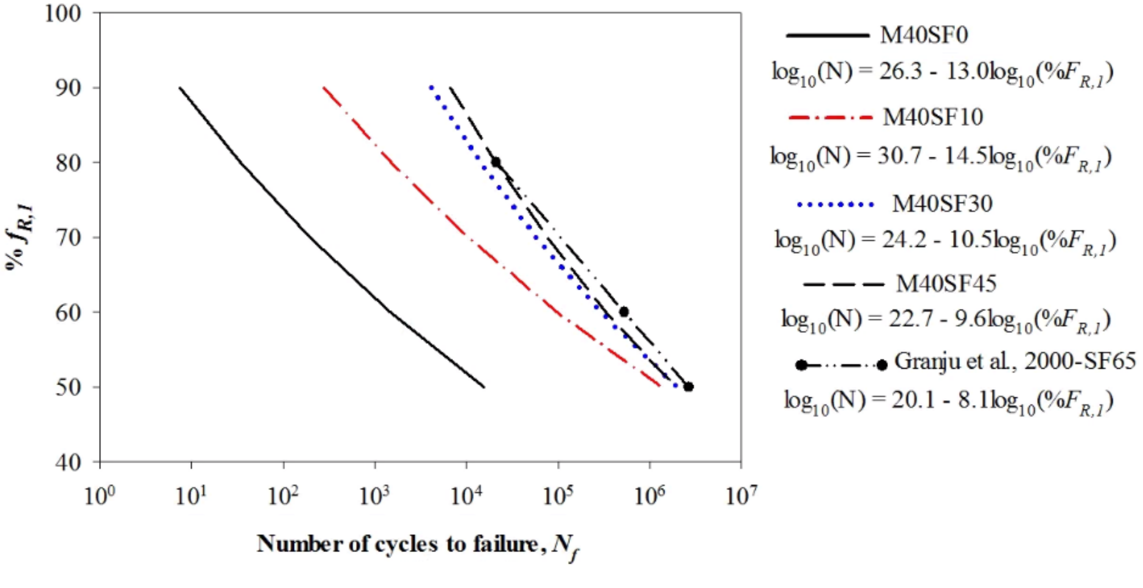

Figure 5.12 Comparison of *S-N* model for concretes with different dosage of steel fibres.

Based on the trends seen, a generalized model is developed based on regression analysis and is expressed as:

$$\log_{10} N = A + B \log_{10}(\% F_{R,1}) \tag{5.6}$$

where, A and B are fatigue coefficients based on the dosage of steel fibres in concrete, $F_{R,1}$ is the residual load carrying capacity at CMOD = 0.5 mm, and N is the number cycles to failure. The values obtained for the coefficients are:

A = 26.3 for plain concrete
 30.7 for dosages less than 30 kg/m^3 of steel fibres
 24.2 for dosages greater than 30 kg/m^3 of steel fibres
B = 13.0 for Plain concrete
 14.5 for dosages less than 30 kg/m^3 of steel fibres
 10.5 for dosages higher than 30 kg/m^3 of steel fibres

This proposed equation comprises the model for the fatigue response of FRC that can be used in analysis and design.

5.4.3 *S-N* model based on critical CMOD

The *S-N* models developed based on the number of cycles to reach critical CMOD for FRC with different dosages of steel fibres are shown in Figure 5.13. The slope of these models is similar to that of the *S-N* models based on the number of cycles to failure for the corresponding concrete. This means the number of cycles to failure and number of cycles to reach the critical CMOD are closely related irrespective of the fibre dosage. By using this model, the failure could be considered for design as the condition when crack opening reaches the critical value, so that the CMOD does not reach the ULS. This way, the probability of failure can be further reduced for structural elements of higher importance, which could have lower maximum allowable crack width. Using this model in design, the safety of the structure can be further improved because the crack growth is prevented from becoming unstable under fatigue.

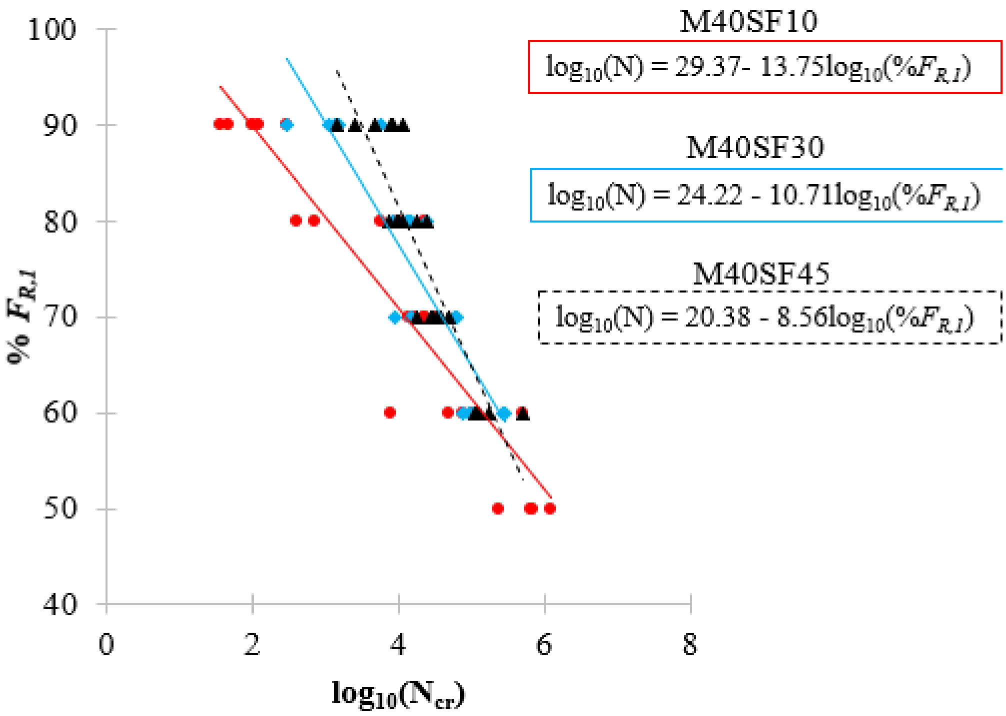

Figure 5.13 *S-N* model based on critical CMOD for FRC reinforced with different dosages of steel fibres

5.5 CONCLUSIONS

In this chapter, the fatigue performance of concrete reinforced with different dosages of steel fibres has been assessed. The evolution of fatigue damage with cyclic loading is obtained based on the progressive increase in crack opening and degradation of stiffness. Regression analysis was carried out on the experimental flexural fatigue data to develop relationships between the number of cycles to failure and applied stress ratio. This fatigue model is suited for the fatigue life of cracked FRC with different toughness. The major findings of this study are as follows:

- The *S-N* diagram of the fatigue data shows wide scatter, which is common in concrete; however, with an increase in dosage of fibres, the scatter decreases.
- The fatigue life of concrete subjected to high fatigue loads can be improved significantly by the incorporation of fibres. Higher dosages of fibres are best suited for structures that experience higher magnitude of fatigue stresses.

- At lower fatigue loads, higher fibre dosages do not have any significance. This is because of the lower energy supplied to the specimen and lower crack widths during cyclic loading does not further increase the length of FPZ. Only some of the fibres that are already present in the FPZ will help in resisting the fatigue damage.
- Even though the fatigue performance of concrete with lower dosage of steel fibres is poorer than that of high dosage of steel fibres, adding a low dosage of steel fibres can significantly improve the fatigue performance of concrete. Hence, low dosage of steel fibres can be incorporated in structures that are subjected to low fatigue cycles.
- By using the developed model, the fatigue performance of FRC can be designed for. With increased usage of FRC, considering its higher durability and fatigue life, the established model could be suitable for the design of pavements and other structures.
- Using the *S-N* model based on the critical CMOD in design, the safety of the structure can be further improved because the crack growth is prevented from becoming unstable under fatigue.

6 INCORPORATION OF TIME-DEPENDENT FRACTURE PROPERTIES IN STRUCTURAL DESIGN

6.1 GENERAL

The time-dependent variations of toughness and fracture properties of fibre reinforced concrete (FRC) have been investigated by studying the influence of quasi-static loading rates and fatigue loading in the previous chapters, where the need to consider these aspects in the incorporation of steel fibres has been demonstrated. FRC structural elements, such as tunnel lining segments, pavements and elevated slabs, that utilise the residual strength of the material as a design parameter and that are most likely to be subjected to prolonged and fatigue loading (tensile or flexural) during their design life have been considered here to develop a comprehensive methodology incorporating time-dependent models.

The objective of this chapter is to analyze some elements that are primarily designed based on toughness parameters and a comprehensive methodology to incorporate the loading rate and fatigue loading effects is proposed. The models developed for FRC subjected to long-term static and dynamic loadings are used as the design input for structural elements, whichever is appropriate. In this context, the design of tunnel lining segments, pavements and elevated slabs that is done considering the residual strength parameters is discussed and finally, recommendations for design are made, including a proposal for design based on the modified toughness parameters considering the long-term static loading and fatigue loading.

6.2 DESIGN MODIFICATIONS USING TIME-DEPENDENT MODELS

The tunnel segments under service must withstand slow soil settlement and groundwater movement. Likewise, elevated slabs used for industrial purposes must bear heavy static to impact loads and load cycling during the stacking of racks. Even though these structural elements are designed for such magnitude of loads, the variation of moment carrying capacity with loading rate is not generally considered in analysis and design. The present rate-effect model accounts for the tensile strength and residual bridging strength at different loading rates (Chapter 4, Section 4.5) and can be incorporated in the design appropriately.

In addition to prolonged loading, some FRC structures are subjected to fatigue loading under service, which could be in the form of traffic movement, temperature variation, wind action, etc. Fatigue reduction factors *X* and *Y* can be derived using the pre-peak and post-peak fatigue model, respectively, as illustrated in Figure 6.1, and the corresponding pre-peak and post-peak strength parameters that are involved in the design can be modified. Since the pre-peak fatigue performance has been studied extensively by various researchers, the S-N model suggested in the literature such as that of IRC:SP:46 (2013) for FRC can be used. In the case of post-peak fatigue model, the S-N model derived in Chapter 5, Section 5.4.2, for FRC with different dosages of steel fibres is proposed to be used. The values of the reduction factor for FRC reinforced with different dosage of steel fibres, which will be used in the design procedure, are listed in Table 6.1.

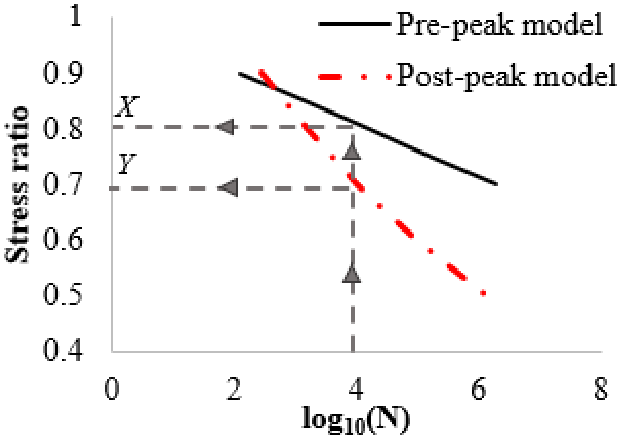

Figure 6.1 Fatigue reduction factors derived from S-N curves

Table 6.1 The values of the fatigue reduction factors for desired fatigue life for FRC with different dosages of steel fibres

N	*X*			*Y*		
	M40SF10	M40SF30	M40SF45	M40SF10	M40SF30	M40SF45
1000	0.75	0.86	0.86	0.82	1.00	1.00
10,000	0.67	0.81	0.81	0.70	0.83	0.86
1,00,000	0.59	0.76	0.76	0.59	0.66	0.68
20,00,000	0.50	0.70	0.70	0.48	0.50	0.50

6.3 DESIGN OF TUNNEL LINING SEGMENTS

Precast concrete tunnel lining segments are installed to provide both initial ground support, and final lining for tunnels installed with tunnel boring machine (TBM) in hard ground and weak rock applications. The TBM advances by thrusting against the completed rings of the tunnel segments that are also typically designed to resist the permanent loads from the ground and groundwater, as well as the temporary loads from fabrication, transportation and construction. These segments are generally reinforced to resist some tensile stresses at both the serviceability (SLS) and the ultimate limit states (ULS) (fib Model, 2010). Since both localized and distributed stresses are generally present in tunnel linings, recent construction practices use a combination (hybrid) of conventional reinforcement bars (rebars) and fibre reinforcement. FRC can be used to withstand bursting and spalling stresses developed during the production, transportation and placement of precast concrete segments, with the added benefit of increasing safety. In the recent years, the introduction of high performance FRC has further led to the use of fibres as the sole reinforcement for more challenging conditions (Figure 6.2 shows the increase in usage of FRC in tunnel lining projects).

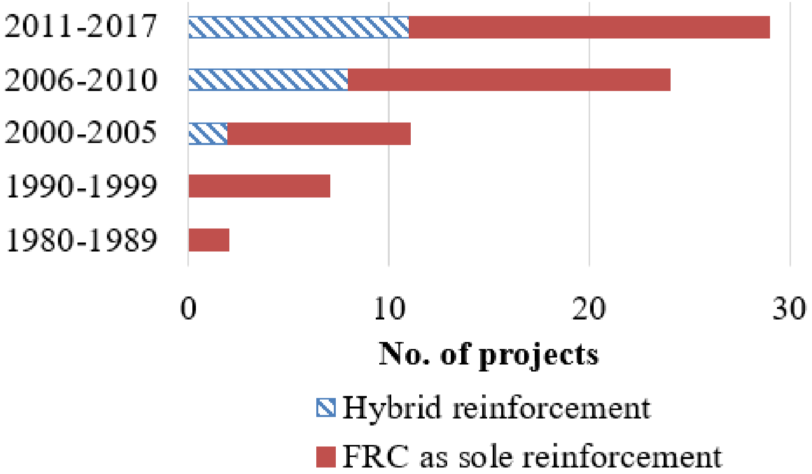

Figure 6.2 Evolution of FRC in the tunnel segment industry (ITA Report, 2016)

The compressive and tensile strength of concrete, and post-crack residual strength (or toughness) provided by the fibres are the primary design parameters for FRC tunnel segment (Nanakorn and Horii, 1996b; Plizzari and Cominoli, 2005; Sorelli and Toutlemonde, 2005; Buratti et al., 2013; ACI 544.7R, 2016). Under service, these segments are subjected to long-term loading and/or fatigue loading, depending on the type of tunnel. For instance, if the tunnel is designed for traffic movement, then the segments must be designed for both long-term and fatigue loading. Hence, in the design process of the FRC tunnel lining segments, the time-dependent models are to be incorporated at the different stages of loading conditions, wherever appropriate. For illustration of the conventional design procedure, a tunnel segment with thickness, *t*, the radius at the mid thickness, *R*, width, *w*, number of segments per ring, *n* is used. The bending moment developed at various loading conditions is discussed in the following sections, and the time-dependent models are incorporated where appropriate.

6.3.1 Load Case 1: Demoulding

The precast tunnel segment is demoulded at the plant once the required strength of the concrete has reached. The segments are lifted from the moulds using mechanical lifting devices and taken to the stacking yard. The demoulding is generally carried out 4 to 6 hours after casting, and hence, the check will be done with reference to the material strength at this age. Since the lifting process induces bending stresses in the segment, the early-age residual tensile strength of FRC segment plays a vital role. The key design parameters for this load case are early-age residual tensile strength and compressive strength (ACI 544.7R, 2016).

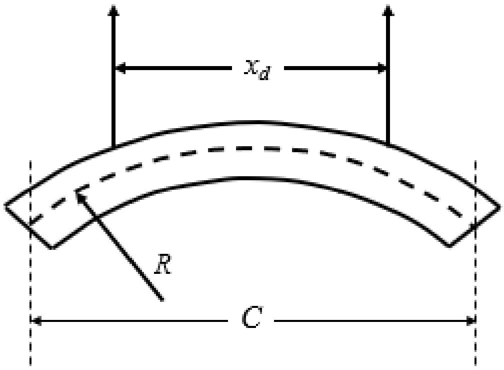

Figure 6.3 Loading condition during demoulding phase

The bending moment developed in a segment during demoulding phase is given as:

$$M_1 = \frac{q_w b(C - x_d)^2}{8} \tag{5.7}$$

where C is the chord length of the segment, q_w is the unit linear weight of a segment and x_d is the lifting point spacing (Figure 6.3). The rate effect and fatigue models are considered irrelevant for this loading case, as the demoulding of segments does not involve neither sudden static loading nor fatigue loading.

6.3.2 Load Case 2: Stacking

In the stacking yard, the demoulded segments belonging to a full ring are stacked one above the other. Wooden blocks are placed in between each segment and at the ground level for support and the blocks are separated by a distance 'x'. In practice, some eccentricity occurs between the upper and lower stack supports (y), which can act toward either side of the wooden blocks. For calculating the maximum bending moment developed during stacking, the bending moment due to self-weight of bottom segment, the self-weight of segments above (W_{n-1}) and the eccentricity of the upper stack support should be considered. The bottom-most segment, in addition to self-weight of above segments, must withstand impact loading caused during the stacking of other segments. The application of load on the bottommost segment might vary from sudden to gradual loading and hence, the variation of load carrying capacity of the tunnel segments under those loading conditions needs to be investigated.

Figure 6.4 Loading condition during the stacking phase (ACI 544.7R, 2016)

The bending moment due to the self-weight of the bottom segment, M_b and due to the self-weight of segment above, M_{n-1}, is given as:

$$M_b = q_w w\left(\frac{x^2}{8} - \frac{(C-x)^2}{2}\right) \tag{5.8}$$

$$M_{n-1} = \frac{q_w \pi R(n-1)e}{n} \tag{5.9}$$

where x is the spacing between the supports and e is the eccentricity.

Thus, the maximum moment at the mid-span of the bottom segment is given as:

$$M_2 = M_b + M_{n-1} \tag{5.10}$$

The bending moment developed in the above two load cases (demoulding and stacking) can be checked for the section capacity by performing nonlinear analysis using finite element method, as detailed in the subsequent section.

6.3.3 Flexural load carrying capacity of the segment

During manufacture and transportation, the loads acting on the segment result in a significant bending moment with no axial forces. Since the tunnel segments at this stage are subjected to pure flexural load, the flexural load carrying capacity of the section is assessed using finite element programme, TNO DIANA v9. If the load carrying capacity is less than the design load, then the assumed segment thickness is adequate. The assumed cross-section of the FRC tunnel segment with steel rebars is modelled in 2D, and the load carrying capacity of the segment under bending is determined by performing a nonlinear static analysis using the displacement-control method. The input for the material model for FRC in tension is determined from the inverse analysis of experimentally obtained flexural test data (6h and 28 days); while the data for compression model is derived directly from the compression test.

As an example, numerical analysis for the Barcelona Metro Line 9 tunnel segment, reinforced with both steel fibres and rebars (as described in Gettu et al., 2004) is performed using the TNO DIANA v9.0 programme. The tunnel has a diameter of 12 m and is made of 7 segments with a length of 4.7 m and one key segment of half that length. The thickness of the tunnel segment is 350 mm. The cross section of the tunnel segment is modelled as 2D solid with tetrahedral elements of size 50 mm. The reinforcement is modelled as 1D element placed at both top and bottom of the segment. The tensile stress-crack opening curve is derived from the inverse analysis of flexural test results of FRC reinforced with 30 kg/m^3 of steel fibres (published in Gettu et al., 2004), from which the tensile stress-strain curve (Figure 6.6a) is obtained by dividing the crack opening by the element size (i.e., crack opening/50). The tunnel segment is simply supported, and the load is applied at the centre of the span to find its flexural load carrying capacity (Figure 6.5).

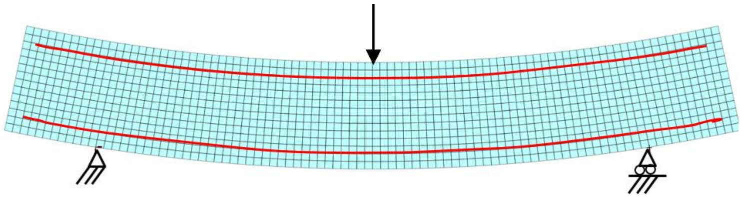

Figure 6.5 Finite element model of tunnel lining segment used for numerical analysis

Nonlinear static analysis is performed under displacement control until a load-point deflection of 15 mm and the load carrying capacity vs. load-point displacement are plotted from the simulation. The experimental (Gettu et al., 2004) and numerical (Plizzari and Cominoli, 2005) results for the Barcelona Metro tunnel segment are used for the validation of the finite element model. Since good agreement between the numerical and experimental results is observed (Figure 6.6b), this 2D model will be utilized for further demonstration.

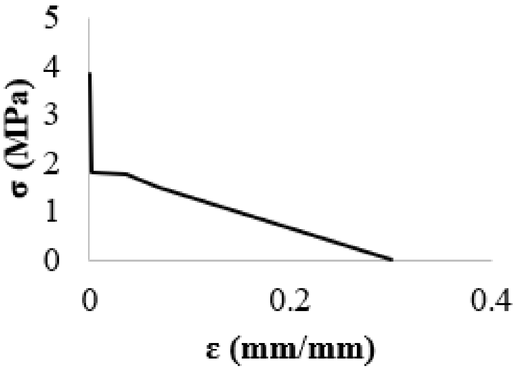

a)

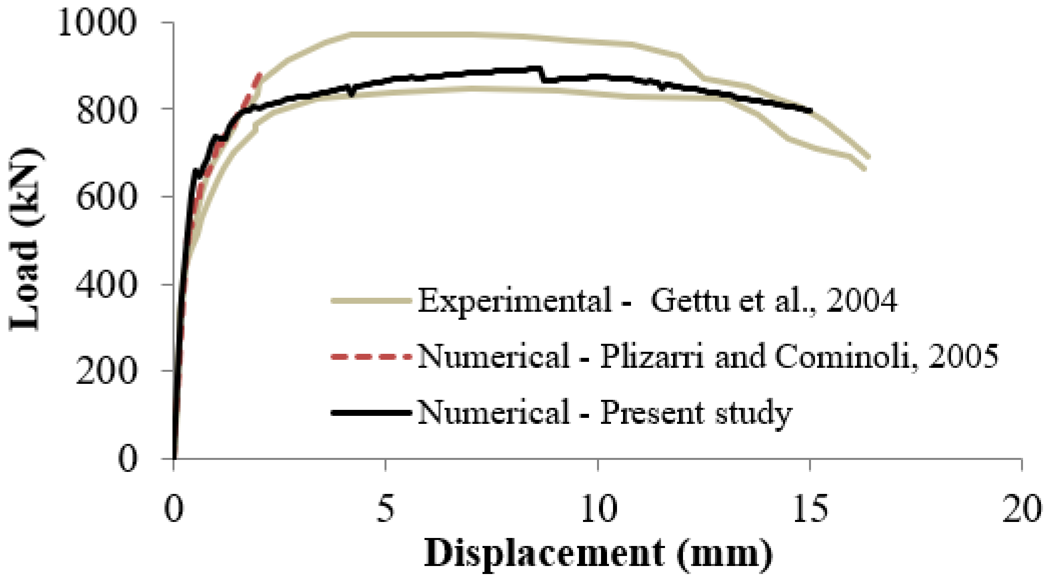

b)

Figure 6.6 a) FRC tensile model obtained from inverse analysis and b) flexural load carrying capacity of Barcelona tunnel segment

After fabrication, these segments are demoulded and placed in the stacking yard one above the other. The bottom-most segment must support the self-weight of above segments and impact loading caused during stacking of other segments. The application of load on the bottom-most segment might vary from sudden to gradual loading and hence, the variation of the load carrying capacity of the tunnel segments under those loading conditions are investigated. The numerical analysis is performed using the tensile material model of the FRCs for which the rate effect model was formulated (Chapter 4 Section 4.5). The compressive material model for the corresponding FRC is derived from the uniaxial compressive test (see Appendix B). In Figure 6.7, the effect of loading rate on the load carrying capacity of the segment with different FRCs is shown, and in the inset, the tensile stress-strain curves for the corresponding loading rates are given. The first peak load decreases by about 33% for M40SF3.75, 27% for M40SF10, 20% for M40SF30 and 10% for M40SF45. With further crack propagation, say at 2 mm deflection, the load carrying capacity decreases by about 25% for both M40PF3.75 and M40SF10, and 10% for concrete with higher dosage of steel fibres. It can be seen that the effect of loading rate on the load capacity of the tunnel segment significantly reduces with the incorporation of higher dosages of steel fibres.

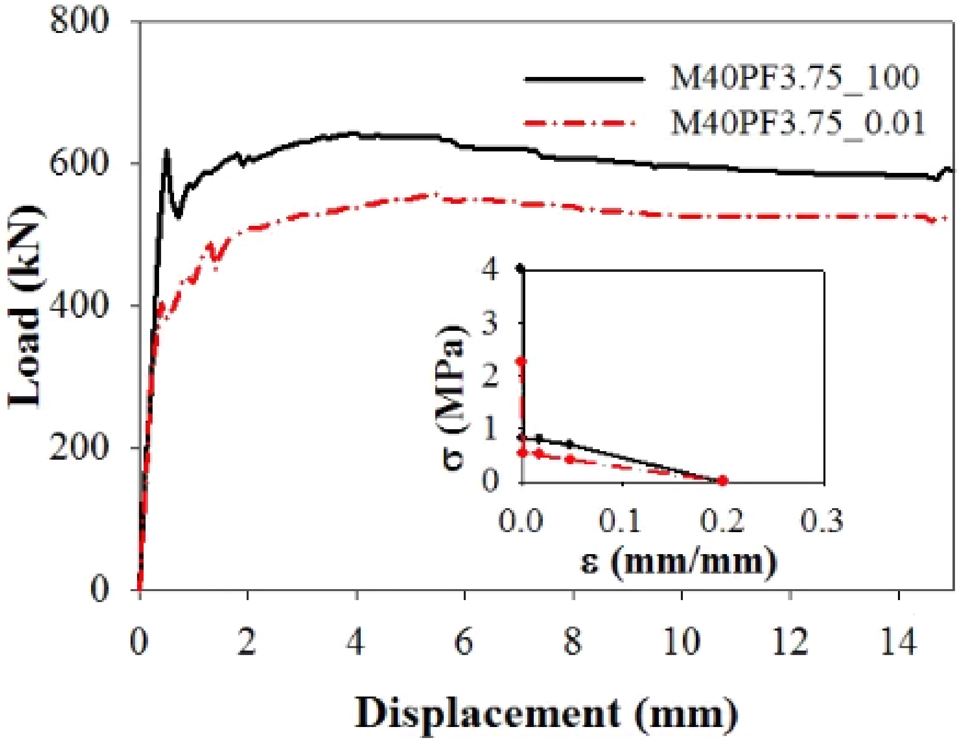

M40PF3.75_100
M40PF3.75_0.01
Load (kN)
Displacement (mm)
800
600
400
200
0
0
2
4
6
8
10
12
14
σ (MPa)
ε (mm/mm)
4
3
2
1
0
0.0
0.1
0.2
0.3

a)

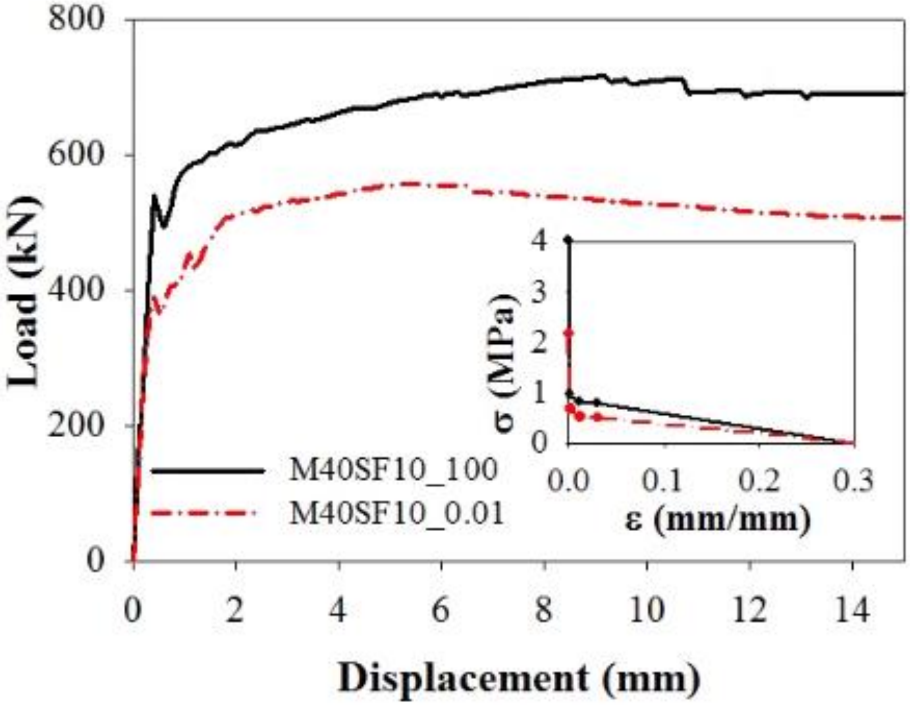

M40SF10_100
M40SF10_0.01
Load (kN)
Displacement (mm)
800
600
400
200
0
0
2
4
6
8
10
12
14
σ (MPa)
ε (mm/mm)
4
3
2
1
0
0.0
0.1
0.2
0.3

b)

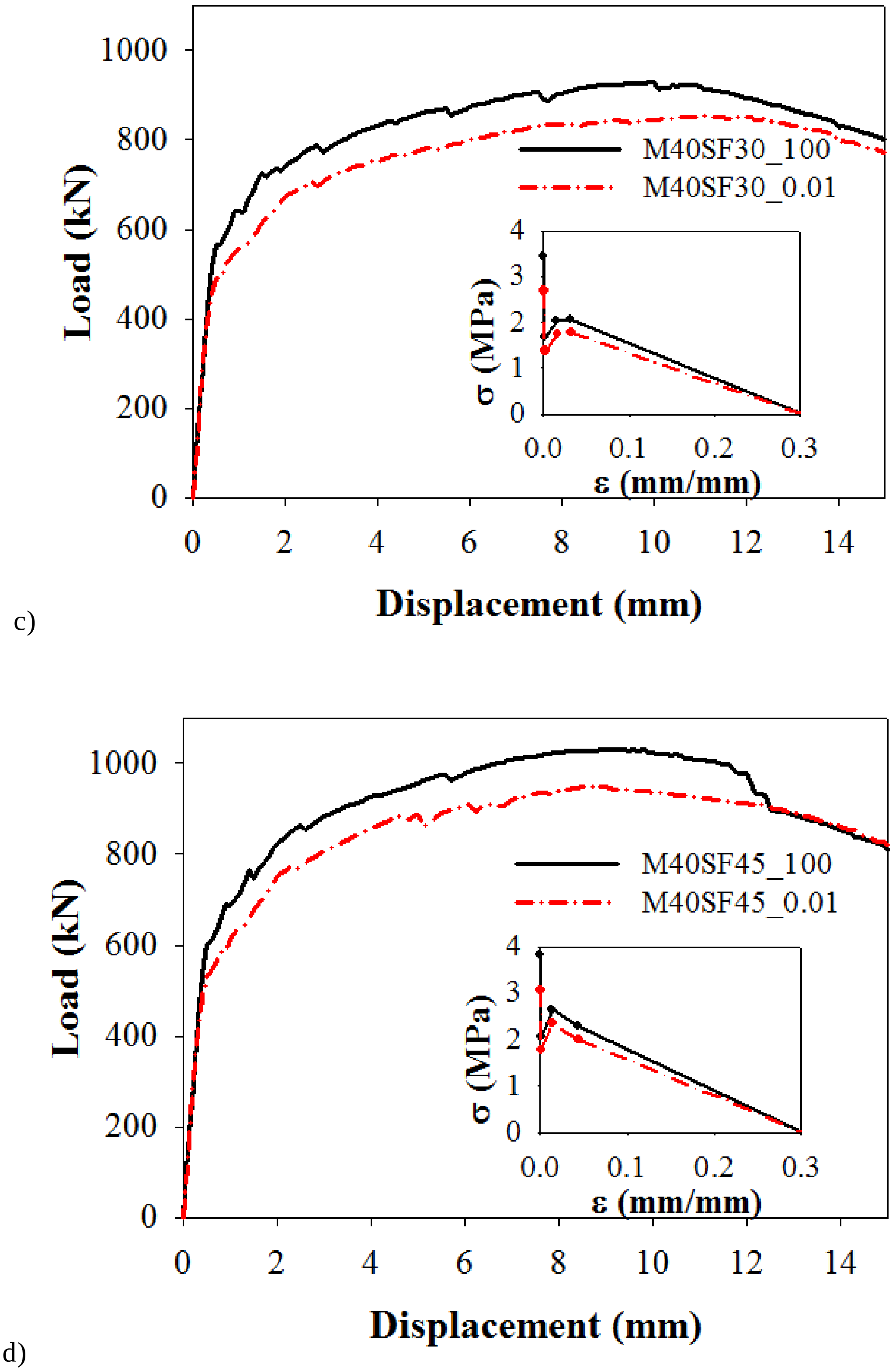

Figure 6.7 Effect of loading rate on the load-carrying capacity of the tunnel segment with different dosages of steel fibre

6.3.4 Load Case 3: Construction stage

Once the desired strength of the concrete is reached, the segments are transported to the construction site. The tunnel boring machine (TBM) advances by thrusting pressure on the recently installed segments due to which the bursting and spalling tensile stresses are developed on the tunnel segment. According to ACI 318-11 (2011), the bursting stresses in the radial direction are expressed as:

$$\sigma_{burst} = \frac{0.25P_{pu}\left(1-\frac{h_{anc}}{h}\right)}{\phi d_{burst}};\ d_{burst} = 0.5(h-2e_{anc}) \tag{5.11}$$

and the bursting stresses in tangential direction as

$$\sigma_{burst} = \frac{0.25P_{pu}\left(1-\frac{a_l}{a_l-2e}\right)}{\phi d_{burst}};\ d_{burst} = 0.5(a_l-2e) \tag{5.12}$$

where P_{pu} is the factored jacking force applied on jack pad, h_{anc} is the length of contact zone between jack shoes and the segment face, h is the depth of cross section, and e_{anc} is the eccentricity of jack pads with respect to the centroid of cross section (Figure 6.8). If these stresses are less than the residual tensile strength of the material, then the design is safe. The residual tensile strength at any crack opening can be obtained from the tensile stress-crack opening curve from the inverse analysis. In this case, the check is performed with σ_1 (refer Section 3.3.2). Since the rate-effect and fatigue model are irrelevant at this phase, the design check does not include any modification.

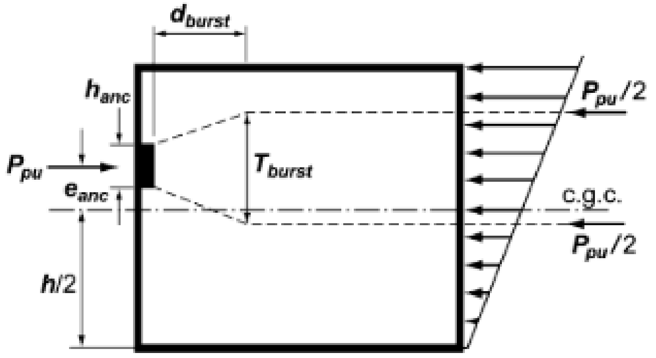

Figure 6.8 Loading conditions during construction stage (ACI 544.7R, 2016)

6.3.5 Load Case 4: Service stage

In the service stage, long-term loads such as soil, groundwater and surcharges exert pressure on the tunnel segments. In addition to axial force and bending moment, hoop stresses are developed, which are transferred along the longitudinal joints between the segments and develop bursting tensile stresses in the segment. The pressure exerted by the soil on the segmental linings is provided by the geotechnical analysis, in terms of axial forces and bending moments using Table 6.2 (refer Figure 6.9). The design check is carried out by drawing the P-M interaction diagram for the segment obtained through translational and rotational equilibrium conditions. The design condition is verified if the axial force and bending moment lie inside or on the border of the interaction diagram.

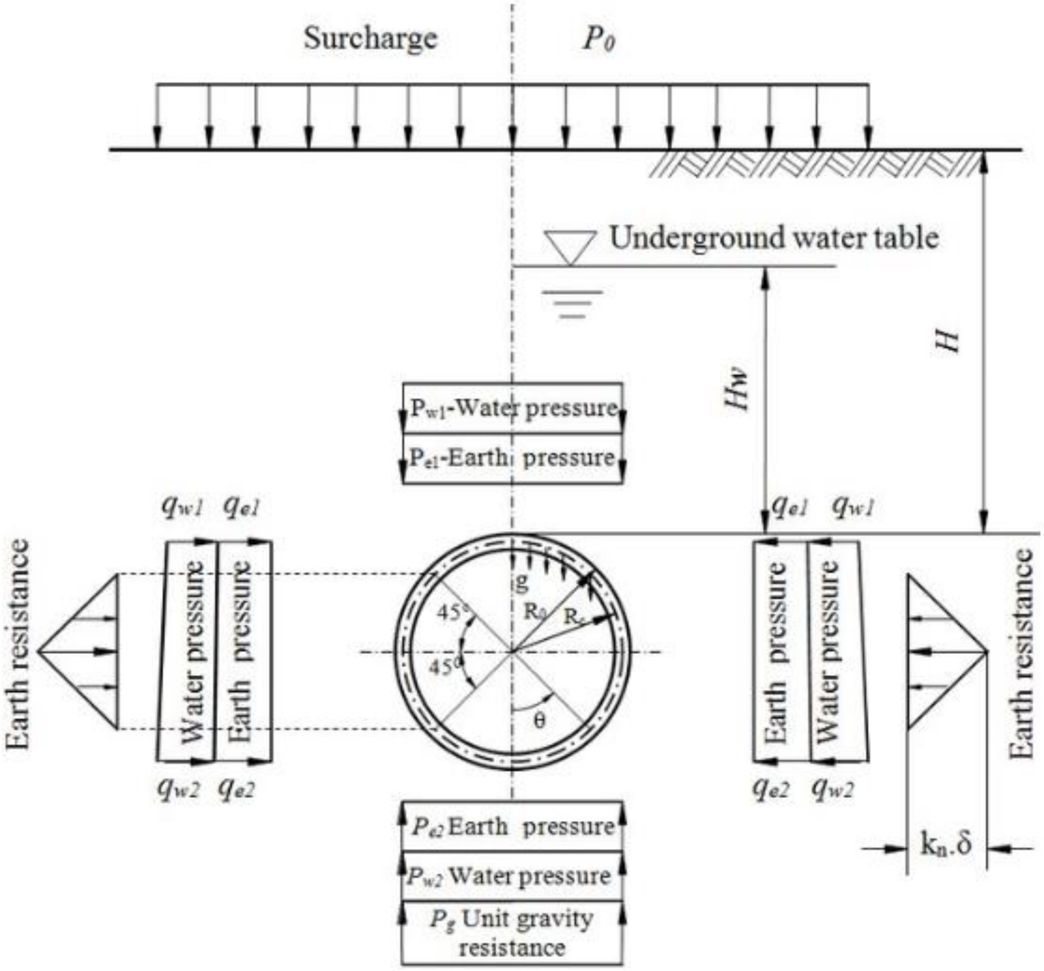

Figure 6.9 Loading conditions for tunnel segment under service (ITA, 2000)

Table 6.2 Equations to compute member forces and moments under service load (ITA Report, 2016)

Load	Bending Moment	Axial Force	Shear Force
Vertical Load $(P = p_{e1}+p_{w1})$	$(1-2S2)\times P\times R_c^2/4$	$S2\times R_c\times P$	$-SC\times R_c\times P$
Horizontal Load $(Q=q_{e1}+q_{w1})$	$(1-2C2)\times Q\times R_c^2/4$	$C2\times R_c\times Q$	$-SC\times R_c\times Q$
Horizontal Triangular Load $(Q'=q_{e2}+q_{w2}-q_{e1}-q_{w1})$	$(6-3C-12C2+4C3)\times Q'\times R_c^2/48$	$(C+8C2-4C3)\times Q'\times R_c/16$	$(S+8SC-4SC2)\times Q'\times R_c/16$
Soil Reaction $(P_k=k\delta_n)$	$0\leq\theta\leq\pi/4$ $(0.2346-0.3536C)\times R_c^2\times k\delta$ $\pi/4\leq\theta\leq\pi$ $(-0.3487+0.5S2+0.2357C3)\times R_c^2\times k\delta$	$0\leq\theta\leq\pi/4$ $0.3536C\times R_c\times k\delta$ $\pi/4\leq\theta\leq\pi$ $(-0.7071C+C2+0.7071S2C)\times R_c\times k\delta$	$0\leq\theta\leq\pi/4$ $0.3536S\times R_c\times k\delta$ $\pi/4\leq\theta\leq\pi$ $(SC-0.7071C2S)\times R_c\times k\delta$
Dead Load $(P_g=\pi g)$	$0\leq\theta\leq\pi/2$ $(3/8\pi-\theta\times S-5/6C)R_c^2\times g$ $\pi/2\leq\theta\leq\pi$ $[-\pi/8+\pi-\theta)S-5/6C-1/2\pi\times S2]\times R_c^2\times g$	$0\leq\theta\leq\pi/2$ $(\theta\times S-1/6C)\times R_c\times g$ $\pi/2\leq\theta\leq\pi$ $(-\pi\times S+\theta\times S+\pi\times S2-1/6C)\times R_c\times g$	$0\leq\theta\leq\pi/2$ $(\theta\times C-1/6S)\times R_c\times g$ $\pi/2\leq\theta\leq\pi$ $[-(\pi-\theta)\times C+\theta\times S+\pi\times SC-1/6S]\times R_c\times g$
Horizontal Deformation at Spring Line (δ_n)	$\delta_n=[(2P-Q')+\pi\times g]\times R_c^4/[24\times(EI/h+0.045k\times R_c^4]$		

θ=angle from crown, $S=\sin\theta$, $S2=\sin^2\theta$, $S3=\sin^3\theta$, $C=\cos\theta$, $C2=\cos^2\theta$, $C3=\cos^3\theta$

6.3.6 P-M interaction diagram for the segment

An interaction diagram can be developed for a segment with known cross section and material properties, to be used for design checks under different loading cases. Yao et al. (2018) implemented a closed-formed solution for a hybrid reinforced tunnel segment to construct the interaction diagram in a spreadsheet. The behaviour of FRC is simulated there by the stress and strain diagrams shown in Figure 6.10 a) and b) for tension and compression, respectively. The response of the steel rebars is simulated using Figure 6.10 c.

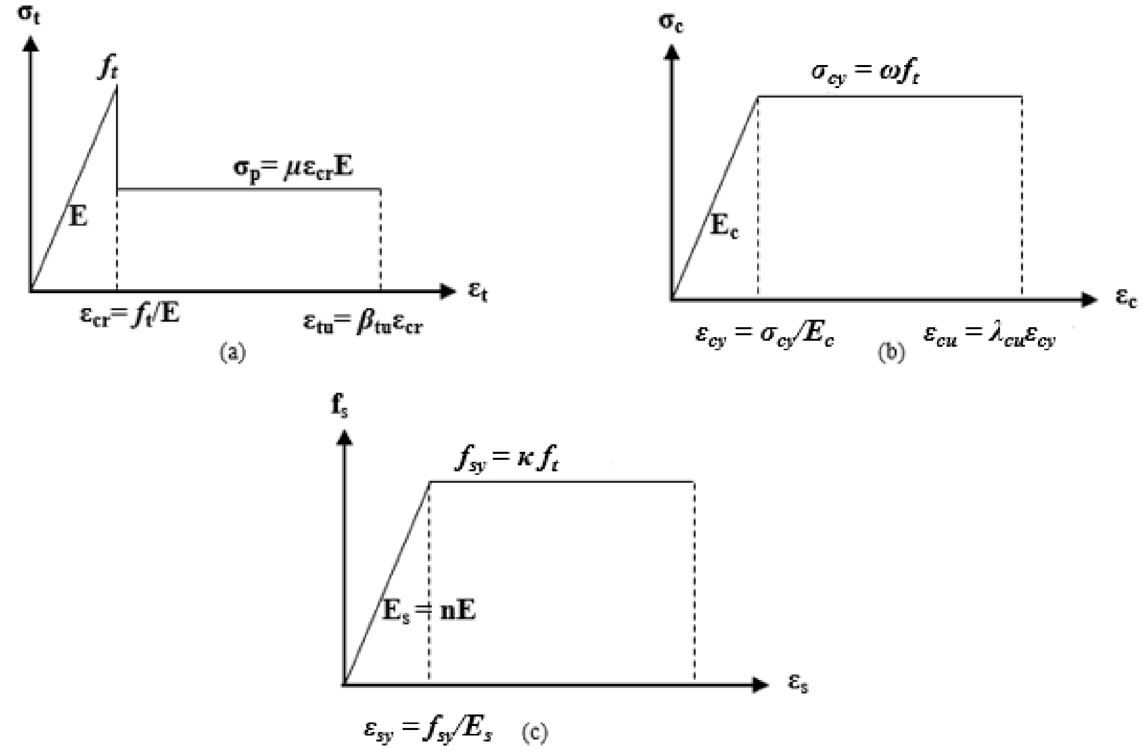

Figure 6.10 Material models for a) SFRC in tension, b) SFRC in compression and c) steel bars in tension (Yao et al., 2018)

The following assumptions are adopted for the development of the closed-formed design formulation (Yao et al., 2018):

- Young's modulus for compression and tension are equal ($E_c = E_t = E$), which can be derived from the inverse analysis of the flexural test.
- Tension model consists of a linear stress-strain diagram up to tensile strength f_t, followed by a post-cracking constant residual tensile stress, $\sigma_1 = \sigma_p = \mu f_t = \mu E\varepsilon_{cr}$, with parameter μ ($0 \leq \mu < 1$) representing the residual tensile strength parameter as a fraction of the tensile strength and ε_{cr} representing tensile cracking strain (f_t/E). The tensile stress-strain curve derived from inverse analysis is assumed to be bilinear and the curve is assumed to be horizontal after σ_1, which is the residual strength at which the fibres start to bridge the crack (refer the Section 4.4.2). The ultimate tensile strain is assumed as 25%, as per RILEM TC 162-TDF (2003), for steel fibre reinforced concrete additionally reinforced with bars. For plain concrete, μ will be taken as 0.

- Compressive behaviour is simulated by an elastic perfectly-plastic model, with a linear stress-strain diagram up to the yield compressive strength σ_{cy} = = ωf_t with parameter ω (ω >1). When the compressive strain is above the yield strain, the stress is maintained constant up to concrete crushing ($\varepsilon_c = \varepsilon_{cu}$). The ultimate compressive strain, ε_{cu}, is assumed to be 3.5% (RILEM TC 162-TDF, 2003). The normalized yield compressive strength ω is the compressive-tensile strength ratio. The compression and tension models terminate at the normalized ultimate compressive strain λ_{cu} and tensile strain β_{tu}, respectively.
- For steel rebars, the tensile model is assumed as elastic perfectly-plastic, with a linear stress-strain diagram up to yield tensile strength of rebar, $f_{sy} = \kappa f_t$, where, κ is the normalized yield tensile strength, which is the ratio between the yield tensile strength of steel rebar and the tensile strength of concrete. The tensile yield strain of steel is taken as, $\varepsilon_{sy} = f_{sy} E_s$, where E_s is Young's modulus of concrete. When the tensile strain of rebar is above the yield tensile strain, the stress maintained constant.

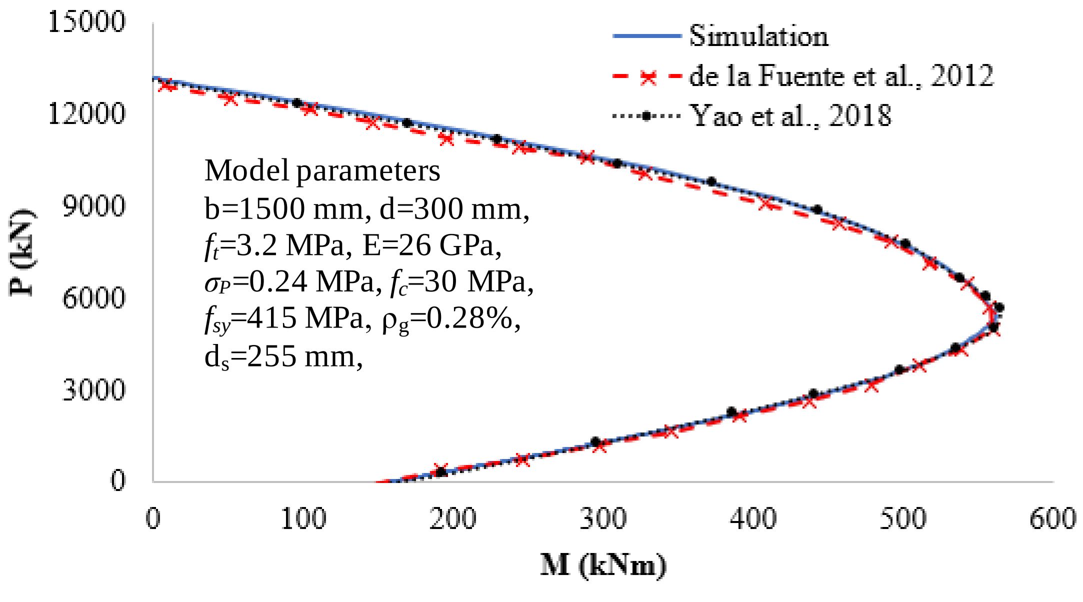

Figure 6.11 Moment interaction diagram for the reinforced concrete tunnel segment

Using the material model, the P-M interaction diagram is derived at different phases of crack propagation in the tunnel segment. An example from Yao et al. (2018), Terrassa tunnel segment, which is taken for illustration, agrees with the simulation by other investigators as well. For FRC, the parameters involved in the tensile model for FRC is derived from the work of de la Fuente et al. (2012), i.e., the peak flexural strength and residual flexural strength values govern the shape of the tensile stress-strain curve. However, in this case, the tensile stress-strain curve is derived from inverse analysis of flexural test data.

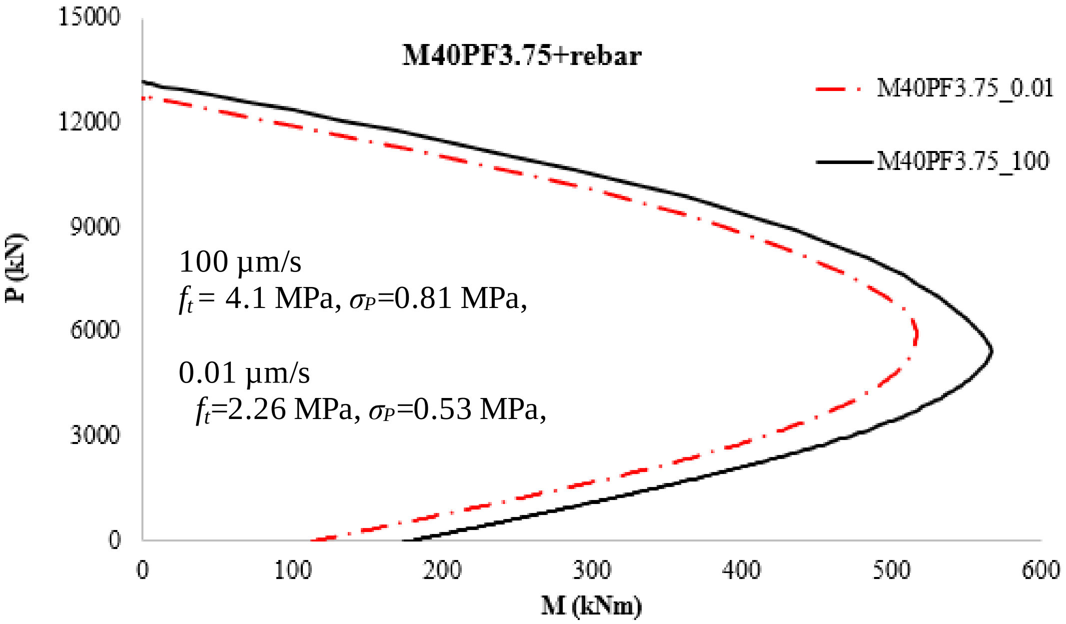

a)

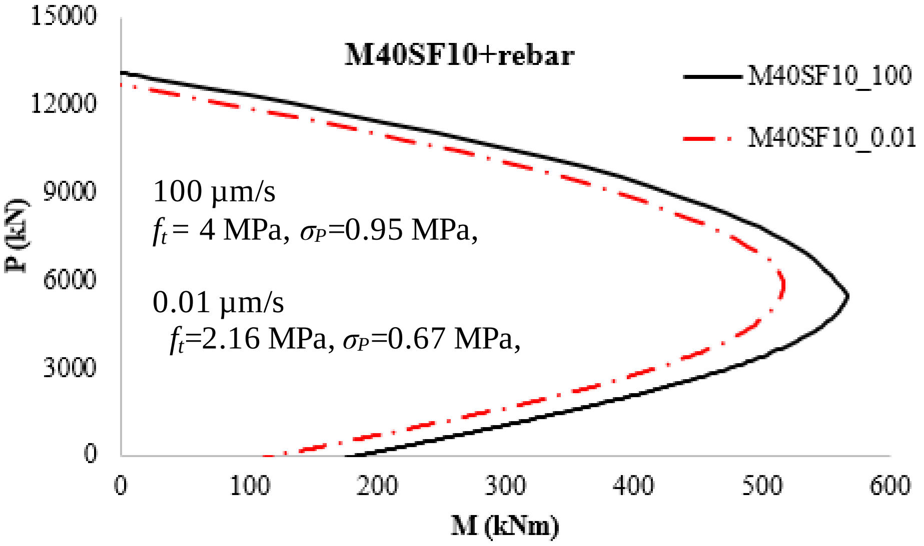

b)

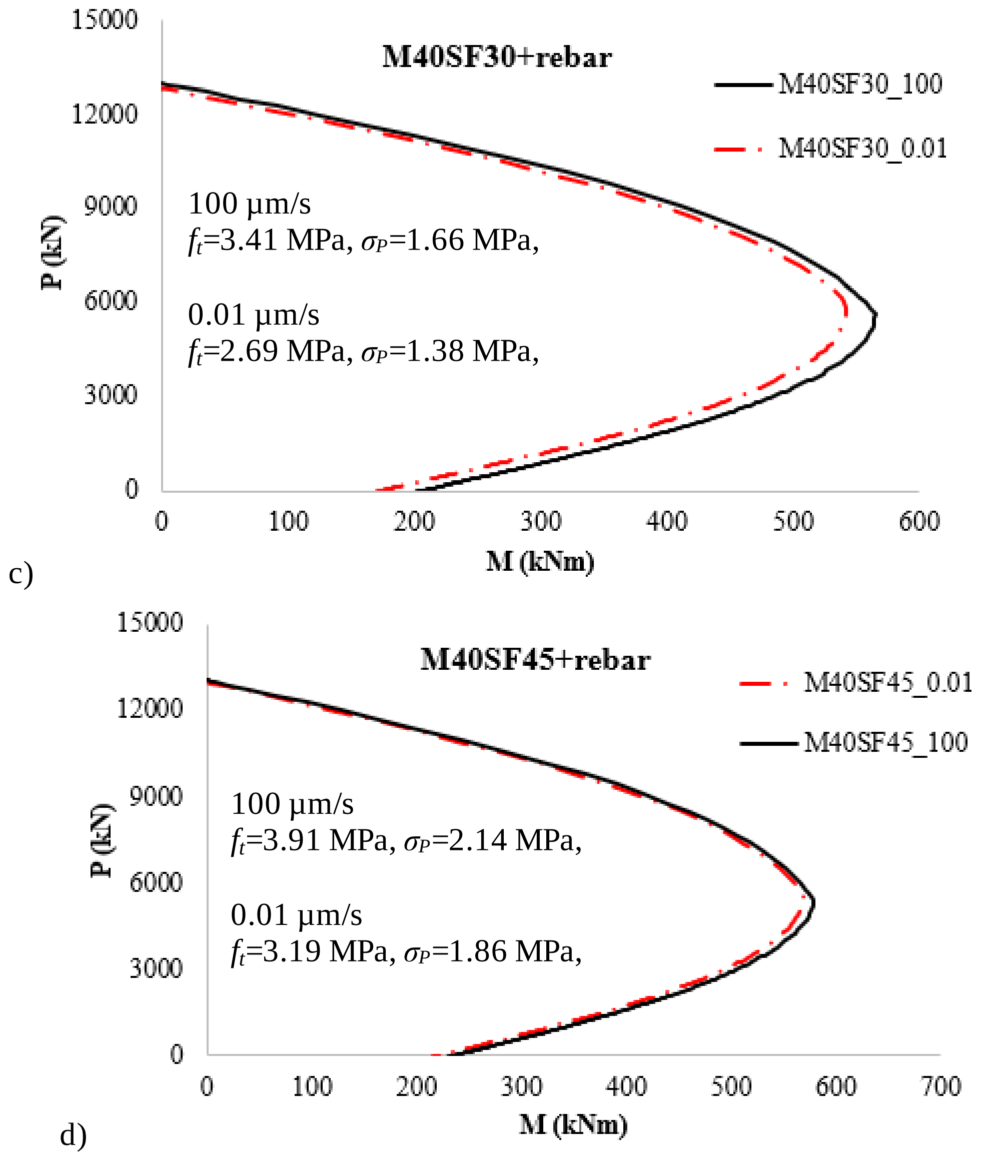

Figure 6.12 Load rate effects on moment-force interaction diagram for tunnel segment under service load condition

Since the design in this phase is based on the P-M (moment-force) interaction diagram, the rate-effect model is utilized to determine the time-dependent fracture properties required to derive the interaction diagram for the Terrassa tunnel segment (Figure 6.12). It is found that the incorporation of PF and lesser dosage of SF have a greater impact on the rate-sensitivity of the segment moment carrying capacity. For instance, at zero axial force, the moment carrying capacity reduces by 40% for M40PF3.75 and M40SF10, and less than 10% for higher dosage of steel fibres, when the loading rate is changed from 100 µm/s to 0.01 µm/s. The rate sensitivity of maximum moment carrying capacity is 15% for polymer fibre reinforced concrete and lower dosage of steel fibres, and less than 10% for higher dosage of steel fibres. When the dosage of SF is increased to 45 kg/m^3, there is no significant difference observed at different loading rates. So, for a tunnel segment reinforced with polymer fibres and low dosage of steel fibres, it appears mandatory to include rate effects in the derivation of the interaction diagram.

Further, if the tunnel is designated for traffic movement, then the tensile properties of FRC used in the design must be modified using fatigue reduction factors. In this approach, X is used as reduction factor for the tensile strength of concrete (Xf_t) and Y is used as the reduction factor for the bridging strength ($Y\sigma_p$), and the interaction diagram at different fatigue cycles is obtained (Figure 6.13). At zero axial force, the moment carrying capacity of the FRC segment considering fatigue loading is about 35% lower than that without considering fatigue loading. However, the maximum moment carrying capacity is reduced by about 10% lower for segments that designed for fatigue. It appers that the fatigue design is crucial, when the segment is subjected to pure bending.

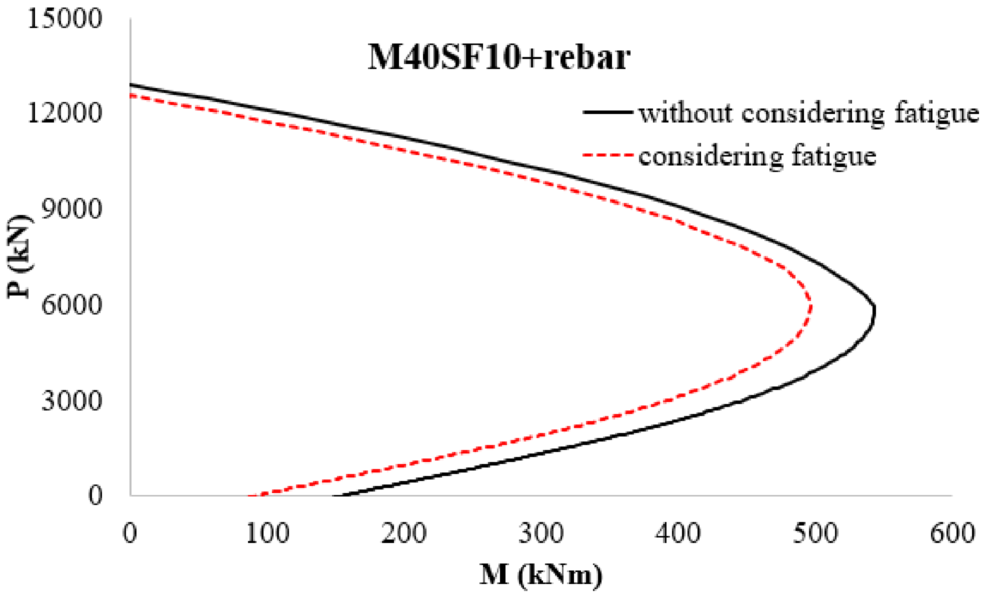

a)

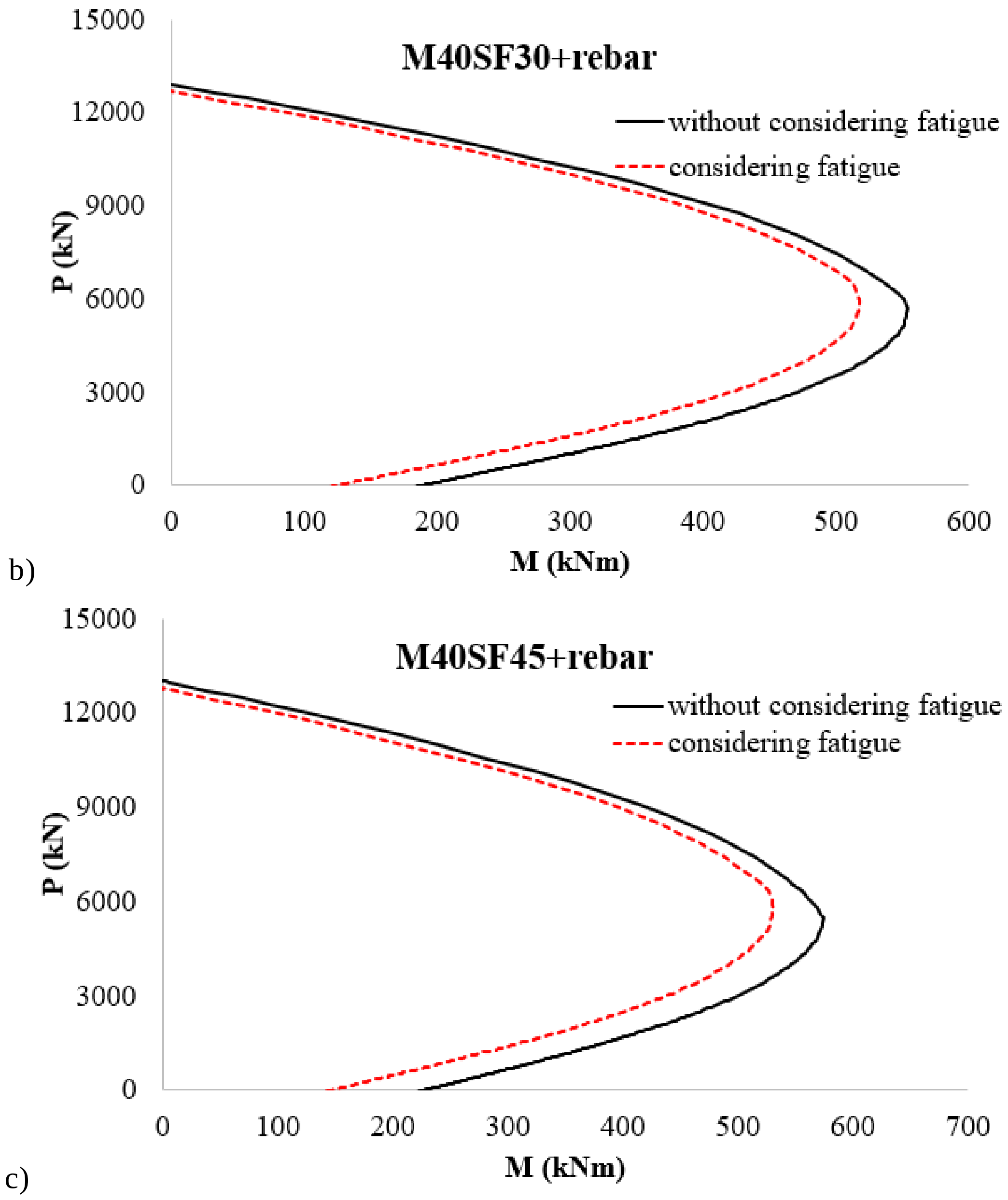

Figure 6.13 Variation of moment-force interaction diagram of tunnel segment with fatigue cycles

6.4 DESIGN OF PAVEMENTS AND SLABS-ON-GRADE

Concrete pavements are usually used in places with heavy traffic movements and the most probable failure condition is associated to fatigue loading. Failure at fatigue might occur at stress levels that are much lower than the capacity of the material, which is the governing factor in design. The adoption of fibre reinforced concrete (FRC), having better performance with respect to resistance to cracking, allows less conservative design than with plain concrete. In India, FRC pavements are designed for fatigue using IRC:SP:46 (2013), which is based on the pre-peak fatigue resistance of FRC. In some industrial slabs-on grade, a similar procedure is used when there is fatigue loading due to fork-lifts and loaders. Since the design parameters include both pre-peak and post-peak strength parameters, the fatigue-based design must include the reduction factors X and Y (from Figure 6.1). However, the drawback identified in these types of design is that the fatigue damage analysis is done using elastic stresses.

Nayar (2015) proposed a design guideline based on the performance of cracked concrete considering the effectiveness of the fibres in the post-peak region and using inelastic analysis for the fatigue design. Thus, the moment carrying capacity of the FRC pavements under fatigue loading is given by the equation:

$$M_{all} = M_n + M_p = \left(X \frac{f_{ct,k}}{\gamma_c} + Y \frac{f_{e,150k}}{\gamma_c} \right) \frac{h^2}{6} \tag{5.13}$$

where X and Y are the reduction factors (derived as illustrated in Figure 6.1) for the pre-peak (f_{ctk}) and post-peak strength ($f_{e,150k}$) parameter. $f_{e,150k}$ is the characteristic equivalent flexural strength of FRC up to a deflection of span/150, f_{ctk} is the characteristic flexural strength of the FRC and h is the thickness of the slab. For a pavement of thickness 265 mm reinforced with hooked-ended cold-drawn steel fibres of 10, 30 and 45 kg/m^3 in M35 grade concrete, the variation of moment carrying capacity at 2 million fatigue cycles is determined (Table 6.3). When the fatigue models are used, the moment carrying capacity decreases by about 50% and 40% for concrete with low (M40SF10) and high dosages of steel fibres (M40SF30 and M40SF45), respectively.

Table 6.3 Moment carrying capacity after incorporating the fatigue model

N	**f_{ctk}* (MPa)**	**f_{e150k}* (MPa)**	**M_{all} (kNmm/mm) at 2 million fatigue cycles**	
			without fatigue consideration	**with fatigue consideration**
M40SF10	3.85	1.56	63.3	31.4
M40SF30	3.60	2.78	74.6	45.7
M40SF45	3.95	3.45	86.6	52.5

*static flexural strength data from Nayar (2015)

6.5 DESIGN OF ELEVATED SLABS

Elevated slabs are used in factories, warehouses and basements where the area underneath the slab is not considered to give vertical support to the slab. The practice has also been extended to slabs supported by columns in the past 20 years. They are used as floors in multi-storey buildings, with fibres as the primary flexural reinforcement. This section addresses the conventional design procedure of steel fiber-reinforced concrete (SFRC) in flat plates supported on piles or columns. FRC used in industrial applications is subjected to dynamic loads from cranes and heavy forklift loads. Further, it could be subjected to fatigue and long-term loads (ACI 544.6R-15).

In the case of elevated slabs, the design as per ACI 544.6R (2015) is chosen for illustrating the incorporation of time-dependent models. These slabs support heavy racks and they are subjected to vehicle movement. The stacking of racks occurs at varying load rates, which necessitates the incorporation of a rate-effect model in the design. The vehicle movement causes fatigue loading in the structure, which can be considered by the use of pre-peak and post-peak reduction factors. The bending moment resistance of simply-supported elevated slab is evaluated using the following equation (ACI 544.6R, 2015):

$$M_{all} = \left(\frac{3\omega\mu}{\omega + \mu} \right) \left(\frac{bt^2}{6} \right) f_t \tag{5.14}$$

where, ω represents the ratio of the compressive strength to tensile strength in the concrete matrix and, f_t is the cracking strength in tension. μ is the ductility factor obtained as a fraction of bridging strength parameter with respect to tensile strength, i.e., ratio of σ_p to f_t.

For illustration purpose, a slab of 22500 m^2 with 30×30 m joint-less bay sizes is designed using an M40 grade concrete. The slab is taken to be installed over a grid of 220 mm diameter piles at 3 × 3 m. The moment-carrying capacity of a slab of thickness 300 mm is calculated for different types of concrete, subjected to varying loading rates (Table 6.4). The rate-effect model is used for determining the tensile strength and residual bridging strength at different loading rates. When the dosage of fibres in concrete is increased, the rate sensitivity of moment carrying capacity decreases. For fatigue-based design, the tensile strength is multiplied by the reduction factor X and residual tensile strength by *Y*, and the moment carrying capacity is calculated using the above equation and listed in Table 6.4. It could be seen that, the moment capacity calculated with consideration of fatigue loading is 50% lower than that calculated without fatigue consideration.

Table 6.4 Moment carrying capacity of slab subjected to different loading rates

Concrete	**M_{all} (kNmm/mm) at different loading rate**		**M_{all} (kNmm/mm) at 2 million fatigue cycles**	
	100 μm/s	**0.01 μm/s**	**without fatigue consideration**	**with fatigue consideration**
M40SF10	41.8	29.7	35.7	17.6
M40SF30	71.7	60.0	65.9	33.5
M40SF45	91.4	79.9	85.7	43.7

6.6 CONCLUSIONS

In this chapter, the design methodology to incorporate time-dependent fracture properties has been proposed. The significance of the methodology is discussed in terms of variation of section capacity with loading rate and fatigue loading. The design of tunnel segment, pavements and elevated slabs that utilise the toughness parameter as design input is chosen to briefly explain the proposed design modification. The modification factors are obtained for the rate effect model and fatigue model to alter the design inputs and determine the section capacity. Further,

- The moment carrying capacity of tunnel segment reinforced with polypropylene fibres could be reduced significantly when subjected to long-term loading. With an increase in steel fibre dosage, the long-term effects diminish. Therefore, it is important to incorporate a rate effect model in tunnel segments reinforced with low dosage of steel fibres or polymer fibres.
- The tunnel lining segment reinforced with higher dosage of steel fibres has higher moment carrying capacity even under high fatigue loading. Hence, they are best suited for segments designed for traffic loading.

- The significance of using a fatigue model in the design of pavements is discussed by comparing the moment-carrying capacity, with and without fatigue reduction factors. It could be seen that the moment carrying capacity reduces by about 50% for concrete reinforced with lower dosage of steel fibres, for the case considered here.
- In elevated slabs, the concrete reinforced with polymer fibres show adverse long-term behaviour when compared to that of concrete reinforced with steel fibres.
- Since the design methodology includes both cracked and uncracked fatigue performance, it can be used to effectively improve the serviceability and safety of the structure. Incorporation of higher dosage of steel fibres has generally a beneficial effect on time-dependent fracture properties. Hence, in all types of structures, the FRC with higher dosage of steel fibres showed higher moment-carrying capacity under long-term static and fatigue loading.

7 CONCLUSIONS

7.1 GENERAL CONCLUSIONS

In general, the present work has resulted in the characterization of the fracture response and the development of design guidelines for fibre reinforced concrete elements subjected to different loading rates and fatigue loading. The experimental work comprises two facets in which M40 grade concrete with different dosage of fibres were characterized at different static loading rates and fatigue loading levels. The results were used to develop models, which were later used in the design of FRC elements such as tunnel segments, pavements and elevated slabs. The salient conclusions that correspond to the fulfilment of the principal objectives of this work are given below:

- The R-curve analysis using the flexural test data of both steel and polymer FRC demonstrates the role of fibres in improving the fracture resistance of concrete in various stages of crack propagation. The R-curve method proves to be a simple analysis tool to represent the toughness of FRC.
- The tetralinear cracked hinge model obtained through inverse analysis and the PGSL optimisation algorithm is proven to be an appropriate model for FRC with softening and pseudo-hardening response.
- From the characterization of FRC at different loading rates, it was understood that higher dosages of hooked-ended steel fibres reduce the rate sensitivity of the peak load. The concrete with polypropylene fibres shows higher rate sensitivity when compared to that with same volume fraction of steel fibres.
- The post-peak fatigue characterisation of FRC indicates that the higher dosage of steel fibres is beneficial in structures that are subjected to high fatigue loads. For structures that are subjected to lower fatigue loads, even low dosage of steel fibres significantly improves the fatigue performance.
- The design methodology developed for FRC tunnel segments addresses different loading conditions that could cause creep and fatigue damage in the structure. The moment-interaction diagram used in design has been

modified based on the rate effect and fatigue models, thereby ensuring the required performance of the tunnel segment throughout the design life.

- The design methodology developed for FRC pavements focuses on the fatigue damage caused due to movement of vehicles. The fatigue model is effectively incorporated in the design equation to account for the post-peak fatigue damage.
- In general, the FRC structural elements designed by incorporating the rate effect model show that the higher dosage of steel fibres significantly has lower rate sensitivity. The rate effect model becomes more critical for structures reinforced with lower dosage of steel fibres.

7.2 SPECIFIC CONCLUSIONS

The specific conclusions derived from the different studies comprising this thesis work are summarised as follows:

7.2.1 R-curve analysis

- The fracture resistance values are consistently higher for concrete with steel fibres than concrete with polymer fibres, for the same volume fractions.

- The R-curves obtained using the EN 14651 have been used satisfactorily to predict the flexural response for other geometry as well. Since the crack progression beyond a crack opening of about 1.5 mm in the EN 14651 specimen is limited by the specimen boundary, it is proposed that toughness characterization be limited to the crack width of 1.5 mm, instead of 3.5 mm. This is expected to provide more representative material characterization without much effect of the specimen dimensions.

7.2.2 Inverse analysis for the σ-w curves

- From the assessment of different models (i.e., bi-, tri- and tetra-linear), it is found that the bilinear model does not represent the hardening response of FRC satisfactorily, with the usage of a weighting function.

- Trilinear and tetralinear models gave satisfactory results for FRCs with both softening and hardening flexural response; although the trilinear model requires a weighting function at the peak load for better fitting. The tetralinear model of the *σ*-*w* curve is found to be robust as it does not involve any weighting functions and is not affected by the choice of the range of the fitting variables.

7.2.3 Rate-dependence of the fracture properties

- The tensile and flexural strength of concrete reduce by 40% for low toughness concrete, when comparing the slowest and fastest loading rates over 5 orders of magnitude. The lowering of the tensile strength can be attributed to the relaxation of stresses near the crack tip, which leads to an increase in the FPZ length, as seen in the finite element simulations. The reduction in strength is found to be much lower in concretes with higher dosages of steel fibres.
- The residual flexural strength (or toughness) of polymer fibre reinforced concrete (PFRC) is found to exhibit higher rate-dependence (i.e., 40% reduction from the fastest to slowest loading rate) compared to steel fibre reinforced concrete (i.e., 20% decrease). This could be a consequence of fibre creep and weakening of the fibre-matrix interface in PFRC at slower crack rates. FRC with the highest dosage of steel fibres, showed the least rate-dependence with only about 10% lower residual strength from fastest to slowest loading rate. Higher dosages of steel fibres in concrete seem to be beneficial for structures subjected to different loading rates.
- The analytical results from the inverse analysis of flexural test data allowed to obtain the rate-dependent model for predicting the tensile strength and cohesive stresses developed during crack propagation at different loading rates.
- The *σ*-*w* curve for different loading rates seem to be modelled well using the proposed model based on the *σ*-*w* curve at the standard rate for the corresponding FRC and the rate-dependence of the tensile strength. The resulting *σ*-*w* curve can be conveniently used in the numerical analysis to predict the structural response at different loading rates.

7.2.4 Post-peak fatigue behaviour of cracked FRC

- The *S-N* diagram of the fatigue data shows wide scatter, which is common in concrete; however, with an increase in dosage of fibres, the scatter decreases.
- The fatigue life of concrete subjected to high fatigue loads can be improved significantly by the incorporation of fibres. Higher dosages of fibres are best suited for structures that experience higher magnitude of fatigue stresses.
- At lower fatigue loads, higher fibre dosages do not have any significance. This is because of the lower energy supplied to the specimen and lower crack widths during cyclic loading does not further increase the length of FPZ. Only some of the fibres that are already present in the FPZ will help in resisting the fatigue damage.
- Even though the fatigue performance of concrete with lower dosage of steel fibres is poorer than that of high dosage of steel fibres, adding a low dosage of steel fibres can significantly improve the fatigue performance of concrete. Hence, low dosage of steel fibres can be incorporated in structures that are subjected to low fatigue cycles.
- By using the developed model, the fatigue performance of FRC can be designed for. With increased usage of FRC, considering its higher durability and fatigue life, the established model could be suitable for the design of pavements and other structures.
- Using the *S-N* model based on the critical CMOD in design, the safety of the structure can be further improved because the crack growth is prevented from becoming unstable under fatigue.

7.2.5 Incorporation of time-dependent fracture properties in the structural design

- The moment carrying capacity of tunnel segment reinforced with polypropylene fibres could be reduced significantly when subjected to long-term loading. With an increase in steel fibre dosage, the long-term effects diminish. Therefore, it is important to incorporate a rate effect model in tunnel segments reinforced with low dosage of steel fibres or polymer fibres.

- The tunnel lining segment reinforced with higher dosage of steel fibres has higher moment carrying capacity even under high fatigue loading. Hence, they are best suited for segments designed for traffic loading.
- The significance of using a fatigue model in the design of pavements is discussed by comparing the moment-carrying capacity, with and without fatigue reduction factors. It could be seen that the moment carrying capacity reduces by about 50% for concrete reinforced with lower dosage of steel fibres, for the case considered here.
- In elevated slabs, the concrete reinforced with polymer fibres show adverse long-term behaviour when compared to that of concrete reinforced with steel fibres.
- Since the design methodology includes both cracked and uncracked fatigue performance, it can be used to effectively improve the serviceability and safety of the structure. Incorporation of higher dosage of steel fibres has generally a beneficial effect on time-dependent fracture properties. Hence, in all types of structures, the FRC with higher dosage of steel fibres showed higher moment-carrying capacity under long-term static and fatigue loading.

7.3 RECOMMENDATIONS FOR FUTURE WORK

The thesis presents design methodologies for FRC tunnel segments, pavements and elevated slabs with approaches to address the static load rate effects and fatigue load specific to each application. Though the methods are quite comprehensive, further studies would give better understanding through the development of more widely-validated models for design. Some recommendations are as follows:

- An extensive experimental study on the effect of loading rate in FRC of different strengths and different types of fibres is needed to validate the proposed rate effect models and to formulate more efficient models that can be incorporated in the design.
- In the design, the rate effects of conventional rebars in the tunnel segment and elevated slabs were assumed to be negligible. However, structural level testing on fibre reinforced concrete beams with conventional reinforcement

bars can be performed at different loading rates in order to determine the rate-dependence of the hybrid material, steel rebars and fibres in concrete.

- The rate effect model can be used to extrapolate the fracture behaviour of FRC under sustained loading, which can be used as the input for finite element model to predict the creep behaviour of beams. It will also help in further validating the model.
- The rate effect study of compressive behaviour of cracked FRC is to be performed for incorporating rate effects in structures that are subjected to compression loads for prolonged time. For example, the compressive forces between segments in tunnel linings.
- The experimental study on post-peak fatigue performance can be extended to other crack openings, and to various combinations of fibres and grades of concrete. Such a study will further help in formulating more efficient S-N models that can be incorporated in design.
- FRC pavement can be properly instrumented in order to monitor the degradation of residual strength with increase in fatigue cycles. This could help in confirming the developed fatigue models.
- The design of other FRC structural elements that experience time- and rate-dependent damage, especially in structures that experience prolonged static and fatigue loadings, during their service life can be identified and modified using the developed models. Further, the design approach can be validated through structural level testing that would also enable verification of scale effects, if any.

REFERENCES

ACI 318-11, 2011. Building code requirements for reinforced concrete, American Concrete Institute, Farmington Hills, MI. https://doi.org/30 CFR 250.901(d)(1)

ACI 544.6R, 2015. Report on Design and Construction of Steel Fiber-Reinforced Concrete Elevated Slabs. Farmington Hills, MI.

ACI 544.7R, 2016. Report on design and construction of fiber-reinforced precast concrete tunnel segments. American Concrete Institute. Farmington Hills, MI.

Alvaredo, A.M., Torrent, R., 1987. The effect of the shape of the strain-softening diagram on the bearing capacity of concrete beams. Mater. Struct. 20, 448–454. https://doi.org/10.1007/BF02472496

ASTM C1609/C1609M, 2010. Standard Test Method for Flexural Performance of Fiber-Reinforced Concrete (Using Beam With Third-Point Loading).

ASTM E739-10, 2015. Standard practice for statistical analysis of linear or linearized stress-life (S-N) and strain-life (ε-N) fatigue data, American Society for Testing and Materials. https://doi.org/10.1520/E0739-10R15

ASTM STP:313, 1962. Manual on fitting straight lines, American Society for Testing and Materials. https://doi.org/10.1520/stp313-eb

Babafemi, A.J., Boshoff, W.P., 2017. Pull-out response of macro synthetic fibre from concrete matrix: Effect of loading rate and embedment length. Constr. Build. Mater. 135, 590–599. https://doi.org/10.1016/j.conbuildmat.2016.12.160

Babafemi, A.J., du Plessis, A., Boshoff, W.P., 2018. Pull-out creep mechanism of synthetic macro fibres under a sustained load. Constr. Build. Mater. 174, 466–473. https://doi.org/10.1016/j.conbuildmat.2018.04.148

Banjara, N.K., Ramanjaneyulu, K., 2018. Experimental Investigations and Numerical Simulations on the Flexural Fatigue Behavior of Plain and Fiber-Reinforced Concrete. J. Mater. Civ. Eng. 30, 1–15. https://doi.org/10.1061/(ASCE)MT.1943-5533.0002351.

Banthia, N., 1990. A study of some factors affecting the fiber-matrix bond in steel fiber reinforced concrete. Can. J. Civ. Eng. 17, 610–620. https://doi.org/10.1016/j.cemconres.2014.05.008

Banthia, N., Sheng, J., 1996. Fracture Toughness of Micro-Fiber Reinforced Cement Composites. Cem. Concr. Compos. 18, 251–269.

Barragán, B.E., 2002. Failure and toughness of steel fiber reinforced concrete. Universitat Politècnica de Catalunya. https://doi.org/10.1017/CBO9781107415324.004

Barragán, B.E., Gettu, R., Martín, M.A., Zerbino, R.L., 2003. Uniaxial tension test for steel fibre reinforced concrete—a parametric study. Cem. Concr. Compos. 25, 767–777. https://doi.org/http://dx.doi.org/10.1016/S0958-9465(02)00096-3

Barros, J.A.O., Cunha, V.M.C.F., Ribeiro, A.F., Antunes, J.A.B., 2005. Post-cracking behaviour of steel fibre reinforced concrete. Mater. Struct. 38, 47–56. https://doi.org/10.1007/BF02480574

Batson, B.G., Ball, C., Bailey, L., Landers, E., Hooks, J., 1972. Flexural Fatigue Strength of Steel Fiber Reinforced Concrete Beams. ACI J. 673–677.

Bažant, Z.P., Gettu, R., 1992. Rate effects and load relaxation in static fracture of concrete. ACI Mater. J. 89, 457–468. https://doi.org/10.14359/2400

Bažant, Z.P., Gettu, R., Kazemi, M.T., 1991. Identification of nonlinear fracture properties from size effect tests and structural analysis based on geometry-dependent R-curves. Int. J. rock Mech. Min. Sci. Geomech. Abstr. 28, 43–51.

Bažant, Z.P., Kim, J.-K., Pfeiffer, P.A., 1986. Nonlinear fracture properties from size effect tests. J. Struct. Eng. 112, 289–307.

Bernad, C., Gettu, R., Barragan, B.E., Antunes, J.L., 2002. Study of the effect of loading rate and relaxation on the behaviour of steel fibre reinforced concrete, in: Report of Tests Performed within Sub-Task 5.2 Creep in the Post- Cracked Region: Brite Project (BRPR.CT98.0813).

Brake, N.A., 2012. The characterization of a plain concrete equivalent elastic fatigue crack resistance curve under various loading regimes, Ph.D. thesis. Michigan State University.

Buratti, N., Ferracuti, B., Savoia, M., 2013. Concrete crack reduction in tunnel linings by steel fibre-reinforced concretes. Constr. Build. Mater. 44, 249–259. https://doi.org/10.1016/j.conbuildmat.2013.02.063

Buratti, N., Mazzotti, C., Savoia, M., 2011. Post-cracking behaviour of steel and macro-synthetic fibre-reinforced concretes. Constr. Build. Mater. 25, 2713–2722.

https://doi.org/10.1016/j.conbuildmat.2010.12.022

Cachim, P.B., 1999. Experimental and numerical analysis of the behaviour of structural concrete under fatigue loading with applications to concrete pavements, Ph.D. thesis. University of Porto.

Chang, D.-I., Chai, W.-K., 1995. Flexural fracture and fatigue behavior of steel-fiber-reinforced concrete structures. Nucl. Eng. Des. 156, 201–207.

Ciancio, D., Mazzotti, C., Buratti, N., 2014. Evaluation of fibre-reinforced concrete fracture energy through tests on notched round determinate panels with different diameters. Constr. Build. Mater. 52, 86–95. https://doi.org/10.1016/j.conbuildmat.2013.10.079

CNR DT 204, 2006. Guidelines for the design, construction and production control of fibre reinforced concrete structures. National Research Council of Italy.

Cotterell, B., Mai, Y.-W., 1987. Crack growth resistance curve and size effect in the fracture of cement paste. J. Mater. Sci. 22, 2734–2738.

Dey, V., Kachala, R., Bonakdar, A., Mobasher, B., 2015. Mechanical properties of micro and sub-micron wollastonite fibers in cementitious composites. Constr. Build. Mater. 82, 351–359. https://doi.org/10.1016/j.conbuildmat.2015.02.084

di Prisco, M., 2004. On the identification of SFRC constitutive law in uniaxial tension. 6th Int. RILEM Symp. Fibre Reinf. Concr. 827–836.

Eissa, A., Batson, G., 1996. Model for Predicting the Fracture Process Zone and R-curve for High Strength FRC. Cem. Concr. Compos. 18, 125–133.

EN 14651, 2005. Test method for metallic fibre concrete-Measuring the flexural tensile strength (limit of proportionality (LOF), residual). European Standards. Brussels, Belgium.

Ferreira, L.E.T., Bittencourt, T.N., Sousa, J., Gettu, R., 2002. R-curve behavior in notched beam tests of rocks. Eng. Fract. Mech. 69, 1845–1852.

Fett, T., Munz, D., Geraghty, R.D., White, K.W., 2000. Bridging stress determination by evaluation of the R-curve. J. Eur. Ceram. Soc. 20, 2143–2148.

fib Model, 2010. Code for Concrete Structures. fib CEB-FIP publication.

Foote, R.M.L., Mai, Y.-W., Cotterell, B., 1986. Crack growth resistance curves in strain-softening materials. J. Mech. Phys. Solids 34, 593–607.

García-Álvarez, V.Ó., Gettu, R., Carol, I., 2017. Determination of the energy release rate function for an eccentrically notched center-loaded beam using elastic fracture analysis. J. Struct. Eng. 44, 88–94.

Germano, F., Tiberti, G., Plizzari, G., 2016. Post-peak fatigue performance of steel fiber reinforced concrete under flexure. Mater. Struct. 49, 4229–4245. https://doi.org/10.1617/s11527-015-0783-3

Gettu, R., Barragán, B., García, T., Fernández, C., Oliver, R., 2004. Steel fiber reinforced concrete for the Barcelona metro line 9 tunnel lining. 6th Int. RILEM Symp. Fibre Reinf. Concr. 141–156.

Gettu, R., Bažant, Z.P., Karr, M.E., 1990. Fracture properties and brittleness of high-strength concrete. ACI Mater. J. 87, 608–618.

Gettu, R., Mobasher, B., Carmona, S., Jansen, D.C., 1996. Testing of concrete under closed-loop control. Adv. Cem. Based Mater. 3, 54–71.

Gopalaratnam, V.S., Cherian, T., 2002. Fatigue Characteristics of Fiber Reinforced Concrete for Pavement Applications. ACI Spec. Publ. 206.

Granju, J.., Rossi, P., Chanvillard, G., Mesureur, B., Turatsinze, A., Farhat, H., Boulay, C., Serrano, J.-J., Fakhri, P., Roque, O., Rivillion, P., 2000. Delayed Behaviour of Cracked SFRC Beams, in: Fifth RILEM Symposium on Fibre-Reinforced Concrete. pp. 511–520.

Grzybowski, M., Meyer, C., 1993. Damage accumulation in concrete with and without fiber reinforcement. ACI Mater. J.

Hillerborg, A., Modeer, M., Petersson, P.-E., 1976. Analysis of crack formation and crack growth in concrete by means of fracture mechanics and finite elements. Cem. Concr. Res. 6, 773–782.

ICI-TC/01.1, 2014. Test methods for the flexural strength and toughness parameters of fiber reinforced concrete, Indian concrete institute technical committee recommendation. Indian Concr. Inst. J. 15, 39–43.

IRC:58, 2010. Plain jointed rigid pavements design for highways.

IRC:SP:46, 2013. Guidelines for Design and Construction of Fibre Reinforced.

ITA, 2000. WG Research Guidelines for the design of shield tunnel lining. Tunn. Undergr. Sp. Technol. 15, 303–331. https://doi.org/10.1016/S0886-7798(00)00058-4

Jenq, Y., Shah, S.P., 1986. Two parameter fracture model for concrete. J. Eng. Mech. 111, 1227–1241.

Jepsen, M.S., Damkilde, L., Lövgren, I., 2016. A fully general and adaptive inverse analysis method for cementitious materials. Mater. Struct. 1–14. https://doi.org/10.1617/s11527-015-0791-3

Johnston, C.D., Zemp, R.W., 1992. Flexural fatigue performance of steel fiber reinforced concrete-influence of fiber content , aspect ratio , and type 88, 374–383.

Jose, S., Gettu, R., Indhuja, S., 2018. Flexural toughness characterization of steel, polymer and glass fibre reinforced concrete based on the notched beam test. Indian Concr. J. 92, 35–50.

JSCE Part III-2 (SF1–SF4), 1984. Method of Tests for Steel Fiber Reinforced Concrete.

Kang, S.-T., Lee, Y., Park, Y.-D., Kim, J.-K., 2010. Tensile fracture properties of an Ultra High Performance Fiber Reinforced Concrete (UHPFRC) with steel fiber. Compos. Struct. 92, 61–71. https://doi.org/10.1016/j.compstruct.2009.06.012

Karihaloo, B.L., 1995. Fracture Mechanics & Structural Concrete(Concrete Design & Construction Series).

Karihaloo, B.L., Nallathambi, P., 1989. An improved effective crack model for the determination of fracture toughness of concrete. Cem. Concr. Res. 19, 603–610. https://doi.org/10.1016/0008-8846(89)90012-4

Kitsutaka, Y., 1997. Fracture parameters by polylinear tension-softening analysis. J. Eng. Mech. 123, 444–450. https://doi.org/10.1017/CBO9781107415324.004

Kooiman, A.G., 2000. Modelling steel fibre reinforced concrete for structural design, Ph.D. Thesis. Delft Univ. of Technology, The Netherlands.

Kumar, S., Barai, S. V., 2010. Determining the double-K fracture parameters for three-point bending notched concrete beams using weight function. Fatigue Fract. Eng. Mater. Struct. 33, 645–660. https://doi.org/10.1111/j.1460-2695.2010.01477.x

Lee, M.K., Barr, B.I.G., 2004. An overview of the fatigue behaviour of plain and fibre reinforced concrete. Cem. Concr. Compos. 26, 299–305. https://doi.org/10.1016/S0958-9465(02)00139-7

Li, V.C., Matsumoto, T., 1998. Fatigue crack growth analysis of fibre reinforced concrete with effect of interfacial bond degradation. Cem. Concr. Compos. 20, 339–351.

https://doi.org/10.1103/PhysRevLett.116.247201

Lloyd, J.P., Loft, J.L., Kesler, C.E., 2007. Fatigue of concrete. University of Illinois at Urbana Champaign, College of Engineering. Engineering Experiment Station.

Löfgren, I., 2005. Fibre-reinforced concrete for industrial construction, Ph.D. Thesis. Chalmars University of Technology, Sweden.

Löfgren, I., Stang, H., Olesen, J.F., 2005. Fracture properties of FRC determined through inverse analysis of wedge splitting and three-point bending tests. J. Adv. Concr. Technol. 3, 423–434. https://doi.org/10.3151/jact.3.423

Mai, Y.W., 2001. Cohesive zone and crack-resistance (R)-curve of cementitious materials and their fibre-reinforced composites. Eng. Fract. Mech. 69, 219–234. https://doi.org/10.1016/S0013-7944(01)00086-8

Mechtcherine, V., 2009. Fracture mechanical behavior of concrete and the condition of its fracture surface. Cem. Concr. Res. 39, 620–628. https://doi.org/10.1016/j.cemconres.2009.03.011

Meda, A., Plizzari, G.A., Slowik, V., 2001. Fracture of fiber reinforced concrete slabs on grade. Fract. Mech. Concr. Struct. 1013–1020.

Meng, W., Yao, Y., Mobasher, B., Khayat, K.H., 2017. Effects of loading rate and notch-to-depth ratio of notched beams on flexural performance of ultra-high-performance concrete. Cem. Concr. Compos. 83, 349–359. https://doi.org/10.1016/j.cemconcomp.2017.07.026

Mobasher, B., Bonakdar, A., Bakhshi, M., 2015. Back-calculation procedure for cyclic flexural fracture tests in fiber reinforced concrete. Am. Concr. Institute, ACI Spec. Publ. 71–92.

Mobasher, B., Li, C.Y., 1996. Mechanical Properties of Hybrid Cement-Based Composites. ACI Mater. J. 93, 284–292.

Morel, S., Lespine, C., Coureau, J., Planas, J., Dourado, N., 2010. Bilinear softening parameters and equivalent LEFM R-curve in quasibrittle failure. Int. J. Solids Struct. 47, 837–850. https://doi.org/10.1016/j.ijsolstr.2009.11.022

Murdock, J.W., 1965. A Critical Review of Research on Fatique of Plain Concrete. Eng. Exp. Stn. Bull. 475.

Naaman, A.E., Gopalaratnam, V.S., 1983. Impact properties of steel fibre reinforced concrete in bending. Int. J. Cem. Compos. Light. Concr. 5, 225–233. https://doi.org/10.1016/0262-5075(83)90064-7

Nanakorn, P., Horii, H., 1996a. Back analysis of tension-softening relationship of concrete. JSCE 32, 265–275.

Nanakorn, P., Horii, H., 1996b. A fracture-mechanics-based design method for SFRC tunnel linings. Tunn. Undergr. Sp. Technol. 11, 39–43. https://doi.org/10.2208/jscej.1996.532_221

Nayar, S.K., 2015. Design of fibre reinforced concrete slabs-on-grade and pavements: PhD thesis. Indian Institute of Technology Madras.

Nayar, S.K., Gettu, R., Krishnan, C.S., 2014. Characterisation of the toughness of fibre reinforced concrete--Revisited in the Indian context. Indian Concr J 88, 8–23.

Nieuwoudt, P.D., Boshoff, W.P., 2017. Time-dependent pull-out behaviour of hooked-end steel fibres in concrete. Cem. Concr. Compos. 79, 133–147. https://doi.org/10.1016/j.cemconcomp.2017.02.006

Nour, A., Massicotte, B., de Montaignac, R., Charron, J.-P., 2015. Development of an inverse analysis procedure for the characterisation of softening diagrams for FRC beams and panels. Constr. Build. Mater. 94, 35–44. https://doi.org/10.1016/j.conbuildmat.2015.06.049

Olesen, J.F., 2001. Fictitious crack propagation in fibre reinforced concrete beams. J. Eng. Mech. 127, 272–280.

Østergaard, L., 2003. Early-age fracture mechanics and cracking of concrete, Ph.D. Thesis. Technical University of Denmark.

Østergaard, L., Olesen, J.F., 2003. Comparative study of fracture mechanical test methods for concrete. Fract. Mech. Concr. Struct. 455–462.

Ouyang, C., Barzin, M., Surendra P., S., 1990. An R-curve approach for fracture of quasi-brittle materials. Eng. Fract. Mech. 37, 901–913. https://doi.org/10.1016/0013-7944(90)90087-W

Planas, J., Guinea, G. V, Elices, M., 1999. Size effect and inverse analysis in concrete fracture. Int. J. Fract. 95, 367–378.

Plizzari, G.A., Cominoli, L., 2005. Numerical simulations of SFRC precast tunnel segments, in: Erdem, Y., Solak, T. (Eds.), In Proceedings of ITA-AITES 2005, Underground Space Use: Analysis of the Past and Lessons for the Future. Istanbul (Turkey), pp. 1105–1112.

Ramakrishnan, V., Wu, G.Y., Hosalli, G., 1989. Flexural Fatigue Strength, Endurance Limit, and Impact Strength of Fiber Reinforced Concretes. Transp. Res. Rec. J. Transp. Res. Board 1226, 17–24.

Raphael, B., Smith, I.F.C., 2003. A direct stochastic algorithm for global search. Appl. Math. Comput. 146, 729–758. https://doi.org/http://dx.doi.org/10.1016/S0096-3003(02)00629-X

Reddy, C.K., Subramaniam, K.V.L., 2017. Analysis for multi-linear stress-crack opening cohesive relationship: Application to macro-synthetic fiber reinforced concrete. Eng. Fract. Mech. 169, 128–145. https://doi.org/10.1016/j.engfracmech.2016.11.015

Report, I.T.A., 2016. Twenty years of FRC tunnel segments practice : Lessons learnt and proposed design principles ITA Working Group 2.

RILEM TC 162-TDF, 2003. Final recommendation of RILEM TC 162-TDF: Test and design methods for steel fibre reinforced concrete sigma-epsilon-design method. Mater. Struct. 36, 560–567. https://doi.org/10.1617/14007

RILEM TC 162-TDF, 2002. Recommendations of RILEM TC 162-TDF: Test and design methods for steel fibre reinforced concrete: bending test. Mater. Struct. 35, 579–582. https://doi.org/10.1617/14007

Roelfstra, P.E., Wittmann, F.H., 1986. Numerical method to link strain softening with failure of concrete. Fract. toughness Fract. energy Concr. 163–175.

Rosa, A.L., Yu, R.C., Ruiz, G., Saucedo, L., Sousa, J.L.A.O., 2012. A loading rate dependent cohesive model for concrete fracture. Eng. Fract. Mech. 82, 195–208. https://doi.org/10.1016/j.engfracmech.2011.12.013

Rots, J.G., Blaauwendraad, J., 1989. Crack models for concrete: discrete or smeared? fixed, multi-directional or rotating? Heron 34, 1–56.

Santos, F.L.G. dos, Sousa, J.L.A.O., 2015. Determination of parameters of a viscous-cohesive fracture model by inverse analysis. IBRACON Struct. Mater. J. 8, 669–706. https://doi.org/10.1590/S1983-41952015000500007

Shukla, S.P., Yadav, S.K., Lohani, B., Behera, S.N., 2012. Characterization of traffic noise for a typical Indian road crossing Characterization of traffic noise for a typical

Indian road crossing. Curr. Sci. 103, 1193–1201.

Skoček, J., Stang, H., 2010. Application of optical deformation analysis system on wedge splitting test and its inverse analysis. Mater. Struct. 43, 63–72. https://doi.org/10.1617/s11527-010-9597-5

Skoček, J., Stang, H., 2008. Inverse analysis of the wedge-splitting test. Eng. Fract. Mech. 75, 3173–3188. https://doi.org/10.1016/j.engfracmech.2007.12.003

Slowik, V., Villmann, B., Bretschneider, N., Villmann, T., 2006. Computational aspects of inverse analyses for determining softening curves of concrete. Comput. Methods Appl. Mech. Eng. 195, 7223–7236. https://doi.org/10.1016/j.cma.2005.04.021

Soetens, T., Matthys, S., 2014. Different methods to model the post-cracking behaviour of hooked-end steel fibre reinforced concrete. Constr. Build. Mater. 73, 458–471. https://doi.org/10.1016/j.conbuildmat.2014.09.093

Sorelli, L.G., Toutlemonde, F., 2005. On the Design of Steel Fibre Reinforced Concrete Tunnel Lining Segments. 11th Int. Conf. Fract. 3–8.

Soufeiani, L., Raman, S.N., Jumaat, M.Z. Bin, Alengaram, U.J., Ghadyani, G., Mendis, P., 2016. Influences of the volume fraction and shape of steel fibers on fiber-reinforced concrete subjected to dynamic loading – A review. Eng. Struct. 124, 405–417. https://doi.org/10.1016/j.engstruct.2016.06.029

Sousa, J.L.A.O., Gettu, R., 2006. Determining the tensile stress-crack opening curve of concrete by inverse analysis. J. Eng. Mech. 132, 141–148. https://doi.org/10.1061/(ASCE)0733-9399(2006)132:2(141)

Sousa, J.L.A.O., Gettu, R., Kitsutaka, Y., 2007. Inverse analysis procedures for determining the tensile stress-crack opening curve of concrete. Exp. Determ. Stress. Open. curve Concr. Tens. RILEM TC 187-SOC Final Rep. 31–39.

Spadea, G., Bencardino, F., 1997. Behavior of fiber-reinforced concrete beams under cyclic loading. J. Struct. Eng. 123, 660–668.

Stang, H., Olesen, J.F., 1998. On the interpretation of bending tests in FRC materials, in: FRAMCOS-3. pp. 511–520.

Stephen, S.J., Gettu, R., Ferreira, L.E.T., Jose, S., 2018. Assessment of the toughness of fibre-reinforced concrete using the R-curve approach. Sādhanā 43–46. https://doi.org/10.1007/s12046-018-0838-6

Stephen, S.J., Raphael, B., Gettu, R., Jose, S., 2019. Determination of the tensile constitutive relations of fibre reinforced concrete using inverse analysis. Constr. Build. Mater. 195, 405–414.

Tada, H., Paris, P., Irwin, G., 1973. The stress analysis of cracks, Del Research Corp, Hellertown PA. Handbook, Del Research Corp, Hellertown PA.

TR34, 2013. Concrete Industrial Ground floors: A Guide to Design and Construction. The Concrete Society, England.

Ulfkjær, J.P., Krenk, S., Brincker, R., 1995. Analytical model for fictious crack propagation in concrete beams. J. Eng. Mech. 121, 7–15.

Wallin, K., 2013. A simple fracture mechanical interpretation of size effects in concrete fracture toughness tests. Eng. Fract. Mech. 99, 18–29. https://doi.org/10.1016/j.engfracmech.2013.01.018

Wecharatana, M., Shah, S.P., 1983. Predictions of Nonlinear Fracture Process Zone in Concrete. J. Eng. Mech. 109, 1231–1246. https://doi.org/10.1061/(ASCE)0733-9399(1983)109:5(1231)

Wei, S., Jianming, G., Yun, Y., 1996. Study of the Fatigue Performance and Damage Mechanism of Steel Fiber Reinforced Concrete. Mater. J. 93, 206–212. https://doi.org/10.14359/9804

Wu, Z., Yang, S., Hu, X., Zheng, J., 2006. An analytical model to predict the effective fracture toughness of concrete for three-point bending notched beams. Eng. Fract. Mech. 73, 2166–2191. https://doi.org/10.1016/j.engfracmech.2006.04.001

Xu, S., Reinhardt, H.W., 1998. Crack extension resistance and fracture properties of quasi-brittle softening materials like concrete based on the complete process of fracture. Int. J. Fract. 92, 71–99. https://doi.org/10.1023/A:1007553012684

Yao, Y., Bakhshi, M., Nasri, V., Mobasher, B., 2018. Interaction diagrams for design of hybrid fiber-reinforced tunnel segments. Mater. Struct. Constr. 51, 1–17. https://doi.org/10.1617/s11527-018-1159-2

Yoo, D.Y., Kang, S.T., Yoon, Y.S., 2014. Effect of fiber length and placement method on flexural behavior, tension-softening curve, and fiber distribution characteristics of UHPFRC. Constr. Build. Mater. 64, 67–81. https://doi.org/10.1016/j.conbuildmat.2014.04.007

Zhang, J., Stang, H., Li, V.C., 1999. Fatigue life prediction of fibre reinforced concrete under flexural load. Int. J. Fatigue 21, 1033–1049. https://doi.org/10.1016/S0142-1123(99)00093-6

Zhang, X.X., Abd Elazim, A.M., Ruiz, G., Yu, R.C., 2014. Fracture behaviour of steel fibre-reinforced concrete at a wide range of loading rates. Int. J. Impact Eng. 71, 89–96. https://doi.org/10.1016/j.ijimpeng.2014.04.009

Zhao, Y., Chang, J., Gao, H., 2015. A three-parameter R-curve of concrete-like quasi-brittle materials. Constr. Build. Mater. 78, 243–249. https://doi.org/10.1016/j.conbuildmat.2015.01.029

PUBLICATIONS BASED ON THE THESIS

Journal Publications:

A. Paper publications in Journal.

1. **Stephen S. J.,** Gettu R., Ferreira L. E. T., and Jose S., “Assessment of the toughness of fibre reinforced concrete using the R-curve approach”, Sādhanā, 43–46 (2018).
2. **Stephen S. J.**, Raphael B., Gettu R., and Jose S., “Determination of the tensile constitutive relations of fibre reinforced concrete using inverse analysis”, Construction and Building Materials, 195, 405-414 (2019).

B. International conference proceedings (* indicates presenter)

1. **Stephen S. J.**, Gettu R.*, and Raphael B., "Effect of loading rate on the fracture behaviour of fibre reinforced concrete", Proc. 9th International Conference on Fracture Mechanics of Concrete and Concrete Structures, FraMCoS-9 (Berkeley, USA), Eds. V. Saouma, J. Bolander and E. Landis, http://framcos.org/FraMCoS-9/Full-Papers/71.pdf, DOI 10.21012/FC9.071, 6 p. (2016)
2. **Stephen S. J.***, Raphael B., and Gettu R., "Obtaining fracture properties of FRC by inverse analysis using the PGSL optimization algorithm", Proc. 6th International Congress on Computational Mechanics and Simulation, ICCMS2016 (Mumbai, India), Eds. S. Pendhari, P. Nanthagopalan, V. Deshmukh, A. Bambole and Y. Desai, http://www.iccms2016.org/Docs/ICCMS_Proceeding.pdf, 480 p. (2016)
3. Jose S.*, **Stephen S. J.,** and Gettu R., “Study of the post-cracking behaviour of steel and polymer fibre reinforced concretes”, Proc. 2nd R. N. Raikar Memorial International Conference on Advances in Science and Technology of Concrete (Mumbai, India), 258p. (2015)

C. Conference presentations

1. **Stephen S. J.***, Jose S., and Gettu R., “Benefits of hybrid combinations of amorphous metallic and steel fibres in structural applications” the ACI Open Topic Session at the ACI Convention and Exposition in Las Vegas, NV, USA, 14 – 18th October, 2018 (Oral Presentation)